Measurement of the W Boson Mass in the $\mathrm{e^+e^-} \to \mathrm{W^+W^-} \to \ell\nu_\ell\ell'\nu_{\ell'}$ Channel with the OPAL Detector at LEP

Dissertation der Fakultät für Physik

der

Ludwig-Maximilians-Universität München

vorgelegt von

Patricia Méndez Lorenzo

aus

Salamanca (Spanien)

München, den 25. Mai 2001

1. Gutachter: Prof. Dr. Dorothee Schaile

2. Gutachter: Prof. Dr. Martin Faessler

Tag der mündlichen Prüfung: 6. August 2001

Measurement of the W Boson Mass in the $e^+e^- \rightarrow W^+W^- \rightarrow \ell\nu_\ell\ell'\nu_{\ell'}$ Channel with the OPAL Detector at LEP

Dissertation der Fakultät für Physik

der

Ludwig-Maximilians-Universität München

vorgelegt von

Patricia Méndez Lorenzo

aus

Salamanca (Spanien)

Mai 2001

A mis padres

Summary

Using data collected at center-of-mass energies from 183 to 202 GeV with the OPAL detector at LEP, which amount to an integrated luminosity of 457.1 pb^{-1}, the mass of the W boson is measured in the fully leptonic decay channel, $\mathrm{W}^+\mathrm{W}^- \to \ell\nu_\ell\ell'\nu_{\ell'}$. An approximative reconstruction of the events and the directly measured energies of the leptons are used to determine the W mass in this channel with two different procedures; a binned fit using a reweighting method and an unbinned fit based on a parametrization of the distributions of the sensitive variables. The results obtained from the two methods are:

$$\mathrm{M_W} = 80.30 \begin{array}{c} +0.48 \\ -1.55 \end{array} \pm 0.14\ \mathrm{GeV},$$

for the reweighting method and

$$\mathrm{M_W} = 80.43 \begin{array}{c} +0.51 \\ -0.52 \end{array} \pm 0.16\ \mathrm{GeV},$$

for the unbinned fit. The first error is statistical and the second systematic. Both measurements are consistent with each other and with the world average of $\mathrm{M_W}$.

Zusammenfassung

Die Masse des W Bosons wird im rein leptonischen Kanal, $\mathrm{W^+W^-} \rightarrow \ell\nu_\ell\ell'\nu_{\ell'}$, bestimmt. Hierzu werden Daten des OPAL Detektors am LEP Beschleuniger, die bei Schwerpunktsenergien von 183 bis 202 GeV aufgezeichnet wurden und einer integrierten Luminosität von 457.1 pb^{-1} entsprechen, verwendet. Zwei auf die Masse des W Bosons sensitive Variablen werden untersucht: die Pseudomasse, die aus einer approximativen Rekonstruktion der Ereignisse gewonnen wird, und die leptonische Energie. Zur Bestimmung der W Masse werden zwei Verfahren angewendet. Ein direkter Vergleich der Variablenspektra mit Monte Carlo Simulationen, die durch eine Umgewichtungsmethode gewonnen werden, sowie ein Ungebinnter Likelihood Fit die auf einer analytischen Parametrisierung der sensitiven Variablen basiert. Für die Umgewichtungsmethode ergibt sich die W Masse zu

$$\mathrm{M_W} = 80.30 \begin{array}{c}+0.48\\-1.55\end{array} \pm 0.14\ \mathrm{GeV},$$

und aus dem analytischen Fit erhält man

$$\mathrm{M_W} = 80.43 \begin{array}{c}+0.51\\-0.52\end{array} \pm 0.16\ \mathrm{GeV}.$$

Der erste Fehler entspricht der statistischen und der zweite der systematischen Unsicherheit der Messung. Die mit den zwei Methoden bestimmten Massen sind in guter Übereinstimmung miteinander und mit dem Weltmittelwert der W Masse.

Contents

Chapter 1

Introduction and Overview

The current theory describing the matter and its interactions, the Standard Model, consists of the quantum field theories of the strong and the electroweak interactions and it is based on the $\mathrm{SU(3)_C} \times \mathrm{U(1)_Y} \times \mathrm{SU(2)_I}$ gauge group. In this theory, all matter is made of two types of fundamental spin $\frac{1}{2}$-particles; *leptons* with integer charge and *quarks* with fractional charge. The interactions between these fundamental particles are described by spin 1-particles called *bosons*, which are the mediators of the forces: the electromagnetic, the weak and the strong forces.

In 1967 Weinberg [1], Salam [2] and Glashow [3] proposed a model, which treated the electromagnetic and weak forces as different aspects of a single electroweak interaction. In a formulation similar to the QED model, they defined a unified gauge theory based on a SU(2) group of weak isospin and a U(1) group of weak hyper-charge. The interactions between the particles would take place by the exchange of four bosons; a massless photon and three massive particles, Z, W^+, and W^-. At the beginning of the seventies, the theory was proven to be renormalizable by 't Hooft [4] and Veltman [5].

The actual theory of the strong interactions had its origin in the sixties when new evidence for quarks started to come from different experiments. Among all the proposed theories of the strong interaction the quantum chromodynamics, the QCD, claimed to be the only fundamental theory of this force [6]. The QCD is a theory based on the $\mathrm{SU(3)_C}$ color gauge group and it explains the strong interaction by the exchange of eight massless particles called *gluons*.

The progress in particle accelerators and the development of new detection techniques have been decisive for the study and experimental verification of the Standard Model. An important milestone was achieved in 1983 by the experiment UA1 in the proton-proton ring SPS at CERN, when the first experimental evidences of the Z, W^+ and W^- bosons were observed [7]. In order to continue with the study of these bosons and to perform consistency tests of the Standard Model, the electron-positron ring LEP at CERN was constructed and began to take data in 1989.

In the first phase of the accelerator, called LEP1 programme [8], collisions between electrons and positrons were performed at a center-of-mass energy around the resonance peak of the Z boson at 91 GeV. The approximately 4 millions Z decays per experiment recorded in this phase provided very precise measurements of the properties of this boson and showed good agreement with the Standard Model predictions.

From 1996 onwards, the center-of-mass energy was increased above the W pairs production threshold of 161 GeV. The energy was further increased in steps up to 208 GeV at the end of

2000. In this phase of the accelerator, called LEP2 programme [9], the study of the properties of the W boson is one of the major goals of the experiment, in particular the mass of the W boson. This measurement provides stringent tests of the Standard Model and when combined with the mass of the Z boson and other electroweak precision measurements, the W mass can be used to constrain the range of the mass of the not yet observed Higgs boson [10]. This particle, predicted by the theory, gives rise of the masses of the different particles by the interaction of these with the Higgs boson.

This thesis presents a measurement of the mass of the W boson in the fully leptonic decay channel using the data of the OPAL detector at LEP and it is structured as follows: After this introduction, chapter 2 describes the e^+e^- collider LEP, the OPAL detector and the data acquisition system together with the Monte Carlo simulation. Chapter 3 provides a brief explanation of the Standard Model, chapter 4 concentrates on the W^+W^- production at LEP2. The selection of the leptonic events and the general description of the Monte Carlo generators used in the analysis are explained in chapter 5. Chapter 6 presents the two sensitive variables to be used in the analysis. A first method to measure M_W using a reweighting method is explained in chapter 7, whereas in chapter 8 the measurement is based on an unbinned method. In chapter 9 the results from both methods are compared and combined with other M_W measurements from OPAL and from LEP. Finally the conclusions of the thesis are presented in chapter 10.

Chapter 2

LEP and OPAL

2.1 The e^+e^- Collider LEP at CERN

The Large Electron Positron collider LEP at the European Laboratory for Particle Physics CERN near Geneva is the largest particle accelerator in the world. Around its 27 km of circumference, bunches of electrons and positrons collide 100 m below the surface in four interaction points, where four detectors are placed. LEP has the shape of an octagon and consists of eight arcs joined by eight straight sectors [11]. Figure 2.1 shows an aerial view of LEP. The interaction regions, P2, P4, P6 and P8 correspond to the four large underground LEP experiments, L3 [12] at P2, ALEPH [13] at P4, OPAL [14] at P6 and DELPHI [15] at P8.

At these four symmetric points around the ring the bunches of particles are focused and are collided in the center of the experiments. Each bunch contains more than 10^{11} particles, but only one in about 40000 collisions between the bunches produces the desired effect of frontal collision between an electron and a positron. For this reason the bunches circulate for hours, each one traveling more than 10000 times a second around the ring. To focus the bunches, quadrupole and sextupole magnets are placed in the arcs together with dipoles to bend the bunches. The straight sectors have radio-frequency cavities to accelerate the particles and compensate the energy loss of the electrons and positrons in the arcs of the circumference due to the synchrotron radiation. This energy loss W can be written as

$$\mathrm{W} = \mathrm{A} \times \frac{(\mathrm{E}[\mathrm{GeV}])^4}{\rho[\mathrm{Km}]} \ \mathrm{GeV\ per\ turn} \tag{2.1}$$

for electrons at sufficiently high energy ($\mathrm{v} \approx \mathrm{c}$). A is a numerical constant whose value is 8.85×10^{-8} for the LEP accelerator, E is the energy of the electrons and positrons and ρ is the radius of curvature. For a beam energy of 100 GeV the energy loss of electrons and positrons in the LEP ring is about 2 GeV per turn.

Figure 2.2 shows the LEP injection system. A high-intensity electron gun supplies electrons to the first LEP injection linac [1] (LIL) [11]. The electrons emerging from this first LIL have an energy of 200 MeV and they strike a tungsten converter target to produce positrons. An electron gun located near the converter provides the electrons to be used in LEP. After the converter, a

[1] Linear accelerator.

Figure 2.1: Aerial view of the e^+e^- collider LEP at the European Laboratory for particles physics CERN near Geneva.

second LIL is located to accelerate both electrons and positrons to 600 MeV in 12 ns pulses. The electron-positron accumulator ring (EPA) after the two LILs is a racetrack shaped storage ring with a perimeter of 126 m, which accumulates particles in eight bunches at 600 MeV before they are injected into the Proton Synchrotron (PS). Here, in a ring with a circumference of 630 m, the leptons are accelerated to 3.5 GeV, with which they are introduced into the Super Proton Synchrotron (SPS). The SPS ring has a circumference of 6.9 km and it consists of 32 copper single-cavities and two super-conducting cavities, which increase the lepton beam energy to 22 GeV. Finally the beams are introduced into the LEP collider whose acceleration system increases the beam energy from 22 GeV to the operating energy and replaces the energy loss due to the synchrotron radiation.

LEP started to operate in summer 1989. Since that year and until 1995 the accelerator worked at a center-of-mass energies around the Z resonance peak at 91 GeV. For such an energy, 128 copper cavities were enough to compensate the energy loss [16]. Since 1996 and until November 2000, LEP operated at center-of-mass energies around and above the $\mathrm{W^+W^-}$ threshold production; from $\sqrt{\mathrm{s}}$ = 161 GeV up to $\sqrt{\mathrm{s}}$ = 208 GeV. Additional super-conducting cavities were added to the system to compensate losses due to the much higher-synchrotron radiation.

Another important parameter of all accelerators is the luminosity [17], $\mathcal{L}$, which determines the rate of events N per time as a function of the interaction cross-section σ_{int}:

$$\frac{dN}{dt} = \mathcal{L}\,\sigma_{int} \tag{2.2}$$

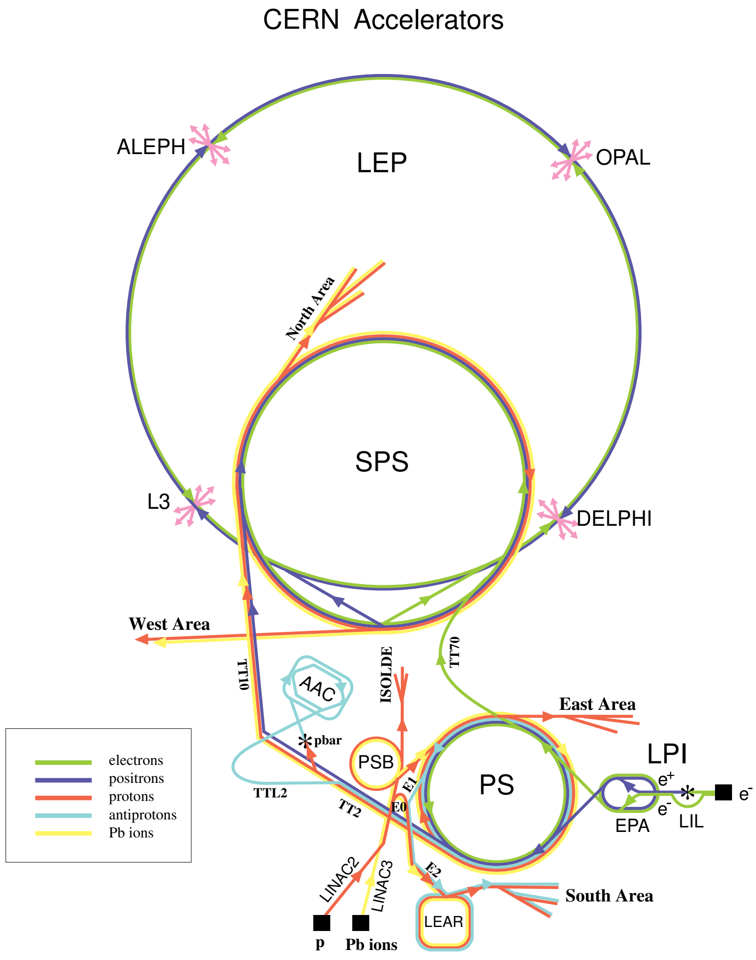

LEP: Large Electron Positron collider
SPS: Super Proton Synchrotron
AAC: Antiproton Accumulator Complex
ISOLDE: Isotope Separator OnLine DEvice
PSB: Proton Synchrotron Booster
PS: Proton Synchrotron
LPI: Lep Pre-Injector
EPA: Electron Positron Accumulator
LIL: Lep Injector Linac
LINAC: LINear ACcelerator
LEAR: Low Energy Antiproton Ring

Figure 2.2: LEP injection system.

If there are two bunches containing n_1 and n_2 particles colliding with a frequency f, then the luminosity is given by:

$$\mathcal{L} = f\frac{n_1 n_2}{4\pi\sigma_x\sigma_y} \tag{2.3}$$

where σ_{x} and σ_{y} characterize the horizontal and vertical dimensions at the interactions points.

During LEP1, the four experiments recorded more than 16 millions of Z decays. These data have provided an extremely accurate knowledge of the Z boson parameters; its mass and its partial and total decay widths [16]. In the second phase of LEP, a total luminosity of 600 pb^{-1} was recorded by each of the four experiments [18]. In this era, the study of the properties of the W boson together with the search of new particles were the major goals [9].

The 2nd of November 2000 was the indicated date for the end of LEP. After that day, the four experiments were dismantled to make space for a new research experiment, the Large Hadron Collider (LHC). The new accelerator will be placed in the old LEP tunnel and it will have two main experiments: ATLAS [19] and CMS [20]. The beginning of data taking at the LHC is expected in 2005–2006.

2.2 The OPAL Detector at LEP

The OPAL (Omni Purpose Apparatus at LEP) detector is designed to provide precise measurements of charged particles and of electromagnetic energy over the full solid angle. The basic idea behind its design has been the detection of all types of interactions occurring in $\mathrm{e}^+\mathrm{e}^-$ collisions with efficient and accurate reconstruction and the unambiguous classification of the events. A general description of OPAL detector can be found in [14, 21, 22].

In its cylindrical form of 12 m length and 10 m diameter, the different sub-detectors are placed around the beam pipe. The main elements of this detector are a central tracking system, a solenoidal magnet coil, an electromagnetic calorimeter, a hadron calorimeter and finally a muon detector. In addition, a pair of forward detectors is used to measure the luminosity and to identify particles emitted at small angles with respect to the beam pipe. Two views of the OPAL detector are shown in figures 2.3 and 2.4. Figure 2.3 shows a three dimensional schematic view of the OPAL detector and figure 2.4 two cross section views of the OPAL detector, one in the r-θ plane and the other one along the beam-line.

To describe the data recorded with the OPAL detector, a cartesian coordinate system is used. The z axis is defined by the electron beam direction and the x-y axises define the transversal plane, where x points towards the center of the LEP collider and y is the perpendicular direction. The measured tracks can also be defined in a polar coordinate system; the polar angle θ and the azimut ϕ.

The OPAL collaboration is a team of physicists and engineers who designed, built and run the OPAL detector, and who analyze the collected data. The collaboration consists of over 300 people from thirty-four institutes around the world.

The most important elements of the detector are described briefly in the next subsections.

2.2.1 The Central Tracking System

The system of central tracking chambers is contained in a solenoid which provides a magnetic field of 0.435 T along the z-axis. It is designed to measure charged particles which travel across the detector.

The first element of the tracking system found after the beam pipe is the **Silicon microvertex detector**. This element (introduced in OPAL in 1992) is designed to provide a precise measurement of the vertex position and consists of silicon microstrips counters [23].

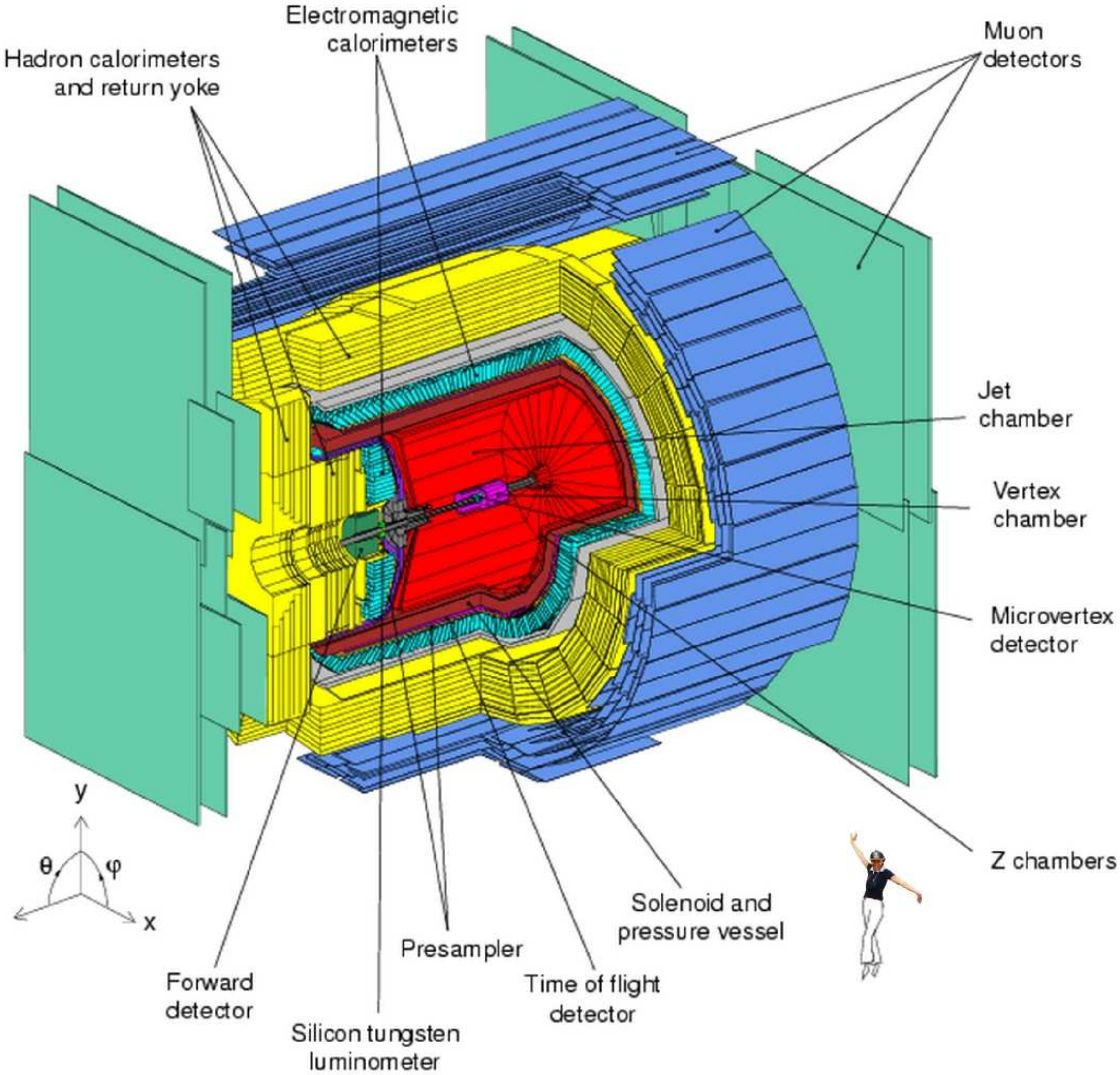

Figure 2.3: OPAL detector at LEP.

The **vertex detector** is a 1 meter long, 470 mm diameter, cylindrical drift chamber located between the Silicon microvertex and the Jet chamber. It is used to locate decay vertices of short lived particles and to improve the momentum resolution. The chamber consists of an inner layer of 36 cells with axial wires and an outer layer of 36 small angle stereo cells. The axial cells provide a precise measurement of the tracks position in the $r - \phi$ plane, while the stereo cells give an accurate z measurement for charged particles close to the interaction region.

The **Jet chamber** is designed to measured the momentum of the charged particles combining good space and double track resolution, fundamental for the efficient recording of jet events. The Jet chamber operation is based on the ionization of atoms by charged particles, which pass through the gas that fills the detector. The electrons liberated in this process drift in an electric field towards anode wires. The amount of ionization that a charged particle causes per unit length as it flies through the Jet chamber depends on the charge and momentum of the particle. The specific energy loss dE/dx is an important tool for particles identification.

The sensitive volume of the jet chamber is a cylinder with a length of about 4 m, surrounding the beam pipe and vertex detector. The chamber is subdivided in 24 identical sectors, each containing a plane with 159 sense wires, parallel to the beam direction.

The last element of the central tracking system are the **z-chambers**. They are used to obtain a precise measurement of the z coordinate of the tracks as they leave the Jet chamber and thus to improve both the polar angle and the invariant mass resolutions. The z-chambers are arranged to form a barrel layer around the Jet chamber covering the polar angle $-0.72 < \cos\theta < 0.72$ and 94% of the azimuthal angle.

The central tracking system has a momentum resolution of [14]:

$$\frac{\sigma_{p_T}}{p_T} = \sqrt{(0.02)^2 + (0.0015\, p_T(\mathrm{GeV}))^2}, \tag{2.4}$$

where p_T is the transverse momentum, measured in the xy-plane. The average angular resolution is 0.3 mrad in ϕ and 1 mrad in θ.

The next element is the **Time-of-Flight detector**(TOF). This system generates trigger signals and, by measuring the time of flight from the interaction region, allows charged particle identification in the range 0.6-2.5 GeV. It also aids in the rejection of cosmic rays. The TOF system covers the barrel region $|\cos\theta| < 0.82$. It consists of 160 scintillation counters (6.8 m long and 45 mm thick) forming a barrel of mean radius 2.36 m, which is positioned outside and coaxial with the aluminum magnet coil.

Charged particles passing these scintillation counters [24], excite the atoms of the material which causes the emission of photons. The light is collected at both ends of each counter via 300 mm conical and cylindrical light guides glued directly to the photomultipliers. The output of these photomultipliers is proportional to the number of incident photons.

2.2.2 The Electromagnetic Calorimeter

The electromagnetic calorimeter (ECAL) detects and measures the energies and positions of electrons, positrons and photons ranging from tens of MeV to 100 GeV. It is designed as a total absorption detector mounted between the coil and the iron return yoke of the magnet. The ECAL is made of lead-glass blocks, which cover nearly all angles from the beam direction. The barrel and endcap lead glass systems together cover 98% of the solid angle. Lead glass was chosen for the electromagnetic calorimeter because of its excellent intrinsic energy resolution [14]. Since there are two radiation lengths of material in front of the lead glass, due mostly to the magnet coil and presurre vessel, most electromagnetic showers are initiated before the ECAL itself. The **presampling devices** are therefore installed in both the barrel and endcap regions immediately in front of the lead glass to provide measurements of the position and energy of electromagnetic showers which start in front on the lead glass.

The **barrel lead glass calorimeter** consists of a cylindrical array of 9440 lead glass block of 24.6 radiation lengths. It is located at a radius of 2455 mm, outside the magnet coil, covering the azimuthal angle of $|\cos\theta| < 0.82$. The energy resolution in the barrel is given by [14]:

$$\frac{\sigma_E}{E} = 0.2\% + \frac{6.3\%}{\sqrt{E}}, \tag{2.5}$$

where E is the electromagnetic energy in GeV. The **endcap electromagnetic calorimeter** consists of two dome-shaped arrays, each of 1132 lead glass blocks. It is located between the pressure bell of the central tracking system and the hadron calorimeter and covers the azimuthal angle of $0.81 < |\cos\theta| < 0.98$. The energy resolution in the endcaps is [14]:

$$\frac{\sigma_E}{E} = \frac{5\%}{\sqrt{E}} \tag{2.6}$$

2.2.3 The Hadron Calorimeter

The hadron calorimeter measures the energy of hadrons and helps in the identification of muons. The iron of the return yoke provides four or more interaction lengths of absorber over a solid angle of 97% of 4π. The yoke is segmented into layers, with planes of detectors between each layer, and forms a cylindrical sampling calorimeter about 1 meter thick. To achieve the coverage in solid angle, the hadron calorimeter is constructed in three parts; **barrel, endcaps** and the **pole tips**. Together they extend down to $|\cos\theta| \leq 0.99$.

The hadron calorimeter achieves a resolution of [14]:

$$\frac{\sigma_E}{E} \approx \frac{120\%}{\sqrt{E}} \tag{2.7}$$

2.2.4 The Muon detector

This detector is designed to identify muons. It is constructed as a barrel and two endcaps and covers 93% of the full solid angle. While muons penetrate in the muon detector and leave a single clean track, most hadrons are absorbed in the magnet return yoke. The **barrel muon detector** consists of 110 large-area drift chambers, each with 1.2 m wide and 99 mm deep. It covers an azimuthal angle $|\cos\theta| < 0.68$ for four layers and $|\cos\theta| < 0.72$ for one or more layers. The **muon endcaps** cover the angular range $0.67 < |\cos\theta| < 0.985$. At each end of the detector an area of about 150 square meters is covered with four layers perpendicular to the beam axis. The direction of the muon tracks is determined from the hit coordinates in these individual layers.

2.2.5 The Luminosity Measurement

The Luminosity of the colliding beams is determined by the observation of small angle Bhabha events, $\mathrm{e}^+\mathrm{e}^- \to \mathrm{e}^+\mathrm{e}^-$. The cross section of these events can be calculated in the framework of quantum electrodynamics QED, with a precision much better than 1% [16]. Moreover, the signature of these events is very clear. Thus the Bhabha processes are ideal to measure the luminosity.

The system to measure this parameter consists of two forward detectors and since 1993 of a Silicon Tungsten Calorimeter. The **forward detectors** measure the luminosity of LEP by detecting small-angle Bhabha scattering, and also tag electrons from $\gamma\gamma$ interactions. The **SiW Calorimeter** was proposed in 1991 as a improvement for OPAL and installed in the detector in 1993. The calorimeter was built to obtain a good energy-position resolution. A good position resolution is fundamental for a precise measurement of the acceptance on the calorimeter. A high energy resolution is important to separate real Bhabha events from the background processes.

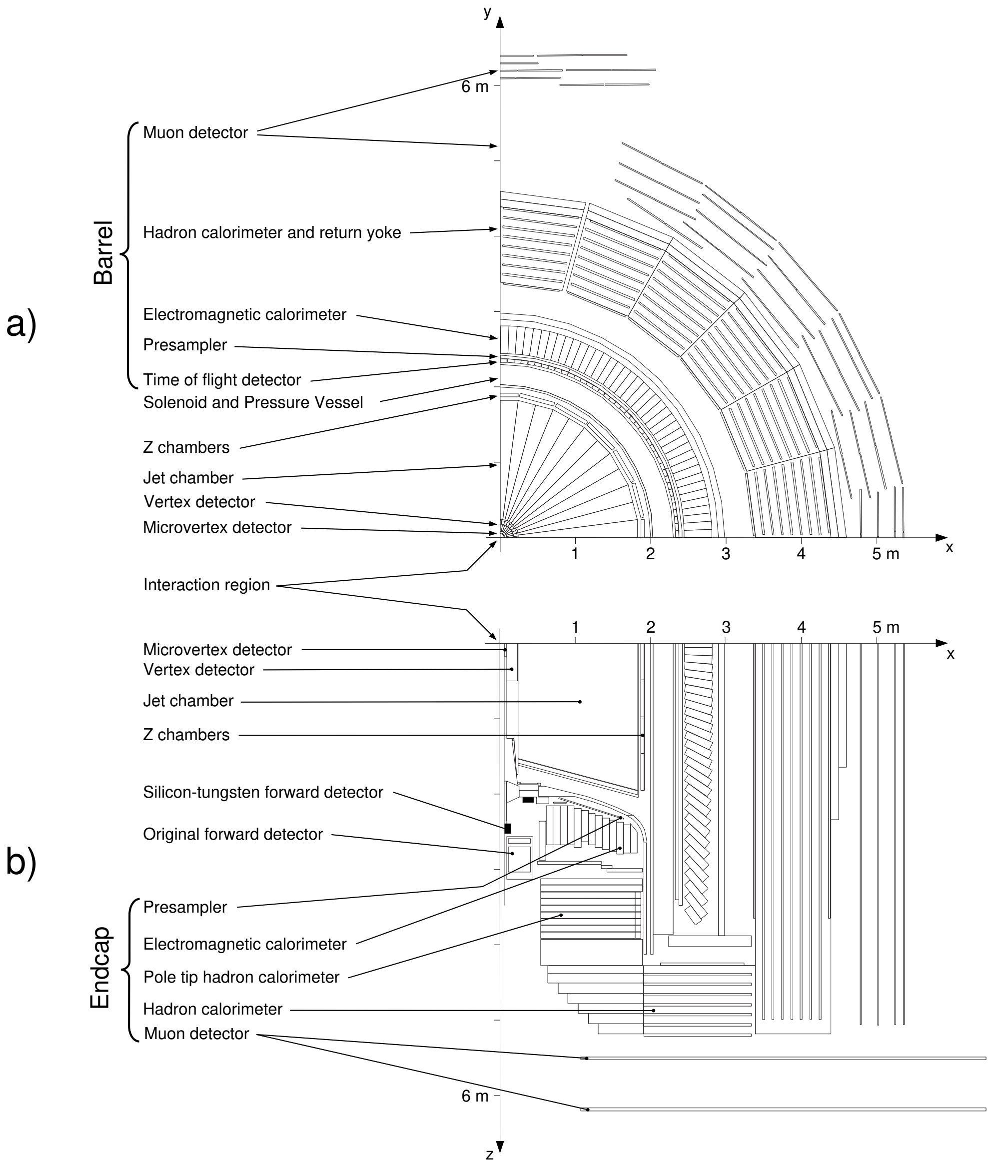

Figure 2.4: Cross section views of the OPAL detector. (a) in the r-θ plane. (b) along the beam-pipe; z-axis.

2.3 The Data Acquisition and the Trigger System

The first classification of the events coming from the e^+e^- collisions is performed during the **on-line** reconstruction. The detector consists of a trigger system to separate candidate events, according to the physics processes under consideration, from the background. The so obtained events are recorded and subjected to further analysis to perform additional events classifications during the **off–line** phase.

The **trigger** system is designed to provide high efficiency for the different physics processes and good rejection of backgrounds coming from cosmic rays, from interactions of the beam particles with the gas inside the beam pipe or the wall of the beam pipe, and from electronic noise in the detector. At LEP, a bunch crossing occurs typically every 22.2 μs. The data acquisition system cannot handle such an amount of data and the trigger system reduces therefore the 45 kHz bunch crossing rate to an event rate of 3-10 Hz.

The whole solid angle covered by the detector is divided in 144 overlapping bins, 6 in θ and 24 in ϕ. The subdetectors deliver trigger signals according to this binning. In addition, "stand-alone" signals are derived from total energy sums or track counting.

All the trigger signals are combined in the central trigger logic to decide whether an event is accepted or rejected. If the trigger logic accepts an event, the corresponding information from the subdetectors is read out and processed by the data acquisition system. After this, the event builder merges all the information coming from the subdetectors and passes the event to the filter, which monitors the quality of the data and classifies events according to their topology. The so obtained data are compressed and written to the filter disk, together with the event headers of all the events which reach the filter. All this information is passed to the ROPE farm, a group of workstations which perform the reconstruction of the events, taking into account the whole information emerging from the subdetectors. The reconstructed events are sent to the SHIFT farm in the central computing facility at CERN and recorded on magnetic tapes. These tapes are called DSTs (Data Summary Tapes) and contain the neccesary information to perform the off-line analysis which is explained in chapter 5.

2.4 The Monte Carlo Simulation

The simulation of the physics processes by the Monte Carlo package is an important tool for the data analysis. Monte Carlo simulation works in two steps described as follows:

- **Production of events.**

  The different Monte Carlo generators produce the four-momenta of the particles according to the properties of the process that is generated. This so called tree– or generator–level includes all the characteristics of the event which comes from e^+e^- collisions, as the W mass, M_W, and the W width, Γ_W. Chapter 5 gives a description of the different Monte Carlo generators used for this analysis.

- **Interactions with the detector.**

  The software package GOPAL [25] describes each component of the OPAL detector geometrically and the GEANT [26] package simulates the response of the detector, describing the interactions between the particles and the detector material. The output from GEANT is recorded in the same format as the data, to allow in the reconstruction package ROPE [27] a similar treatment of data and simulated events.

Chapter 3

The Standard Model

The Standard Model describes the fundamental constituents of matter and their interactions. This model is a gauge-invariant field theory based on the gauge group $\mathrm{SU}(3) \times \mathrm{SU}(2) \times \mathrm{U}(1)$ and describes the strong, the electromagnetic and the weak forces.

The electromagnetic force is successfully explained by the quantum electrodynamics (QED) [28]. This is a gauge theory based on the $\mathrm{U}(1)_{\mathrm{em}}$ local gauge transformations group, which leads to the conservation of the electric charge as a quantum number. The QED explains the interaction between charged particles as the exchange of a massless neutral particle, the photon.

The electromagnetic and weak interactions have been unified by the Glashow, Salam and Weinberg [1–3] model proposed in the late 1960s and described below. This theory is based on the $\mathrm{SU}(2) \times \mathrm{U}(1)$ local gauge transformations group, the $\mathrm{SU}(2)$ group is related to the weak isospin transformations (I) and the $\mathrm{U}(1)$ group to the weak hypercharge (Y). The theory was later proven to be renormalizable by t' Hooft and Veltman [4, 5].

The quantum chromodynamics (QCD) is a theory based on the SU(3) group of local transformations, which explains the strong color interaction between quarks [29–31]. The color is a quantum number with three possible values, say red, blue and green. The bosons which mediate the strong interaction between quarks are the gluons, each is carrying a color and an anticolor. In QCD, there are six types of charge (color and anticolour) and eight color charged mediator bosons. Quarks have been never observed as isolated particles and they can exist only in colorless combinations (a phenomenon called confinement) of colored objects, in the following configurations: $\mathrm{q\overline{q}}$ (mesons) and qqq (baryons).

The gravitation is the fourth interaction observed in nature and it is not included in the Standard model. Its unification with the other interactions is still one of the remaining open questions, which can lead to more general theories beyond this model.

The general characteristics of the Standard Model can be summarized as follows:

- The matter is made out of spin 1/2 particles called fermions: six leptons and six quarks. The leptons carry integer charge and these are the electron (e), the muon (μ) and the tau (τ). The muon and the tau are heavy versions of the electron. Each charged lepton has the corresponding neutral lepton called neutrino. The quarks carry fractional charges $+2/3|\mathrm{e}|$ or $-1/3|\mathrm{e}|$, where $|\mathrm{e}|$ is the value of the electrical charge of the electron. The quark flavors are denoted by u, d, s, c, b and t.[1]

- Leptons and quarks fall into three families classified according to their hypercharges and the third component of the weak isospin. All the matter is built from particles of the first family. Table 3.1 summarizes the three families for the leptons and quarks.

  In case of leptons, there is no cross-generation coupling, but in the case of quarks, the situation is not so simple. Although the generation structure is similar, the weak interaction do not strictly respect their separate identities, allowing cross generational couplings, described by the Cabbibo-Kobayashi-Maskawa matrix.

- The weak hypercharge is related to the weak isospin by the Gell-Mann-Nishjima relation:

  $$Q = I_3 + Y \tag{3.1}$$

  where Q is the electric charge.

- The Dirac field operator for each particle can be split into a left-handed and a right-handed operator. For the neutrinos however only the left-handed part can couple. Considering the symmetry group $\mathrm{SU}(2)_\mathrm{I} \times \mathrm{U}(1)_\mathrm{Y}$ for the electroweak interaction, the fermions are grouped in left-handed doublets and right-handed singlets according to the weak isospin I of the SU(2) group and the weak hypercharge of the U(1) group. Table 3.2 summarizes the classification of leptons and quarks together with their fundamental quantum numbers.

  Where d', s' and b' are the weak eigen–states which are related to the physical quarks d, s and b by the Cabbibo-Kowayashi-Maskawa matrix. In terms of this formulation, d', s' and b' are the eigen–states of the weak interaction whereas d, s and b are the mass eigen–states of the matrix.

- Interactions between elementary particles are described by the exchange of twelve spin-1 bosons, four bosons as the carriers of the electroweak force, γ, W^+, W^-, Z and eight massless gluons as the carriers of the strong force.

- The model invokes a spontaneous symmetry breaking process to give rise to the masses of Z and W^+, W^-. This process requires the existence of another spin-0 particle called the Higgs boson.

Due to the topic of the present thesis, only the electroweak sector will be explained here. A detail explanation of the QCD and QED can be found in [28, 32].

3.1 The Weak Interaction

A quantum field theory which explains an interaction should have the property of *renormalisability*, meaning that the amplitudes for different processes associated with an interaction should be nondivergent at high energies and to high orders in the coupling constant. The possibility of performing precision tests of the theory is based on this property which preserves its predictive

[1] These denotations are related to the words, up, down, strange, charm, botton (or beauty) and top (or truth).

Fermions	Families			Q
Leptons	$\begin{pmatrix}\nu_{\mathrm{e}}\\ \mathrm{e}^-\end{pmatrix}$	$\begin{pmatrix}\nu_{\mu}\\ \mu^-\end{pmatrix}$	$\begin{pmatrix}\nu_{\tau}\\ \tau^-\end{pmatrix}$	0 1
Quarks	$\begin{pmatrix}\mathrm{u}\\ \mathrm{d}\end{pmatrix}$	$\begin{pmatrix}\mathrm{c}\\ \mathrm{s}\end{pmatrix}$	$\begin{pmatrix}\mathrm{t}\\ \mathrm{b}\end{pmatrix}$	+2/3 -1/3

Table 3.1: Classification of the leptons and quarks families together with their electrical charges.

power also for beyond high order calculations [32, 33] A prototype of a renormalisable field theory is the QED explained briefly at the beginning of this chapter.

Historically, the prototype of a weak interaction process was the nuclear β-decay:

$$\mathrm{n} \rightarrow \mathrm{p} + \mathrm{e}^- + \overline{\nu}_{\mathrm{e}}$$

or in terms of quarks:

$$\mathrm{d} \rightarrow \mathrm{u} + \mathrm{e}^- + \overline{\nu}_{\mathrm{e}}$$

In this model, the interaction between the four fermions involved in the process is effectively pointlike and it is described by a coupling term $\mathrm{G_F}$ which is the Fermi constant. This model works properly at low energies, but a high energies (> 300 GeV), the cross section for such processes exceed the so called unitarity limit [2]. The fact that the dimension of the coupling constant $\mathrm{G_F}$ depends inverse on the energy, produces such divergences. It is therefore neccesary to redefine the weak interaction in terms of a dimensionless coupling constant [34].

The theories tried then, to explain such processes by the introduction of intermediate bosons in a similar way to the QED theory. Thus, the following features should have taken into account:

- If the interaction is explained as the interchange of bosons, these should be charged in order to explain the β^+ and the β^- decays.

- These intermediate bosons should be massive, since the reach of the interaction is small.

The introduction of intermediate charged vector bosons (called $\mathrm{W^+}$ and $\mathrm{W^-}$) does not eliminate however all the divergences and the situation is particular dramatic for weak and electromagnetic processes, in which the W boson production in the takes place in the final state as in $\nu\overline{\nu} \rightarrow \mathrm{W^+W^-}$ or $\mathrm{e^+e^-} \rightarrow \mathrm{W^+W^-}$ events. The cancellation of the divergences in such processes is reached by introducing a neutral boson (called Z). It is natural to assume that the same neutral boson eliminates the divergences in the weak and the electromagnetic processes. In such case it is clear that the weak coupling will have the same magnitude as the electromagnetic coupling.

[2] This limit is determined by the condition that the scattered intensity cannot exceed the incident intensity of any partial wave.

Fermions			I	I_3	Y
Leptons					
$\begin{pmatrix} \nu_e \\ e^- \end{pmatrix}_L$	$\begin{pmatrix} \nu_\mu \\ \mu^- \end{pmatrix}_L$	$\begin{pmatrix} \nu_\tau \\ \tau^- \end{pmatrix}_L$	1/2 1/2	1/2 -1/2	-1/2 -1/2
e^-_R	μ^-_R	τ^-_R	0	0	-1
Quarks					
$\begin{pmatrix} u \\ d' \end{pmatrix}_L$	$\begin{pmatrix} c \\ s' \end{pmatrix}_L$	$\begin{pmatrix} t \\ b' \end{pmatrix}_L$	1/2 1/2	1/2 -1/2	1/6 1/6
u_R d'_R	c_R s'_R	t_R b'_R	0 0	0 0	2/3 1/3

Table 3.2: Classification of the left and right–handed leptons and quarks and their fundamental quantum numbers.

Introducing this neutral boson, the divergences dissapear but there is still a residual divergence if the fermion is considered a massive particle. This divergence can be canceled by the introduction of further scalar particles, with a special coupling proportional to the fermion mass. These are the so called Higgs scalars.

3.2 The Electroweak Interaction

The Glashow, Weinberg and Salam model unifies the electromagnetic and the weak forces in an electroweak interaction based on the local $\mathrm{SU}(2)_\mathrm{I} \times \mathrm{U}(1)_\mathrm{Y}$ group of transformations.

This theory postulates four massless bosons, arranged in a triplet and a singlet as members of multiplets of the weak isospin (I) and the weak hypercharge (Y) [33]. Table 3.3 summarizes these multiplet members:

I	Group	Multiplet
1	SU(2)	$\mathbf{W}_\mu = \mathrm{W}^1_\mu, \mathrm{W}^2_\mu, \mathrm{W}^3_\mu$
0	U(1)	B_μ

Table 3.3: Triplet and singlet members of multiplets of the weak isospin (I) and hypercharge (Y).

The gauge bosons are endowed with masses by means of a spontaneous symmetry breaking process, which leaves the renormalization of the theory intact as it is explained in the next section. The massive bosons are denoted by $\mathrm{W}_\mu^+, \mathrm{W}_\mu^-$ and Z_μ, and the fourth, the photon, A_μ remains massless.

The interaction between the leptons and the quarks to the intermediate bosons can be written by the Lagrangian:

$$L = gJ^\mu \cdot W_\mu + g' J^{Y^\mu} B_\mu \tag{3.2}$$

where $\mathbf{J}_\mu = \mathbf{J}_\mu^\mathbf{1},\ \mathbf{J}_\mu^\mathbf{2},\ \mathbf{J}_\mu^\mathbf{3}$ and $\mathrm{J}_\mu^\mathrm{Y}$ are the fermionic currents of weak isospin and hypercharge, $\mathbf{W}_\mu$ and B_μ are the potentials associated to the boson fields and g, g' are the coupling constants.

Taking into account the Gell-Mann-Nishjima relation between the electric charge, the hypercharge and the third component of the weak isospin, the weak hypercharge can be written as:

$$J_\mu^Y = J_\mu^{em} - J_\mu^3 \tag{3.3}$$

where $\mathrm{J}_\mu^\mathrm{em}$ is the electromagnetic current, and J_μ^3 is the third component of the weak isospin.

The physical bosons can be expressed as combinations of the component of the isotriplet of vector fields $\mathbf{W}_\mu$ and the singlet B_μ. These fields are:

$$W_\mu^\pm = \frac{1}{\sqrt{2}}[W_\mu^{(1)} \pm iW_\mu^{(2)}] \tag{3.4}$$

$$W_\mu^{(3)} = \frac{gZ_\mu + g'A_\mu}{\sqrt{g^2 + g'^2}} \qquad B_\mu = \frac{-g'Z_\mu + gA_\mu}{\sqrt{g^2 + g'^2}} \tag{3.5}$$

where $\mathrm{W}_\mu^{(3)}$ and B_μ are orthogonal.

Introducing these expressions in the Lagrangian, equation 3.2, with the Weinberg angle defined by:

$$\frac{g}{g'} = \tan\theta_w, \tag{3.6}$$

the Lagrange function for this interaction becomes:

$$L = \frac{g}{\sqrt{2}}(J_\mu^- W_\mu^+ + J_\mu^+ W_\mu^-) + \frac{g}{\cos\theta_w}(J_\mu^{(3)} - \sin^2\theta_w J_\mu^{em})Z_\mu + g\sin\theta_w J_\mu^{em} A_\mu \tag{3.7}$$

The last equation contains three terms, which correspond to a weak charged current, a weak neutral current and an electromagnetic neutral current, whose coupling constant should be the electromagnetic coupling *e*:

$$e = g\sin\theta_w \tag{3.8}$$

At low energies the Fermi model of the weak interaction is reproduced and the coupling of the $W^{\pm}$ bosons is related to the Fermi constant G_F as:

$$\frac{G_F}{\sqrt{2}} = \frac{g^2}{8M_W^2} \tag{3.9}$$

Introducing now the relation 3.8 it follows that:

$$M_{W_\pm} = (\frac{e^2\sqrt{2}}{8G\sin^2\theta_w})^{1/2} = \frac{37.4}{\sin\theta_w}\text{GeV}. \tag{3.10}$$

The predicted Z mass is obtained from M_W by the relation:

$$\cos\theta_w = \frac{M_W}{M_Z} \tag{3.11}$$

3.3 The Higgs Mechanism

There is still a remaining question in the model concerning the mechanism which gives rise to the gauge bosons and fermion masses. The simplest idea could be to add mass terms for these bosons to the Lagrange density. This procedure, however, violates the local gauge invariance and leads to a non renormalizable theory [32].

Salam and Weinberg presented a method based on a spontaneous symmetry breaking to generate the masses for the W^+, W^- and Z bosons. This phenomenon occurs when the fundamental equations of a system have a symmetry, which is not visible in the ground state. The suggested mechanism requires additional scalar fields, called Higgs fields. In the minimal Standard model it is enough to introduce two complex scalar fields, which form a doublet under the weak isospin group SU(2):

$$\phi(x) = \begin{pmatrix} \phi_1(x) \\ \phi_2(x) \end{pmatrix} \tag{3.12}$$

The next step is to look for a Lagrange density, $\mathcal{L}_\phi$ which contains the coupling of this scalar doublet field to the gauge field and is invariant under the SU(2) transformations. With these requirements the Lagrange density has the following form:

$$\mathcal{L}_\phi = (D_\mu\phi^\dagger)(D_\mu\phi) - V(\phi), \tag{3.13}$$

where D_μ is the covariant derivate defined as:

$$D_\mu = \delta_\mu - ig' I_a W_\mu^a - i\frac{g}{2}B_\mu \tag{3.14}$$

g and g′ are the gauge couplings for SU(2) and U(1) and $V(\phi)$ is the Higgs field self-interaction defined by:

$$V(\phi) = \mu^2\phi^\dagger\phi + \frac{1}{4}\lambda(\phi^\dagger\phi)^2$$

where μ and λ are free parameters. The first term of the Lagrangian is assumed to be positive defined. The minimum of the energy corresponds therefore to the minimum of the potential which occurs at:

$$\phi \equiv v = \sqrt{\frac{\mu^2}{\lambda}} \tag{3.15}$$

v is the vacuum expectation value of the scalar boson field ϕ and $\mathrm{V}(v) = -\mu^4/4\lambda$, so that V is a non-zero constant in the ground state.

Considering a perturbation expansion in lowest order around the vacuum minimum v for this scalar field, it is possible to obtain from the Lagrange density, the mass associated to this scalar particle:

$$M_H = \sqrt{2\lambda v^2} = \sqrt{2}\mu \tag{3.16}$$

The kinematic term of the gauge-invariant Higgs Lagrangian gives rise to mass terms for the vector bosons, which depend on the gauge coupling g and g' and the Higgs vacuum term v:

$$M_\gamma = 0 \tag{3.17}$$

$$\mathrm{M_W} = \frac{gv}{2}$$

$$M_Z = \frac{v}{2}\sqrt{g^2 + g'^2}$$

Finally, the fermion masses are obtained from the Yukawa coupling of the Higgs boson to the fermions, which introduces additional terms in the total Lagrange function.

Chapter 4

The W Physics at LEP2

This chapter presents a general overview of the W boson physics performed at LEP2. The first section introduces the fundamental measurements and the next section explains the W pair production cross section and other four fermion processes which contribute to the total cross section. Finally, the determination of the width, Γ_{W} and the mass, $\mathrm{M_W}$ of the W are explained at the end of the chapter.

4.1 Introduction

The LEP $\mathrm{e^+e^-}$ collider at CERN is an ideal environment to study the properties of the gauge bosons of the Standard Model in the electroweak sector.

The recorded data during the second phase of the accelerator program, LEP2, have improved our knowledge of the Standard Model from two fundamental measurements [9]:

- **Direct measurement of the W mass** which was possible before only in hadron colliders. Since the W mass is related directly to the fundamental parameters of the electroweak sector, a high precision measurement of this mass provides stringent tests of the Standard Model. When it is combined with the mass of the Z obtained from LEP1, the W mass can be used to constrain the mass of the Higgs boson [35, 36].

- **The structure of the trilinear gauge couplings** of the W to Z and γ bosons. In the Standard Model, couplings have the Yang-Mills form, which leads to a proper high-energy behavior of the W pair cross section. Since these couplings appear in the non-abelian structure of the Standard Model, their measurement is essential for its direct confirmation [37].

  Couplings which are different to the Yang-Mills form are called anomalous or non-standard. They lead to high energy cross section and a violation of the unitarity. The center–of–mass energy at LEP is too low to see a deviating energy behaviour, however it is still possible to estabilish limits on the anomalous triple gauge couplings by studing both the total W pair cross section as a function of the center–of–mass energy and the angular distribution of the W bosons and their decays. In particular, the angular distribution of the W production is sensitive to non-standard couplings.

4.2 The W Pair Production

The W pair production from e^+e^- collisions is described in the lowest order of the perturbation theory by three different contributions shown in figure 4.1. The first diagram (left) shows the interchange of a neutrino in t-channel (abelian diagram). The second and the third diagrams (right) show the production of a virtual γ / Z in s-channel (non-abelian diagram [1]).

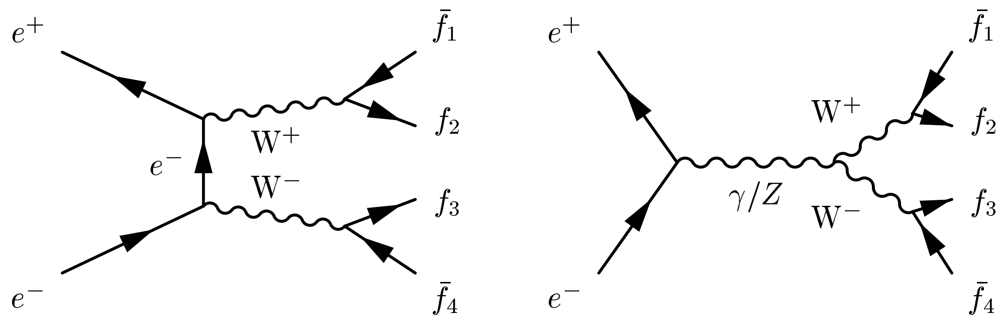

Figure 4.1: Feynman diagrams for the W pair production. Abelian diagram (left). Non-abelian diagrams (right).

In a first step, the calculation of the cross section can be performed at the so called *on-shell Born-level* [9]. At this order the W bosons are stable and the cross section has an edge like rise at $\sqrt{s} = 2M_W$, as shown in figure 4.2. This is, however, only an approximation since it neglects the width of the W boson.

Taking this width into account, the total cross section is given by:

$$\sigma^{off-shell}(s) = \int_0^s ds_1 \int_0^{(\sqrt{s}-\sqrt{s_1})^2} ds_2 \; \mathcal{BW}(M_W, \Gamma_W, s_1) \; \mathcal{BW}(M_W, \Gamma_W, s_2) \; \sigma_0(s, s_1, s_2) \tag{4.1}$$

where s_1 and s_2 are the invariant masses and $\mathcal{BW}$ represents the relativistic Breit-Wigner for each W boson:

$$\mathcal{BW}(M_W, \Gamma_W, s) = \frac{1}{\pi}\frac{\Gamma_W}{M_W}\frac{s}{(s - {M_W}^2)^2 + s^2\frac{{\Gamma_W}^2}{{M_W}^2}}, \tag{4.2}$$

σ_0 is here the Born level contribution, which can be written as the quadratic sum of the individual amplitudes of the Feynman diagrams shown before.

Moreover, it is neccesary to include radiative corrections due to initial and final state radiations [2] (ISR and FSR) [8,9]. ISR is particularly important because it decreases the center-of-mass energy of the system. This correction has an important effect in the determination of the W mass by a reconstruction method (see section 4.4.1), because the method uses the total center-of-mass

[1] Because of the coupling of the three gauge bosons (either WWZ or WWγ).

[2] Emission of one or more photons on the initial or the final states.

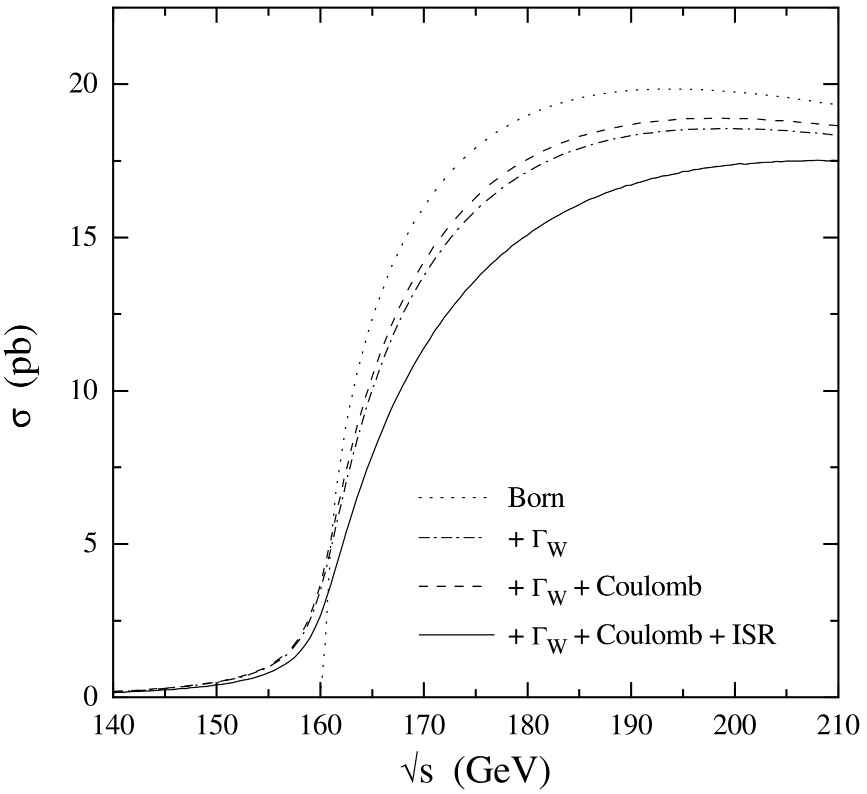

Figure 4.2: Cross-section for $e^+e^- \rightarrow W^+W^-$ events in various approximations: (1) Born (*on-shell*) cross-section (dotted line). (2) Born (*off-shell*) cross-section (dotted dashed line). (3) First order Coulomb corrections (dashed line). (4) Initial state radiation (solid line).

energy information to improve the mass resolution. The exact knowledge of the energy distribution of ISR photons is therefore neccesary.

A second important correction at threshold is the so called *Coulomb Singularity*, which leads to an interchange of low energetic photons between the W bosons. The exchange of a soft photon distorts the lineshape of the W^+W^- production. In the case of the resonant W pair cross-section, the so called CC03 diagrams [3], the Coulomb singularity gives rise to a correction factor which reaches its maximal value of $\approx 5.7\%$ at the nominal threshold and drops smoothly above the threshold, amounting to 2.4% at $\sqrt{s}$ = 176 GeV and only 1.8% at 190 GeV. Figure 4.3 shows the W-pair production cross section as a function of the center-of-mass energies measured at LEP [38]. The results obtained are consistent with the Standard Model expectation [10,38,39].

[3]These are the three resonant W pair diagrams shown in figure 4.1.

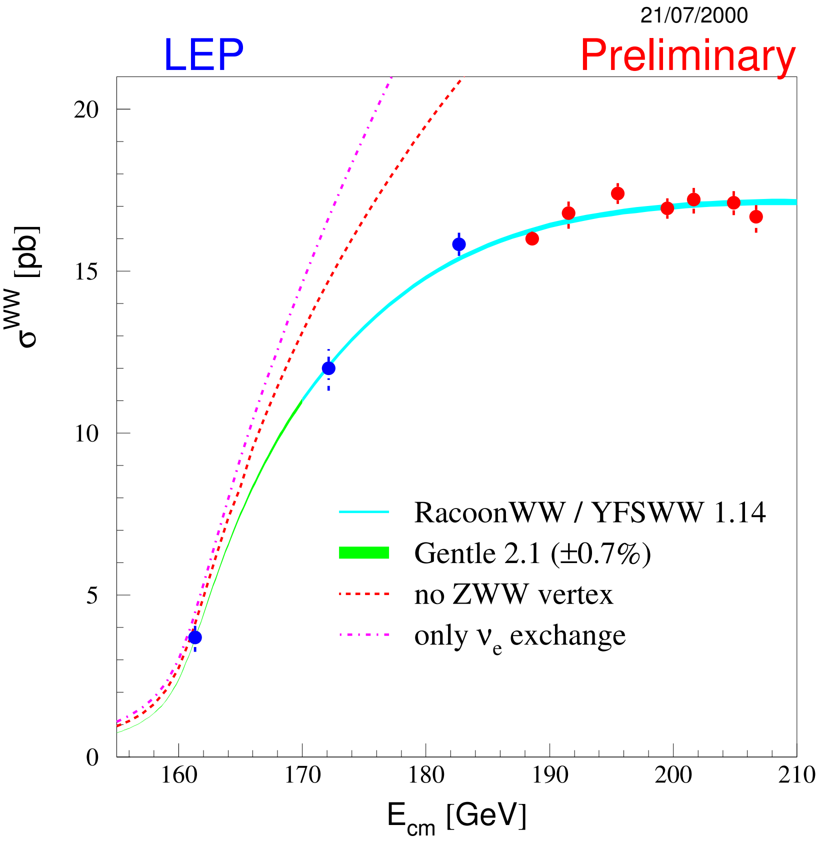

Figure 4.3: Measurements of the W-pair production cross section compared to the predictions of RACOONWW [40], and YFSWW3 [41] and GENTLE [42]. The shaded area represents a $\pm 0.4 - 0.7\%$ ($\pm 0.7\%$) uncertainty on the predictions for $\sqrt{s} > 170$ GeV ($\sqrt{s} < 170$ GeV) [38].

4.2.1 Four-Fermion Processes

The resonant CC03 W pair production diagrams, $e^+e^- \rightarrow W^+W^- \rightarrow 4f$, shown in figure 4.1, belong to the general group of four–fermion processes in which four fermions are observed in the final state, $e^+e^- \rightarrow X \rightarrow 4f$, with the same initial and final state but different intermediate states and all these diagramas give sizeable contributions.

Figure 4.4 shows all these contributions for the cross section classified in abelian and non-abelian. The diagrams (a) and (f) contribute to the CC03 diagrams. The resonant CC03 diagrams can interfere with the other four-fermion processes and these interferences should be taken into account in the determination of the total cross-section and further analysis of the W boson. Nevertheless, the usage of the CC03 diagrams only in the W analysis instead of the full set of four–fermion diagrams is a good approximation since the contributions of the other diagrams are small due to the fact that most of the four–fermion contributions are situated in different phase space regions than the W–pair events. One example of these interferences is given by the $\mathrm{e^+e^-} \rightarrow$ qq'eν process which is compatible with the diagram (e) in figure 4.4. In this process two quarks (in the case that $\mathrm{B_3} = \mathrm{Z},\ \gamma$) or a charged lepton and the corresponding neutrino (in the case that $\mathrm{B_3} = \mathrm{W}$) appear in the final state. This process is compatible with diagrams (a) and (f) as final states are identical and therefore they interfere and contribute to the cross section of the W pair production. The dominant non–CC03 contribution to this process comes from diagram (e).

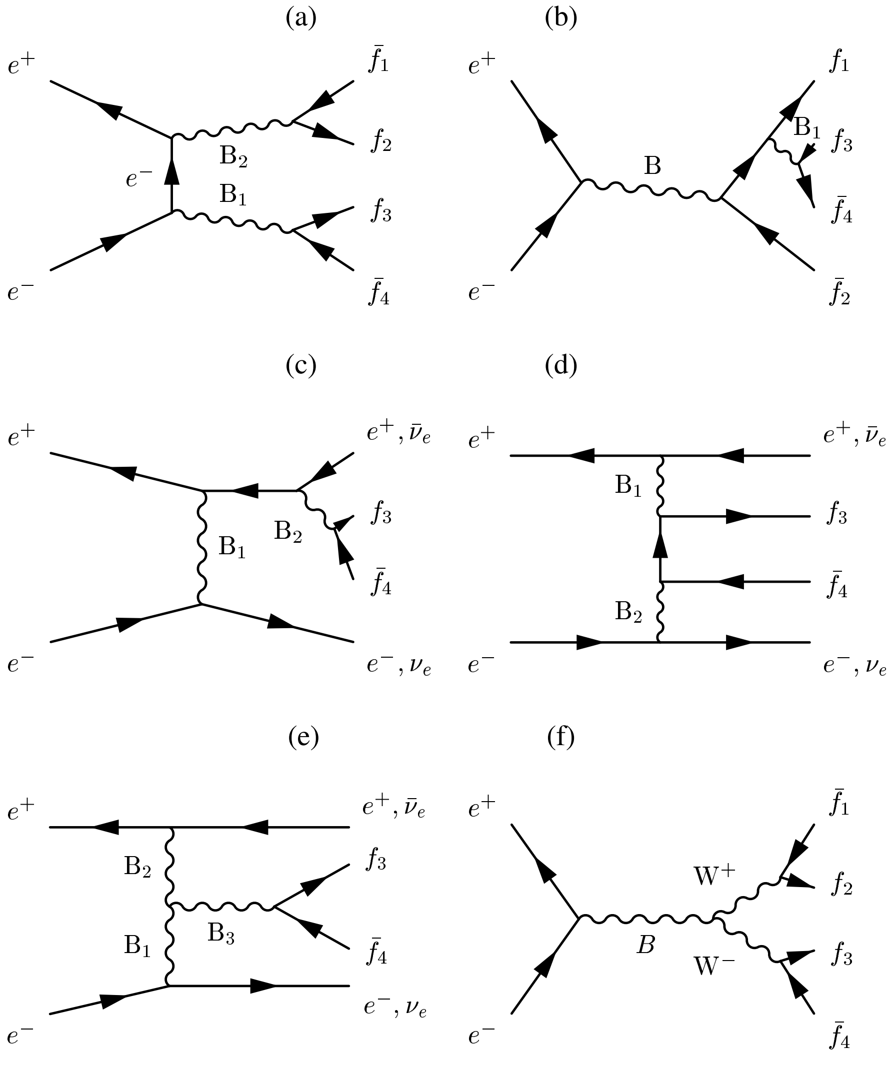

Figure 4.4: Four fermion Feynman diagrams. (a), (b), (c) and (d) corresponds to the abelian classes. (e) and (f) are the non-abelian classes. B's denote the following: $\mathrm{B} = \mathrm{Z},\ \gamma,\ \mathrm{B_1},\ \mathrm{B_2},\ \mathrm{B_3} = \mathrm{Z}, \gamma, \mathrm{W^+W^-}\ +\ \text{Higgs Graphs}$.

The fundamental Feynman diagrams for the most important four-fermion background processes are shown on figure 4.5:

- **Z(γ)-pair production (ZZ)(Zγ) (γ γ)**
  This process is shown in figure 4.5(a). Below a center-of-mass energy $\sqrt{s}$ = $2\mathrm{M_Z}$, this process has only a small cross section less than 0.4 pb. Since 1997, when the center-of-mass energy of LEP increases over 180 GeV, this channel is dominated by the production of two real Z bosons, reaching a cross section of about 1 pb. This ZZ production is an important background source for the hadronic and leptonic channels.

- **Single Z production** (Zee)
  In this case the intermediate photon is quasi-real and normaly only one $\mathrm{e^-}$ is detected (see figure 4.5(b)). The process has a high cross section and is an important background for the semileptonic and leptonic channels.

- **Single W production** (Weν)
  The quasi-real γ in the intermediate state causes the scattering angle of the $\mathrm{e^-(e^+)}$ to be generally very low (see figure 4.5(c)), in most cases it goes along the beam pipe and is not detected. If it is, however, observed in the detector, it leads to an indistinguible background event, for final states with $\mathrm{e^-}$-ν_e pair.

- **Multi-peripheral events (Two photon production)**
  This process, shown in figure 4.5(d) has a very high cross section, but since the fermion pairs have in general a low mass its contribution to the phase space relevant to the measurement of W properties is relative small. Because of the small angle scattering of $\mathrm{e^-}$ and $\mathrm{e^+}$ these particles go normally along the beam pipe and are not detected. These events are an important source of background in case of the fully leptonic channel.

Figure 4.6 shows the cross section of the most important processes as function of the center-of-mass energies at LEP2.

4.2.2 Two-Fermion Processes

Another important source of background events comes from two fermion processes, in which an intermediate Z/γ decays into a pair of fermion-antifermion. Figure 4.7 shows the Feynman diagrams for such a process.

In such processes the initial state radiation corrections are very important. In case of $\mathrm{q\overline{q}}$ events typically 75% of them have hard ISR such that $\sqrt{s} \approx \mathrm{M_Z}$ (called radiative return events). The cross section for these processes is high, if the energy of the photon is:

$$E\gamma = \frac{\mathrm{s} - \mathrm{M_Z}^2}{2\sqrt{\mathrm{s}}}. \tag{4.3}$$

However, these processes are easy to reject, by a determination of the effective $\sqrt{s}$.

For the fully hadronic $\mathrm{W^+W^-}$ channel, the non-radiative processes are an important background, since the primary quarks can emit energetic gluons, giving rise to events with more than two jets in the final state.

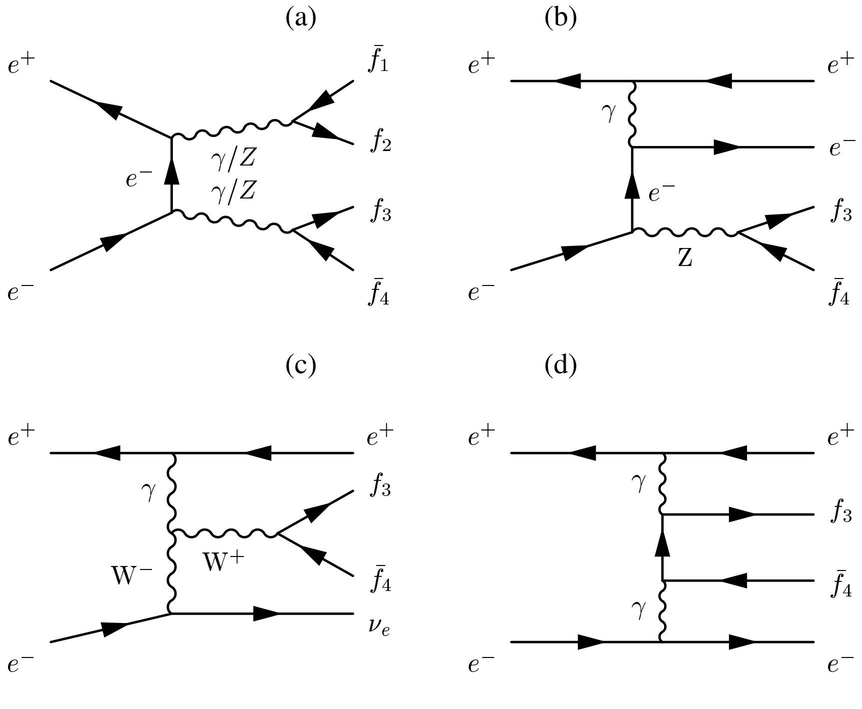

Figure 4.5: Background processes for the WW pair production.

4.3 The Width of the W Boson

As discussed in the last section, the width of the W is a crucial ingredient for the (off-shell) W pair production cross section, especially in the threshold region. Γ_{W} is determined by the coupling of the fermions and is related to $\mathrm{M_W}$ in the Standard Model.

In case of W decays to leptons ($\mathrm{W} \to \mathrm{e}\nu_{\mathrm{e}}$, $\mathrm{W} \to \mu\nu_\mu$, $\mathrm{W} \to \tau\nu_\tau$), there is no mixture between the individual generations. In hadronic decays, the W boson couples to u-d quarks and the mixture between the generations is determined by the Cabibbo-Kobayashi-Maskawa (CKM) Matrix $\mathrm{V_{ij}}$. The total width is now obtained as a sum of the individual contributions. In a first step, at Born-level (without radiative corrections), and neglecting fermion masses which are small compared to $\mathrm{M_W}$, the partial width for a decay of a W boson to a pair of fermions $f_i\overline{f'}_i$ is given by:

$$\Gamma_{\mathrm{W}}{}^{Born}(f_i, \overline{f'}_i) = \frac{\alpha}{12\sin\theta_W}\mathrm{M_W}\begin{cases} 1 & \text{for leptons,} \\ N_C|V_{ij}|^2 & \text{for quarks,} \end{cases} \tag{4.4}$$

where θ_W is the Weinberg angle, α the finestructure constant, $N_C = 3$ to take into account the different color charges of the quarks and $|V_{ij}|^2$ are the elements of the CKW matrix. The decay of the W boson in a top quark is forbidden since the mass of this quark is about two times larger than the W mass. From the remainder six hadronic decays, only two modes give sizeable contributions to the W width; the $\mathrm{W} \to \mathrm{ud}$ and $\mathrm{W} \to \mathrm{cs}$ decays. Together with the leptonic decays $\mathrm{W} \to \mathrm{e}\nu_{\mathrm{e}}$, $\mathrm{W} \to \mu\nu_\mu$ and $\mathrm{W} \to \tau\nu_\tau$ and neglecting other contributions, the total width

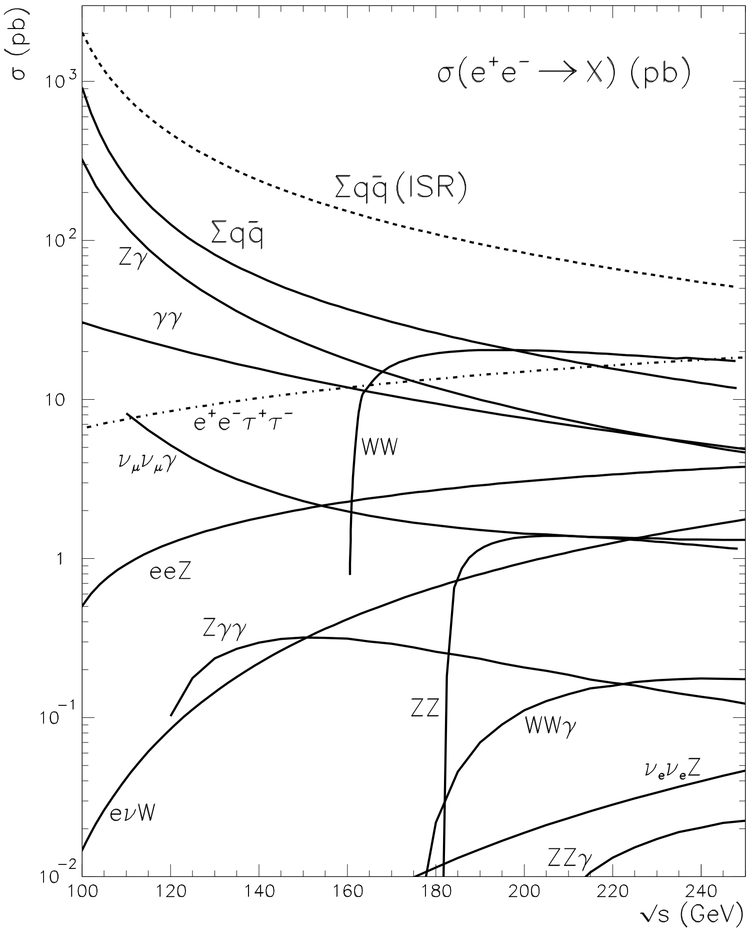

Figure 4.6: Cross sections for some typical standard model processes.

can be written in a first approximation as:

$$\Gamma_{\mathrm{W}} \approx (3 + 2 \times 3)\frac{\alpha \mathrm{M_W}}{12\sin^2\theta_W} = \frac{3\alpha}{4\sin^2\theta_W}\mathrm{M_W} \tag{4.5}$$

Electroweak corrections can be more easily taken into account, defining the lowest order of Γ_{W} in terms of the so called G_μ scheme (G_μ is the Fermi constant) , which uses $\mathrm{M_W}$, G_μ and $\mathrm{M_Z}$ instead of $\sin\theta_{\mathrm{W}}$ and α. These corrections remain below 0.5% of the total width.

Further QCD radiative corrections for the hadronic decay modes are practically constant and equal to $2\alpha_s(M_W^2)/3\pi$ [9]. Taking into account these corrections, the total W width can now be

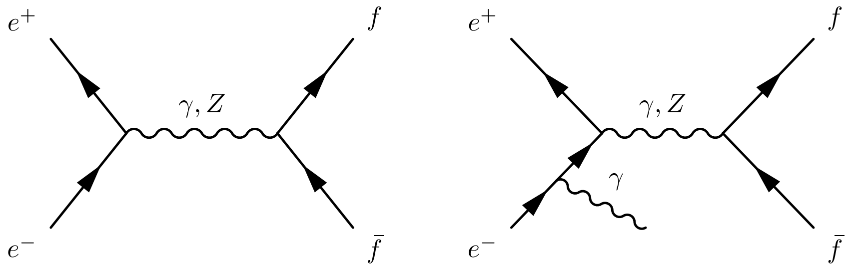

Figure 4.7: Feynman diagrams for two fermion events.

written as:

$$\Gamma_{\mathrm{W}} \approx \frac{G_\mu {\mathrm{M_W}}^3}{2\sqrt{2}\pi}\left(1 + \frac{2\alpha_s({\mathrm{M_W}}^2)}{\pi}\right) \tag{4.6}$$

The experimental determination of Γ_{W} has not achieved a high precision. The detectors CDF and D0 at TEVATRON at Fermilab have determined Γ_{W} by an indirect measurement, comparing the well known width of the Z in leptonic decays with the corresponding Γ_{W}. The result of this indirect measurement is [43]:

$$\Gamma_{\mathrm{W}} = 2.043 \pm 0.092 \text{ GeV}.$$

A second group of measurements performed in CDF and D0 determine Γ_{W} by a direct method based on the transverse leptonic mass [43]:

$$\Gamma_{\mathrm{W}} = 2.11 \pm 0.32 \text{ GeV}.$$

Measurements performed by the four LEP experiments yield a value of [44]:

$$\Gamma_{\mathrm{W}} = 2.12 \pm 0.11 \text{ GeV}.$$

The results of the four LEP experiments are shown in Figure 4.8.

4.4 The Mass of the W Boson

At LEP1, the W mass can be determined indirectly from the relation between $\mathrm{M_W}$, $\mathrm{M_Z}$ and the Fermi constant G_μ, which is known with high accuracy from the decay of the muon. This relation is given by:

$$G_\mu = \frac{\alpha\pi}{\sqrt{2}M_W^2(1 - M_W^2/M_Z^2)}\frac{1}{1 - \Delta r} \tag{4.7}$$

where Δr parameterizes the radiative corrections which depend on the mass of the top quark, $\mathrm{m_t}$, and the mass of the Higgs boson, $\mathrm{m_H}$. Figure 4.9 shows the first order corrections to the W propagator.

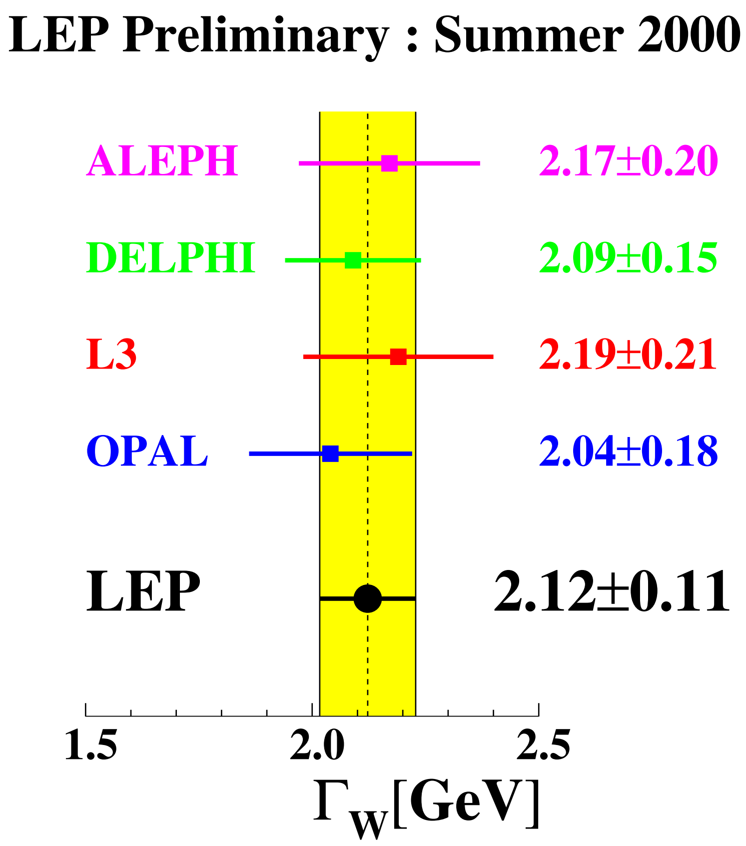

Figure 4.8: Combined results for the measurements of the W width compared to the results obtained by the four LEP collaborations [44].

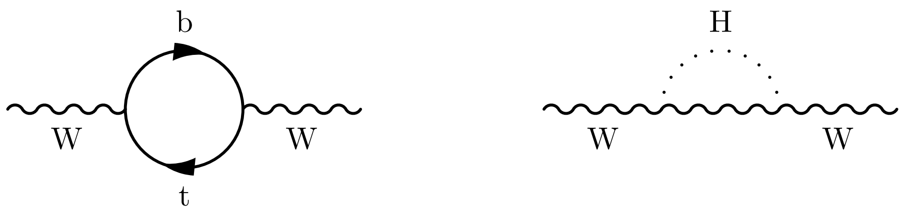

Figure 4.9: First order corrections to the W propagator.

A direct measurement of $\mathrm{M_W}$ together with a measurement of $\mathrm{m_t}$ allows an estimation of $\mathrm{m_H}$. A precise determination of $\mathrm{M_W}$ can therefore be used to constrain further the range of $\mathrm{m_H}$. Figure 4.10 shows the world average $\mathrm{M_W}$ measurement plotted versus $\mathrm{m_t}$ obtained from the CDF and D0 experiments. The solid contour denotes indirect limits derived from electroweak data for LEP1, SLD and neutrino experiments. The dashed line corresponds to the direct measurements for LEP2 and TEVATRON. The intersection with the bands corresponds to the limits of the Higgs boson.

The combination of direct measurements of $\mathrm{M_W}$ from LEP2 and from hadron colliders currently gives [45]:

$$\mathrm{M_W} = 80.436 \pm 0.037 \ \mathrm{GeV}.$$

The direct measurement is consistent with the indirect value obtained from lower energy data measurements at $\sqrt{\mathrm{s}} \approx \mathrm{M_Z}$ [45]:

$$\mathrm{M_W} = 80.386 \pm 0.025 \ \mathrm{GeV}.$$

It is expected that the ultimate LEP precision on $\mathrm{M_W}$ will be approximately 30 MeV when all data are included and combining the results of the four experiments.

4.4.1 General Methods to Determine $\mathrm{M_W}$ at LEP2

The two main methods to measure $\mathrm{M_W}$ from $\mathrm{W^+W^-}$ decays are now described. These methods are based on the sensitivity of $\mathrm{M_W}$ to the cross section shape of the $\mathrm{W^+W^-}$ production close to the threshold ($\sqrt{\mathrm{s}} = 161 \ \mathrm{GeV}$) and on a kinematic reconstruction of the decay products ($\sqrt{\mathrm{s}} > 161 \ \mathrm{GeV}$). For leptonic decays, a full reconstruction of the event is not possible due to the two neutrinos in the final state.

Threshold Cross-Section Measurement

This method exploits the fact that the $\mathrm{W^+W^-}$ production cross section increases rapidly at $\sqrt{\mathrm{s}} = 2\mathrm{M_W}$. The threshold method is based on the comparison of the absolute cross section measurement with a theoretical calculation which has $\mathrm{M_W}$ as the free parameter. The theory predicts the cross section with high accuracy and radiative corrections are well under control. Table 4.1 shows the results obtained by the four experiments with the threshold cross section method [46].

Experiment	$\mathrm{M_W}$ (threshold)/GeV
ALEPH [47]	80.14 ± 0.35
DELPHI [48]	80.40 ± 0.45
L3 [49]	$80.80\left(^{+0.48}_{-0.42}\right)$
OPAL [50]	$80.40\left(^{+0.46}_{-0.43}\right)$

Table 4.1: W mass measurements from the $\mathrm{W^+W^-}$ threshold cross section at $\sqrt{\mathrm{s}} = 161 \ \mathrm{GeV}$. The errors include statistical and systematic contributions.

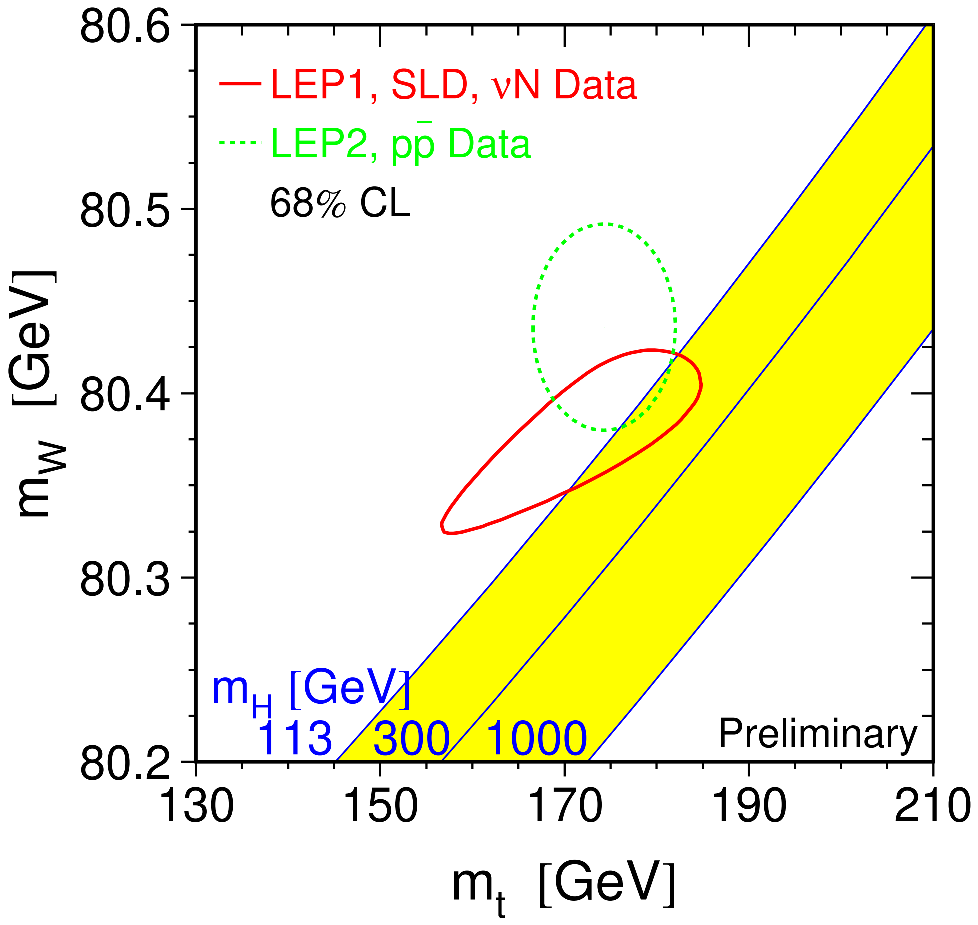

Figure 4.10: The solid line represents the indirect measurements from electroweak data. The dashed line corresponds to the direct measurements form LEP2 and TEVATRON.

The W boson mass measured at LEP from the data recorded at threshold for W pair production yields to [46]

$$\mathrm{M_W(threshold) = 80.40 \pm 0.20(stat.) \pm 0.07(syst.) \pm 0.03(LEP)\ GeV.}$$

Direct Reconstruction of $\mathrm{M_W}$

The determination of $\mathrm{M_W}$ via a direct reconstruction is performed in two stages. Firstly, the invariant masses of the W decay products are reconstructed on an event-by-event basis. The precision of the reconstructed mass is degraded due to the limited detector resolution. Kinematic fits [4] are therefore used to improve the mass resolution and to reject the background. Fits to the resulting mass spectra to obtain $\mathrm{M_W}$ are performed in OPAL using three different techniques:

- A Monte Carlo reweighting technique which compares fully simulated [5] mass distributions to observed mass spectra [51].

- The convolution method uses the convolution of the single event error information with a semianalytical function in an unbinned maximum likelihood fit [51–53]. The underlying likelihood parent distribution takes into account the effects of ISR on the mass reconstruction.

- An analytic fit to the measured mass spectrum using an unbinned likelihood function to determine $\mathrm{M_W}$. The method employs a parameterization based on a Breit-Wigner function [54].

The direct reconstruction can be used only for hadronic and semileptonic events. Table 4.2 shows the results obtained by the four experiments of LEP with a direct reconstruction. Figure 4.11 shows the comparisons between these results.

Experiment	$\mathrm{W^+W^-} \to \mathrm{q_1\overline{q}_2}\ell\nu_\ell$	$\mathrm{W^+W^-} \to \mathrm{q_1\overline{q}_2 q_3\overline{q}_4}$	Combined
ALEPH [55,56]	$80.435 \pm 0.063 \pm 0.048$	$80.467 \pm 0.064 \pm 0.057$	$80.449 \pm 0.045 \pm 0.047$
DELPHI [57,58]	$80.381 \pm 0.088 \pm 0.048$	$80.372 \pm 0.064 \pm 0.063$	$80.380 \pm 0.053 \pm 0.047$
L3 [59,60]	$80.273 \pm 0.089 \pm 0.046$	$80.461 \pm 0.077 \pm 0.069$	$80.362 \pm 0.058 \pm 0.052$
OPAL [61,62]	$80.510 \pm 0.067 \pm 0.031$	$80.408 \pm 0.066 \pm 0.100$	$80.486 \pm 0.053 \pm 0.039$

Table 4.2: W mass measurements from direct reconstruction ($\sqrt{\mathrm{s}}$ = 172-202 GeV). Results are given for the semi-leptonic, hadronic channels and the combined value. The errors are statistical and systematic, respectively. The combined values of $\mathrm{M_W}$ from each collaboration take into account the correlated systematic uncertainties between the two channels and between the different years of data taking. The $\mathrm{W^+W^-} \to \mathrm{q_1\overline{q}_2}\ell\nu_\ell$ results from the ALEPH and OPAL collaborations include mass information from the $\mathrm{W^+W^-} \to \ell\nu_\ell\ell'\nu_{\ell'}$ channel.

The W boson mass measured at LEP using a direct reconstruction method yields [44]:

$$\mathrm{M_W(direct\ recons.)} = 80.428 \pm 0.30(\mathrm{stat.}) \pm 0.036(\mathrm{syst.})\ \mathrm{GeV}.$$

When this is combined with the result obtained from the threshold cross section measurement one obtains a W mass measurement of [44]:

$$\mathrm{M_W} = 80.427 \pm 0.046\ \mathrm{GeV}.$$

[4] The kinematic fit is defined employing energy and momentum conservation based on the precise knowledge of the beam energy of and direction as constraints.

[5] Taking into account all the detector effects.

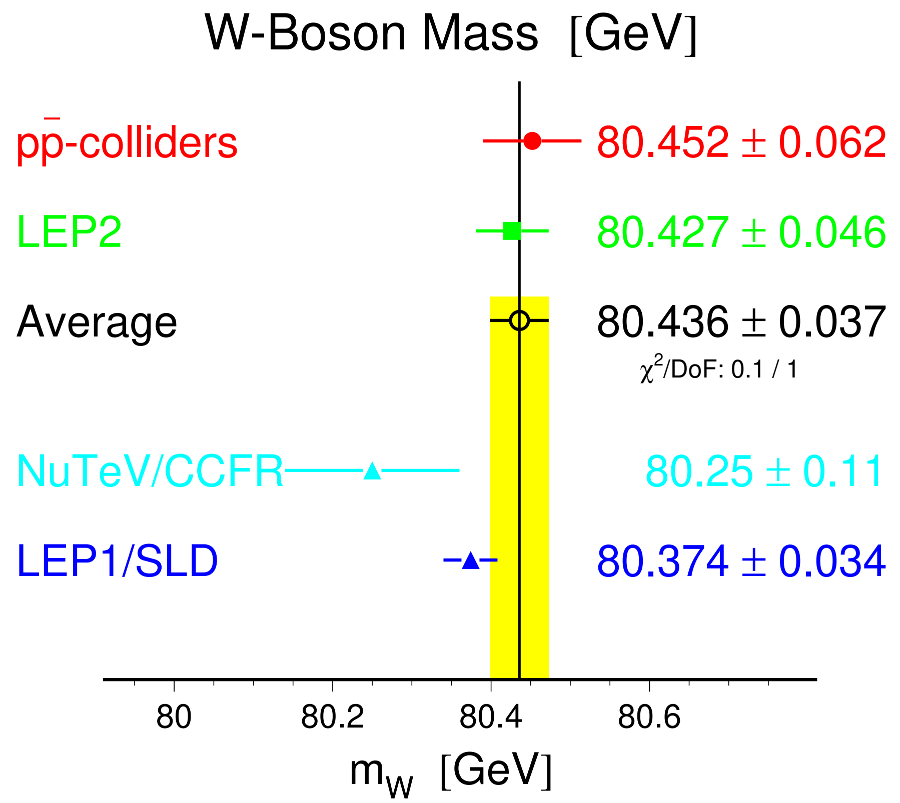

Figure 4.11: W mass values by direct, $p\overline{p}$/ LEP2, and indirect, NuTeV/ LEP1 measurements.

4.5 W^+W^- Decays

W pair events can be classified by the decay products in three different channels: hadronic $W^+W^- \to q_1\overline{q}_2q_3\overline{q}_4$, semileptonic $W^+W^- \to q_1\overline{q}_2\ell\nu_\ell$ and leptonic $W^+W^- \to \ell\nu_\ell\ell'\nu_{\ell'}$. The final state in these channels is characterized by four quarks in the hadronic channel, ($W^+ \to q_1\overline{q}_2$, $W^- \to q_3\overline{q}_4$), by two quarks one charged lepton and the corresponding neutrino in the case of semileptonic decays, ($W^+ \to q_1\overline{q}_2$, $W^- \to \ell\nu_\ell$) and by two charged leptons and the corresponding neutrinos in leptonic decays, ($W^+ \to \ell\nu_\ell$, $W^- \to \ell'\nu_{\ell'}$).

- **Fully hadronic channel**.
  The typical topology of a hadronic event consists of four or more energetic jets in the final state. Figure 4.12 shows an example of $W^+W^- \to q_1\overline{q}_2q_3\overline{q}_4$ candidate recorded at $\sqrt{s}$=192 GeV by OPAL. This channel has a high multiplicity and visible energy and its branching ratio is the biggest of the three possible W pair decays (46%). The main background to this four-jet topology comes from $e^+e^- \to q\overline{q}$ events.

  In the case of a direct reconstruction method to obtain the mass, a jet finder is used to force the selected events to contain four or five jets [63]. These jets are usually reconstructed using both tracks and calorimeter information combined to give the best resolution. $\mathrm{M_W}$ may be reconstructed by forming the invariant mass of pair of jets.

A conceptual difficulty of this channel is the combinatorial background, since the four jets can be combined in three ways to form the two W bosons candidates. A further problem are the final state interaction effects, such as Bose-Einstein correlations or color reconnection [64,65] which can influence the reconstructed event mass and therefore $\mathrm{M_W}$.

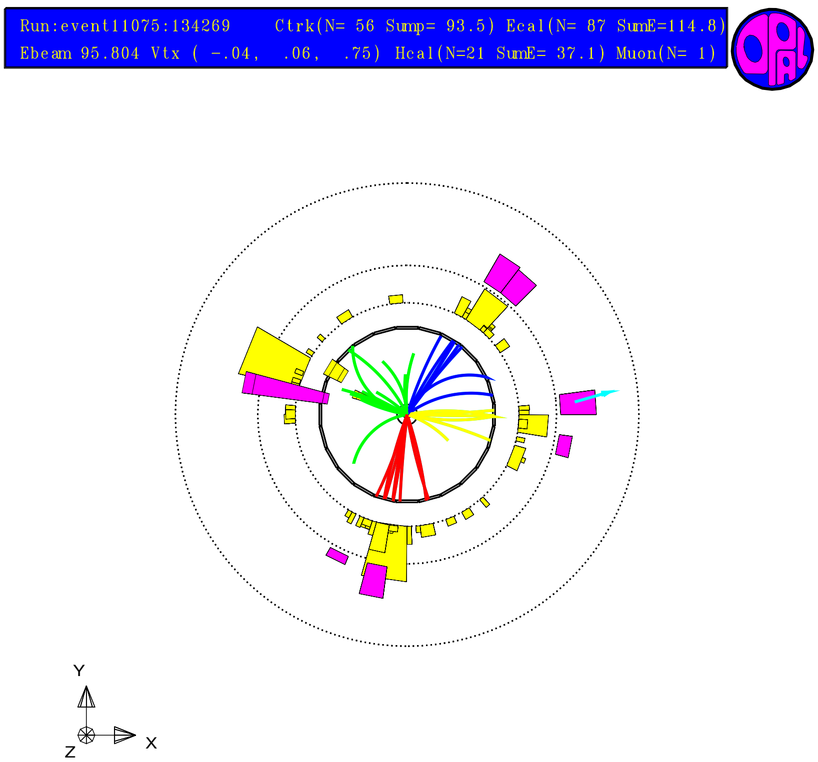

Figure 4.12: $\mathrm{W^+W^-} \rightarrow \mathrm{q_1\overline{q}_2q_3\overline{q}_4}$ candidate recorded by OPAL at $\sqrt{\mathrm{s}}$=192 GeV. The tracks in the center correspond to the four jets reconstructed in the central detector. The blocks after the central detector are the electromagnetic and the hadronic clusters of energy in the calorimeters. The arrow pointing out the hadron calorimeter describes the muon escaping towards the muon detector.

- **Semileptonic channel**
  This channel is characterized by the presence of two or more hadronic jets, an isolated energetic lepton (or a narrow jet in case of hadronic τ decays) and missing energy and momentum due to the undetected neutrino (see figure 4.13 for a $\mathrm{W^+W^-} \rightarrow \mathrm{q_1\overline{q}_2}\ell\nu_\ell$ candidate recorded at $\sqrt{\mathrm{s}}$ = 192 GeV by OPAL). The branching ratio of this channel is 44%.

The background is very low and only in the case of $qq\tau\nu$, $e^+e^- \rightarrow q\overline{q}$ processes contribute to the background [66].

The mass of the W boson can be estimated by forming the invariant mass of the hadronic system, using the full information of the event in a kinematic fit. In this case, the hadronic system is forced into two jets, which are reconstructed as in the fully hadronic channel.

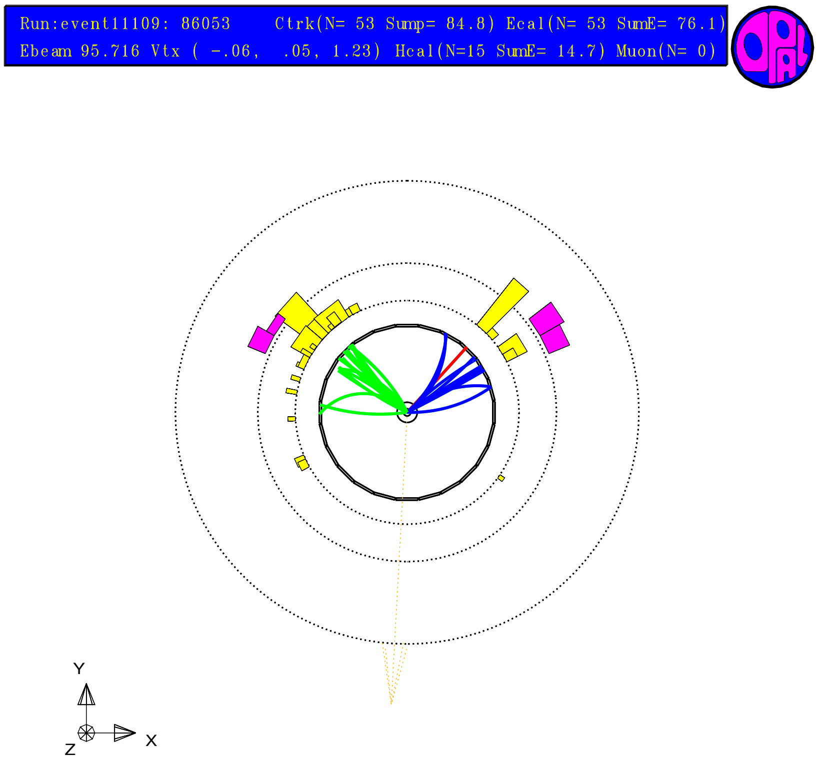

Figure 4.13: $W^+W^- \rightarrow q_1\overline{q}_2\ell\nu_\ell$ candidate recorded by OPAL at $\sqrt{s}$=192 GeV. The two quarks are represented by the two jets in the central detector. The corresponding charged lepton is a e^- which flies towards the electromagnetic calorimeter. The dotted arrow is the missing momentum due to the not observed neutrino.

- **Fully leptonic channel**

Purely leptonic decay modes of a W pair, although small in rate (these decays comprise 10% of the total W^+W^- cross section), give the cleanest signal of the W pair production processes in e^+e^- collisions. This channel is characterized by two acoplanar charged leptons and a large missing energy due to at least two unobserved particles in the final state [9]. Figure 4.14 shows a $W^+W^- \rightarrow \ell\nu_\ell\ell'\nu_{\ell'}$ candidate with two muons in the final state recorded at $\sqrt{s}$=196 GeV by OPAL. Although a full reconstruction of leptonic events is not possible due to the two neutrinos in the final state, the absence of final state interactions and hadronisation uncertainties make this channel particularly attractive. The dominant background sources are Weν, ZZ and dilepton events.

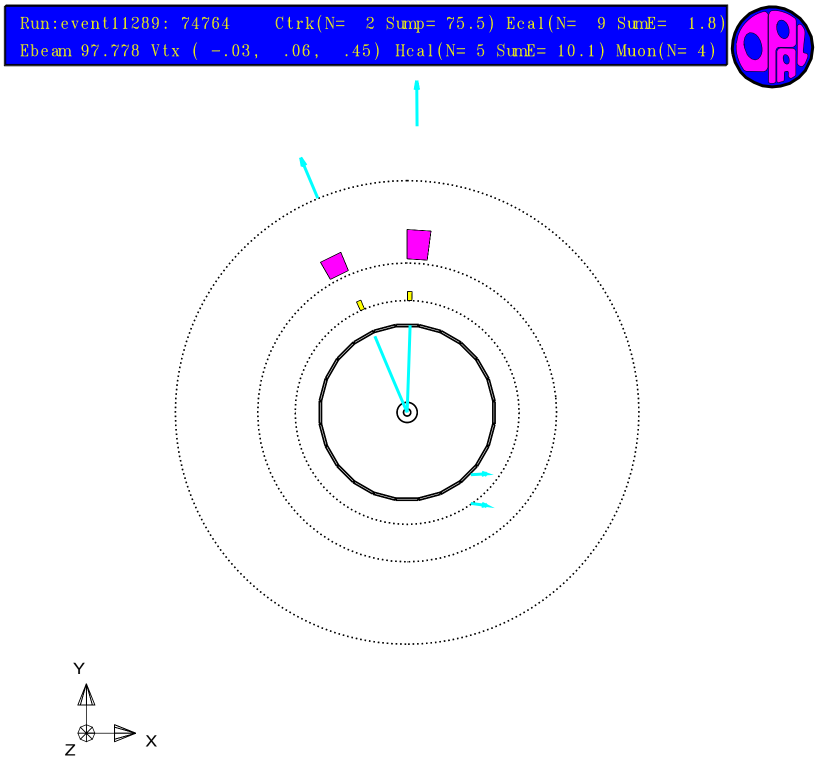

Figure 4.14: $W^+W^- \rightarrow \ell\nu_\ell\ell'\nu_{\ell'}$ candidate recorded by OPAL at $\sqrt{s}$=196 GeV. The two charged leptons are represented by the two tracks in the central detector. The two arrows escaping from the last blocks (which are the hadron calorimeter) correspond to the two muons which fly towards the muon detector.

Chapter 5

The Selection of Fully Leptonic Events

This chapter describes the selection of $\mathrm{W^+W^-} \rightarrow \ell\nu_\ell\ell'\nu_{\ell'}$ events used for the determination of $\mathrm{M_W}$. The Monte Carlo generators used to simulate the signal and background processes are as well described at the end of the chapter.

During the on-line reconstruction, the events pass a first classification based on a set of conditions imposed by the filter system (see chapter 2). The accepted events are recorded and subjected to a refined off-line reconstruction. The present $\mathrm{M_W}$ analysis makes use of the `WW113` software package [67], a set of FORTRAN programs designed to standardize the jet and tracks selection, momenta and energy determination, error parameterization, kinematic fitting and systematic study of $\mathrm{W^+W^-}$ production at OPAL. The `WW113` package consists of independent subroutines which can be used very flexible in each individual study.

The signature of the $\mathrm{W^+W^-} \rightarrow \ell\nu_\ell\ell'\nu_{\ell'}$ channel is an acoplanar lepton pair. Di-lepton decays of W pairs lead to six different classes, ee, $\mu\mu$, $\tau\tau$, eμ, eτ and $\mu\tau$ in ratios 1 : 1 : 1 : 2 : 2 : 2. Experimentally these di-lepton classes lead to three quite different signatures depending on the number of τ's in the final state. Four ninth of the events have two long lived charged leptons (e, μ) in the final state originated directly from W decays, four ninth have one such lepton and in one ninth both W bosons decay into tau leptons. Two thirds of the cross-section corresponds to events in which the leptons are of different flavor [68].

The main background are leptonic decays in $\mathrm{ee} \rightarrow \mathrm{ZZ}$, $\mathrm{ee} \rightarrow \mathrm{Zee}$ and $\mathrm{ee} \rightarrow \mathrm{We}\nu$ events. These sources comprise 30%, 40% and 15% respectively of the total selected background cross-section for the $\mathrm{W^+W^-} \rightarrow \ell\nu_\ell\ell'\nu_{\ell'}$ events [68]. Other background sources such as $\mathrm{ee} \rightarrow \mathrm{ee}$, $\mathrm{ee} \rightarrow \mu\mu$ and $\mathrm{ee} \rightarrow \tau\tau$ and two photon production of di-leptons, contribute as well at a small level.

5.1 The Selection of Fully Leptonic Events

The tracks and electromagnetic clusters of all possible event candidates pass through a first common set of **quality cuts**. The aim of these cuts is to avoid fake signals coming normally from electronic noise in the different parts of the detector. The most important quality cuts can be summarized as follows [69]:
'Good tracks' in central detector:

- A minimum transverse momentum: $p_T > 150$ MeV
- A maximum total momentum to avoid wrong measurements: $p < 0.1 \times 10^{+11}$ GeV
- Minimum number of hits in the jet chamber: $N \geq 20$
- Minimal radial distance from the interaction point: $|d_0| < 2.0$ cm
- Minimal distance from the interaction point in the beam direction: $|z_0| < 25$ cm

'Good cluster' in the electromagnetic calorimeter:

- In the barrel region at least 1 block is required and an energy larger than 100 MeV.
- In the endcap region at least 2 blocks are required and an energy larger than 250 MeV.

Further energy cuts are defined for clusters in the forward detector (FD), in the gamma catcher[1] (GC) and in the silicon–tungsten luminometer (SW) to complete the set of conditions which define the quality cuts [69]: $E_{FD} > 5$ GeV, $E_{GC} > 5$ GeV and $E_{SW} > 2$ GeV.

5.1.1 The Preselection

An event is selected as a $W^+W^- \to \ell\nu_\ell\ell'\nu_{\ell'}$ candidate if it passes a series of cuts defined to isolate the signal events and to reject the dominant backgrounds.
In the first step high multiplicity events are rejected defining the following conditions:

- The charged track multiplicity is between 1 and 8.
- The number of charged tracks plus electromagnetic clusters does not exceed 15.

In the next step jets are reconstructed using a *cone algorithm* [70]. In this algorithm, a jet is defined as a set of particles whose momentum vectors lie within a cone of half–angle R, such that the axis of the cone coincides with the momentum sum of the particles contained. The total energy of the set of particles is required to be greater than some cutoff ϵ. Thus the results of the jet finding depend on two parameters, R and ϵ. The values chosen for these parameters when the cone algorithm is applied to observed tracks and calorimeter clusters are the following:

- A half-opening angle R of 20 degrees is defined.
- A jet energy ϵ, larger than 2.5 GeV is required.

Only those events with 1–3 identified jets are considered further in the general selection. The preselection efficiency for the signal, $W^+W^- \to \ell\nu_\ell\ell'\nu_{\ell'}$ is estimated to be around $98.0 \pm 0.1\%$. The jet multiplicities are expected to be in the ratio 0.059 : 0.905 : 0.036 for mono-jet, di-jet and tri-jet respectively after the preselection [71].

[1] The space between the forward calorimeter and the endcap lead glass causes a gap in the calorimeter acceptance in the polar angle between 142 and 200 mrad. This gap is covered by the gamma catcher.

5.1.2 The Two-Jet Selection

The general selection for di-lepton events requires a pair of leptons and a significant missing energy and momentum due to the non-observed neutrinos in the final state. The principal cuts of this selection are [72]:

- A minimum acolinearity angle,$\phi_{acol} > 5^o$ is required. This angle is defined as $180^{\rm o}$ minus the angle θ between the two charged leptons. Figure 5.1 shows the geometrical definition of the acolinearity angle. Figure 5.2 shows the acolinearity angle cut.

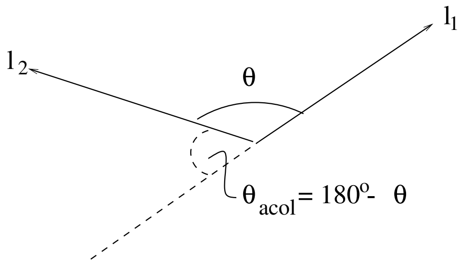

Figure 5.1: Geometrical definition of the acolinearity angle.

- A minimum scaled transverse momentum, x_T: $x_T = p_T/E_{beam} > 5\%$, is required where p_T is the momentum component perpendicular to the beam axis and E_{beam} is the beam energy. Figure 5.3 shows the x_T cut.

- A number of Standard Model processes can lead to high energy particles which travel along the beam pipe and are not detected. They give rise to missing momentum along the beam axis. The selected candidate should therefore have a significant missing momentum in the plane perpendicular to the beam axis, p_T^{miss} and a total missing momentum vector which does not point along the beam pipe to avoid such background events. A conventional cut on the direction of the missing momentum is made: $|\cos\theta_{p_T}^{miss}| < 0.95$.

- Other Standard Model events containing neutrinos, specially those which come from $\mathrm{e^+e^-} \to \tau\tau$ events, or poorly measured particles represent a potential background. In these events the value of p_T^{miss} can be large and the missing momentum vector may have a big angle with respect to the beam axis. However, most of the Standard Model events tend to be approximately *back-to-back* in the plane perpendicular to the beam axis (coplanar). In these coplanar events, the component of p_T^{miss} which is perpendicular to the event thrust axis[2] in the transverse plane, a_T^{miss}, is much less sensitive than p_T^{miss} to the presence of neutrinos which come from tau decays or poorly measured particles. A cut on a_T^{miss} is a

[2]The thrust axis **n** is defined as the direction which maximizes

$$\frac{\sum_i \vec{p}_i \cdot \vec{n}}{\sum_i |\vec{p}_i|}$$

where i runs over all momenta of charged tracks and clusters.

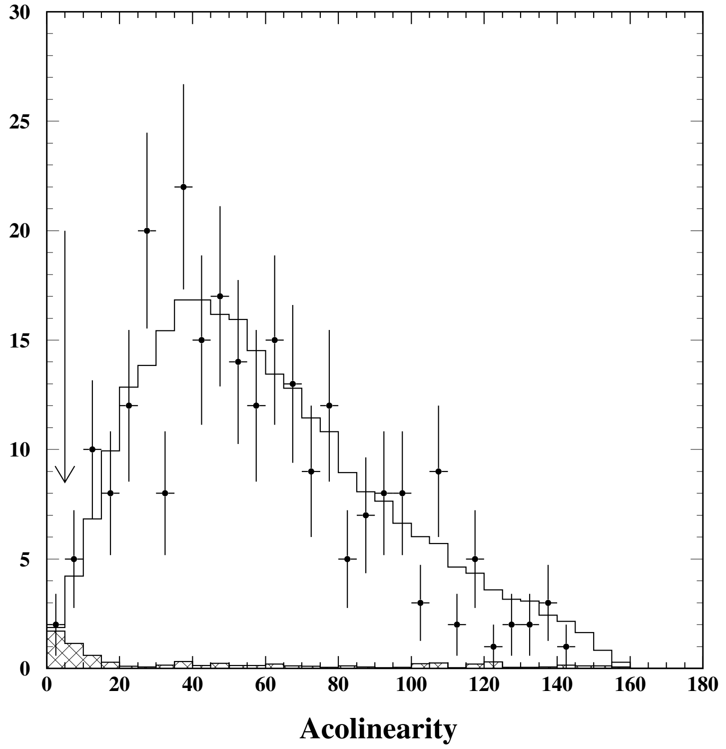

Figure 5.2: Acolinearity cut for di-lepton events at a center-of-mass energy of 189 GeV. All other cuts which define the selection are already applied. Events to the right hand side of the arrow are accepted. The hatched region corresponds to the background events.

more effective way to remove this background than a cut on the acoplanarity angle. Figure 5.4 shows the geometrical definition of a_T^{miss}. The cut is: $a_T^{miss}/E_{beam} > 0.022$ [73]. Figure 5.5 shows the a_T^{miss}/E_{beam} cut distribution for a center-of-mass energy of 189 GeV.

In addition to the cuts described above further requirements are imposed as background vetoes:

- A potential background arises from lepton pairs of two-photon processes in which one of the initial electrons is scattered under large angle to the beam direction. Cuts in the forward region (SW, FD and GC) suppress such events:
  - Events with a total energy in the FD and the SW in either z-hemisphere exceeding 80% of the beam energy are rejected.
  - GC clusters with energy exceeding 5 GeV are rejected.

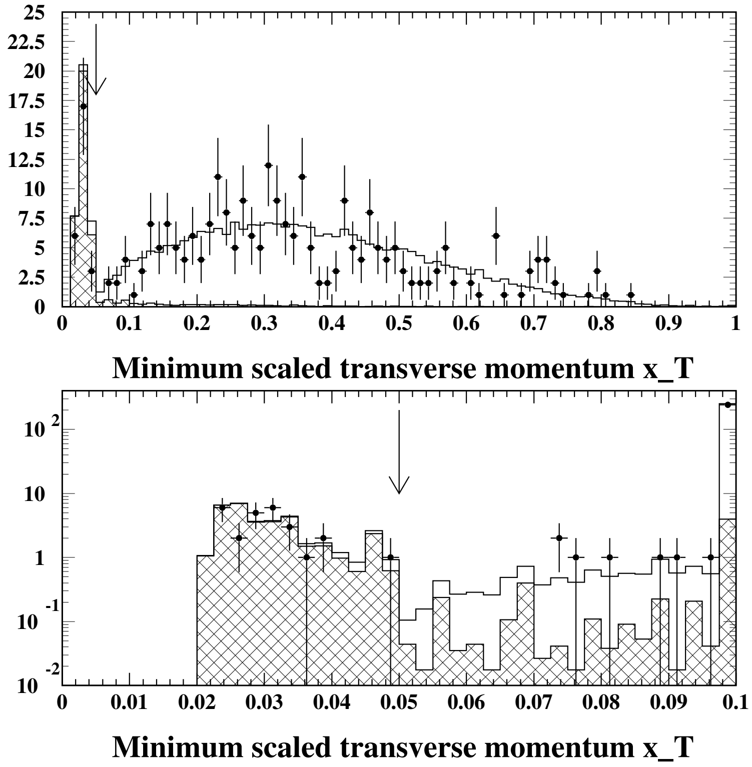

Figure 5.3: x_T cut for di-lepton events at a center-of-mass energy of 189 GeV. All other cuts which define the selection are already applied. Events to the right hand side of the arrow are accepted. The hatched region corresponds to the background events.

- An additional cut is introduced using the MIP plug detector. This detector consists of four layers of scintillating tiles installed at each end of the OPAL detector. The aim of the MIP plug is to provide a hermetic coverage for muons for $\theta > 25$ mrad. If the angular region is not covered, muons can escape detection and this can lead to a background from $\mathrm{e}^+\mathrm{e}^-\mu^+\mu^-$ events in which one electron and one muon were observed in the detector. Using the MIP plug detector, candidate events are vetoed if they contain coincident hits in two or more scintillator layers in the MIP plug at the same ϕ and at the same end of OPAL. The efficiency to detect a muon with these cuts is measured to be $80 \pm 4\%$.

The analysis presented in this thesis makes used of leptonic events with exactly two identified leptons only. A total of 761 events at the center-of-mass considered in the analysis, from 183 to 202 GeV, are observed in the data. Table 5.1 summarizes the observed number of events for each center-of-mass energy together with the corresponding luminosities. Figure 5.6 shows distributions of the reconstructed visible energy fraction for the six different di-lepton event

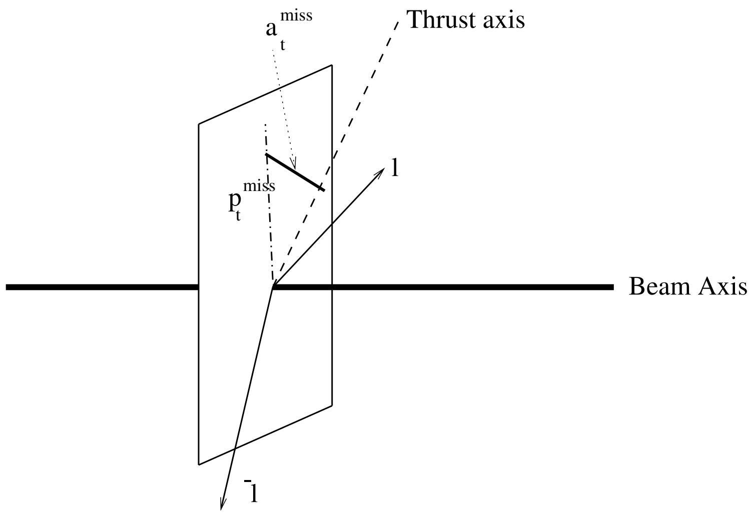

Figure 5.4: Geometrical definition of the a_t^{miss} variable.

classes.

ECM (GeV)	$\mathcal{L}(\mathrm{pb}^{-1})$	$\mathrm{W}^+\mathrm{W}^- \to \ell\nu_\ell\ell'\nu_{\ell'}$
183	57	71
189	183	278
192	29	52
196	77	144
200	74	134
202	37	82

Table 5.1: Integrated luminosities and number of $\mathrm{W}^+\mathrm{W}^- \to \ell\nu_\ell\ell'\nu_{\ell'}$ events for the data from 183 to 202 GeV.

5.2 The Di-Lepton Classification

The lepton classification is based on the lepton identification described in the following subsection as well as the observed track multiplicity in each jet. It is further refined by momentum cuts dependent upon the acolinearity angle. The main purpose of this refinement is to re-classify identified e and μ with low momenta which are more likely to originate from τ decays as τ candidates [74].

5.2.1 The Lepton Identification

The lepton flavor identification is performed by different routines implemented in the `WW113` package.

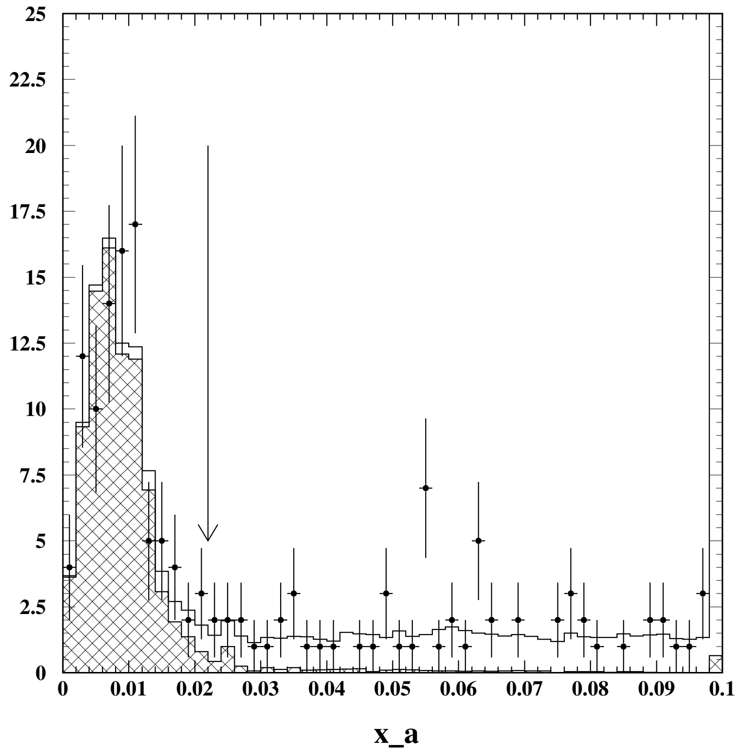

Figure 5.5: a_t^{miss} cut for di-lepton events at a center-of-mass energy of 189 GeV. All other cuts which define the selection are already applied. Events to the right hand side of the arrow are accepted. The hatched region corresponds to the background events.

The *electron identification*, employs the ratio of the energy deposit in the electromagnetic calorimeter to the track momentum, E/p. This identification tries to use the smallest possible number of subdetectors (only the jet chamber and barrel and endcap electromagnetic calorimeter are used) in order to have a high efficiency. An important background source for the electron identification are tracks from γ-conversion into an $\mathrm{e^+e^-}$ pair. If one of the tracks has low momentum such that the other one passes the isolation cut or if the tracks are close enough to be reconstructed as a single one, the track can pass as an isolated electron [75]. A standard OPAL finding routine `IDGCON` [3] [76] is used to remove such tracks. This package uses the dE/dx measurements to remove background. Converted γ's in which the tracks are too closed to be distinguished tend to give dE/dx measurements higher than those expected for electrons. The dE/dx value of the electron candidate is required to be within three standard deviations of the expected value for an electron.

The *muon identification* requires a minimum number of associated hits in either the muon

[3] This routine checks if a track is compatible with an electron or a positron originating from a gamma conversion.

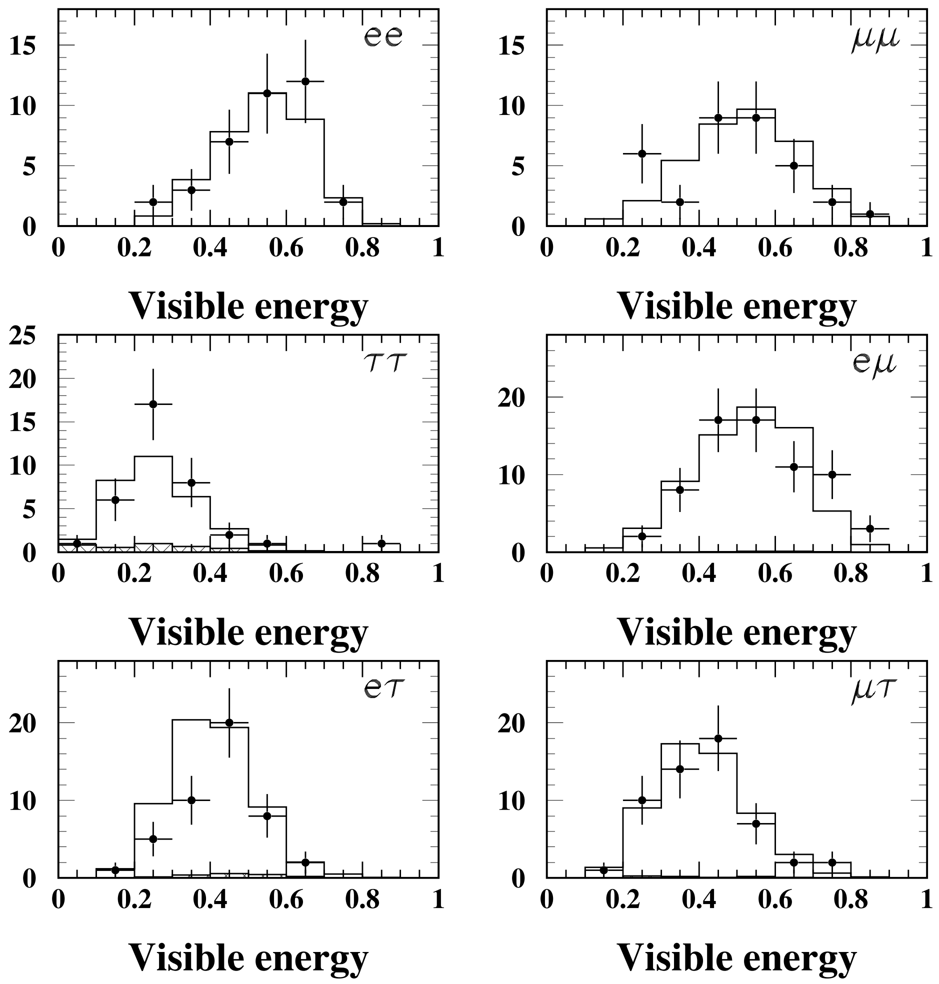

Figure 5.6: Distributions of visible energy scaled to the center-of-mass energy, $\mathrm{R_{vis}}$, for the six di-lepton classes selected as $\mathrm{W^+W^-} \rightarrow \ell\nu_\ell\ell'\nu_{\ell'}$ events. The data are shown as the points and the error bars denote the statistical errors. The total Monte Carlo expectation is shown as the histogram with the non-$\ell^+\ell^-\nu\nu'$ background contribution shown by the hatched histogram.

chamber or the hadron calorimeter. Furthermore, the energy deposit in the electromagnetic calorimeter must be small. Thus if a muon track has an associated electromagnetic cluster, its energy must be less than 3 GeV in the barrel and end caps regions of the detector or less than 5 GeV in the overlap region $0.7 < |\cos\theta| < 0.82$.

5.2.2 The Momentum Variation with Acolinearity

The energy and momentum of a lepton which comes from a W decay can be determined from energy and momentum conservation in the W rest frame.

The momentum depends on the decay angle θ^* of the lepton with respect to the W direction in the W restframe (see figure 5.7):

$$E_\ell = \frac{E_W}{2}(1 + \beta \cos\theta^*) \qquad \text{with} \quad \beta = \frac{P_W}{E_W} \tag{5.1}$$

P_W is the momentum of the W boson and E_W is its energy.

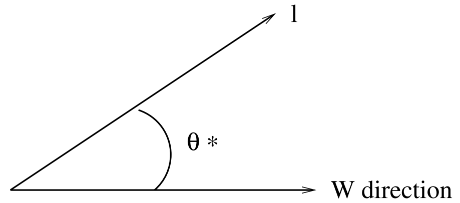

Figure 5.7: Leptonic decay of a W boson. θ^* is the angle between the initial W direction and the lepton in the W rest frame.

If the lepton is produced in the same direction than its parent W, it will have the maximal energy and if it is emitted in the opposite direction to the initial W boson it will have the minimal energy.

In an event, the two W bosons produced from an e^+e^- collision are emitted *back-to-back*[4]. If the leptonic decays from both W bosons take place in the same direction than its parents, the θ^* angle will be almost zero and they will tend to have high momenta (see figure 5.1). In this case the two charged leptons will be emitted almost back–to–back and the event has *low acolinearity*. In the case that both leptons are emitted in almost the same direction, the event has a *high acolinearity*.

The scaled momenta for the higher momentum lepton X_1[5] and the lower momentum lepton X_2 are studied with Monte Carlo events. Figures 5.8 and 5.9 shows these distributions at low and high acolinearity for the different lepton event classes identified from Monte Carlo tree level information.

In both cases, at low and at high acolinearity, differences are observed between $\ell\ell$[6] and $\ell\tau$ events. In $\ell\tau$ events, the visible particles coming from a τ will have less energy than the electron or muon which are originated directly from the W boson due to the extra neutrino in the τ decay.

A comparison between low and high acolinearity plots shows a larger number of events along the X_2 axis in the case of high acolinearity. This is in agreement with the hypothesis that one particle is emitted forwards with respect to its parents W and the other particle is emitted backwards.

[4] Neglecting effects of initial state radiation.
[5] $X_i = p_i/E_{beam}$ where p_i denotes the momentum of the lepton i.
[6] Here ℓ means e^- or μ.

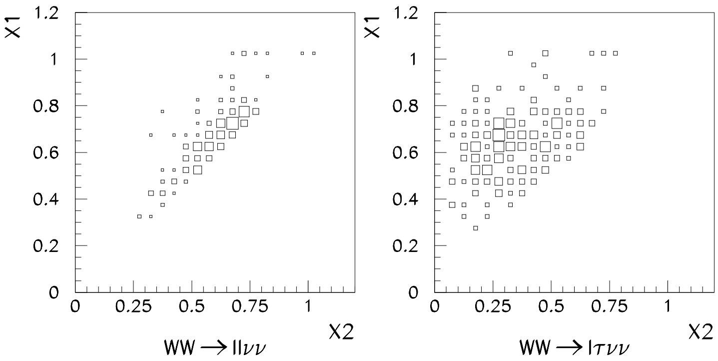

Figure 5.8: Di-jet events measured at 189 GeV with low acolinearity ($0^{o} < \mathrm{acolinearity} < 15^{o}$). The measured momentum distributions are scaled by the beam energy. The left hand plot contains $\ell\ell$ events (ℓ is an electron or a muon) and the right hand one contains $\ell\tau$ events. The lepton class identification is determined in both cases from Monte Carlo tree level information.

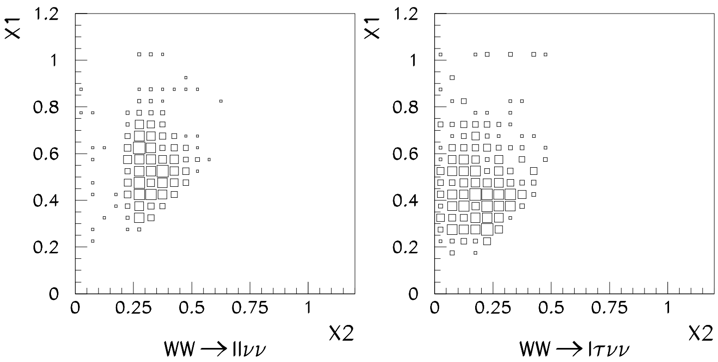

Figure 5.9: Di-jet events measured at 189 GeV with high acolinearity ($105^{o} < \mathrm{acolinearity} < 180^{o}$). The measured momentum distributions are scaled by the beam energy. The left hand plot contains $\ell\ell$ (ℓ is an electron or a muon) events and the right hand one contains $\ell\tau$ events. The lepton class identification is determined in both cases from Monte Carlo tree level information.

These observed differences at low and high acolinearity for the $\ell\ell$ and $\ell\tau$ events motivate the development of acoplanar dependent cuts on these variables, X_1 and X_2 to optimize the efficiency matrix. In this matrix, each element represents the fraction number of events selected and classified in a particular channel divided by the total number of Monte Carlo tree level events for that channel. The sum of each column gives the total efficiency ϵ for each class taking into account all the other di-lepton events. The classification purity $\mathcal{P}$, is defined as:

$$\mathcal{P}_i = \frac{\omega_i \epsilon_{ii}}{\sum_j \omega_j \epsilon_{ij}} \tag{5.2}$$

where ω is a weight factor whose value is 2 in case of $e\mu$, $e\tau$ and $\mu\tau$ events since there are two possibilities to obtain each combination and 1 in case of ee, $\tau\tau$ and $\mu\mu$ events and ϵ_{ij} are the different matrix elements.

The relative performance of a group of cuts can be determined by the calculation of a factor 'D' which is defined as the sum of the diagonal elements of the efficiency matrix divided by the total sum of all elements:

$$D = \frac{Tr(\epsilon_{ij})}{\sum_{i,j} \epsilon_{ij}} \tag{5.3}$$

If each selected event was correctly classified, 'D' would be 100%. Before the acolinearity cuts definition this parameter had a value of 77.1 $\pm$ 0.4%. After the inclusion of these cuts, its value is improved to 83.2 $\pm$ 0.3%. A complete description of the method and the numerical cuts used in the analysis can be found in [74].

The efficiency matrix for all 2 jets events after these new acolinearity dependent momentum cuts have been applied is shown in table 5.2. Figure 5.10 shows the selected di-lepton types after the descripted selection.

MC	Truth	ee	$e\mu$	$e\tau$	$\mu\mu$	$\mu\tau$	$\tau\tau$	Purity
S								
E	ee	72.4	0.3	6.6	0.0	0.0	1.0	83.0
L	$e\mu$	1.3	71.1	5.4	0.6	7.2	1.6	83.2
E	$e\tau$	7.1	3.5	58.3	0.0	1.1	10.7	81.2
C	$\mu\mu$	0.0	0.7	0.0	70.7	4.5	0.2	87.0
T	$\mu\tau$	0.0	2.7	0.3	5.2	56.0	6.9	86.1
E	$\tau\tau$	0.4	0.3	3.5	0.2	3.2	41.8	74.1
D								

Table 5.2: Efficiency Matrix for two jets events at a center-of-mass energy of 189 GeV after acolinearity dependent momentum cuts have been applied.

5.3 Background Sources for $\mathrm{W^+W^-} \to \ell\nu_\ell\ell'\nu_{\ell'}$ Events

Backgrounds to the $\mathrm{W^+W^-} \to \ell\nu_\ell\ell'\nu_{\ell'}$ event selection can be grouped into three different classes [69].

- The first class consists of background processes which do not contain two leptons and two neutrinos in the final state. The τ-pair, two-photon and Zee events belong predominantly to this type of background. This class contributes an expected 38 ± 11 fb to the

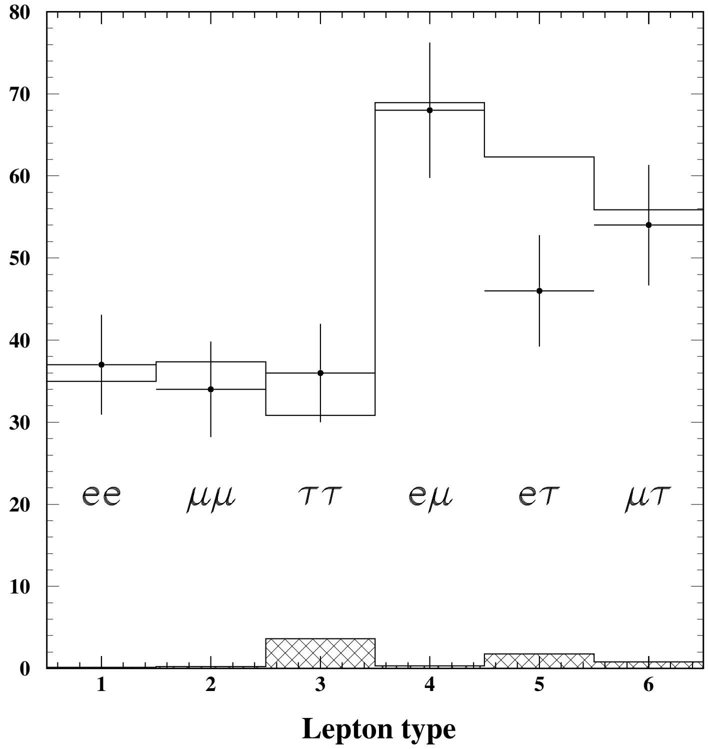

Figure 5.10: Selected di-lepton type after the selection described in section 5.2.2. The hatched region corresponds to background events.

total selected $W^+W^- \rightarrow \ell\nu_\ell\ell'\nu_{\ell'}$ cross section. Figures 4.5(b) and 4.5(d) show the corresponding Feynman diagrams for these events.

- The second class consists of an irreducible background from $\ell^+\ell^-\nu_{\ell'}\overline{\nu}_{\ell'}$ final states which can only be produced by neutral current diagrams as the neutrinos have a different lepton flavor than the charged leptons. Leptonic decays from ZZ and $Z\gamma$ processes contribute to this class. Figure 4.5(a) shows the Feynman diagram for this background source. Since the neutrinos are unobserved, these final states are indistinguishable from the signal events in terms of the event topology. This class contributes an additional 45 ± 2 fb of background to the inclusive $W^+W^- \rightarrow \ell\nu_\ell\ell'\nu_{\ell'}$ selection.

- The final class of background is the difference between the complete four-fermion cross section and the theoretically predicted rate from CC03 diagrams for $W^+W^- \rightarrow \ell\nu_\ell\ell'\nu_{\ell'}$ final states. This includes neutral-current processes in the final states where the two charged leptons are of the same type ($\ell^+\nu\ell^-\nu$). Only ee, $\mu\mu$ and $\tau\tau$ events have contributions from such diagrams. Four-fermion processes with an e^- in the final state ($\mathrm{e}\nu\ell\nu$) contribute as well to this class of background. Leptonic decays from $\mathrm{We}\nu$ events belong to this background. Figure 4.5(c) shows the corresponding Feynman diagram. This non CC03 production and the interference between the CC03 and the non CC03 diagrams contributes a large cross section of 77 $\pm$ 10 fb which is treated as a background in the CC03 selection and is also largely irreducible within the detector acceptance.

The errors on the accepted background cross sections include all systematic uncertainties and the effects of limited Monte Carlo statistics. A summary of the accepted background cross-sections is given in Table 5.3. The dominant systematic error associated with the leptonic background estimate is due to the four-fermion correction. The accepted four-fermion background rate is estimated from the difference observed in KORALW four-fermion and CC03 samples with equivalent EXCALIBUR samples providing a cross-check.

Source	Cross-section (fb)
$\ell^+\nu_\ell\ell^{'-}\nu'_{\ell'}$	77 ± 10
$\mathrm{q\overline{q}}\ell^\pm\nu_\ell$	3 ± 1
$\mathrm{q\overline{q}q\overline{q}}$	—
$\ell^+\ell^-\nu_{\ell'}\overline{\nu}_{\ell'}$	45 ± 2
$\mathrm{q\overline{q}}\nu\overline{\nu}$	3 ± 1
$\mathrm{q\overline{q}e^+e^-}$	1 ± 1
$\mathrm{q\overline{q}}\ell^+\ell^-$	—
$\mathrm{e^+e^-f\overline{f}}$	9 ± 9
$\nu\overline{\nu}\gamma(\gamma)$	2 ± 1
$\ell^+\ell^-$	20 ± 4
$\mathrm{q\overline{q}}$	—
Combined	160 ± 14

Table 5.3: Accepted background cross sections for the 189 GeV $\mathrm{W^+W^-} \to \ell\nu_\ell\ell'\nu_{\ell'}$ selection in fb. All errors include both statistical and systematic uncertainties.

5.4 The General Monte Carlo Generators Description

The different Monte Carlo generators used in the present analysis for the simulation of $\mathrm{W^+W^-}$ signal and the corresponding background events are now briefly described [77, 78]:

- **Signal Generator:**
  - KORALW [79]
    This is the standard generator to perform $\mathrm{W^+W^-}$ studies in OPAL. This program includes the leptonic decays of W bosons and secondary decays, i.e in the tau lepton decays. Effects of initial and final state radiations are implemented too. Hadronization of quarks is performed using the program JETSET [80]. KORALW includes an interface to the GRACE [81] library to calculate multi-diagram matrix elements.

- **Background Generators:**
  - BHWIDE [82]

    The program evaluates the Bhabha cross sections at LEP1 and LEP2 energies. It is used in this analysis to generate Bhabha final states for background processes.
  - KORALZ [83]

    This program simulates the process of fermion pair production, where the fermion can be a lepton or a quark. KORALZ is used to generate $\mu\mu$ and $\tau\tau$ di-leptons background processes.
  - PYTHIA [80]

    This generator is the standard package to produce ZZ and Zee processes for background events. For applications at LEP2, the JETSET [80] package is implemented together with PYTHIA, providing together a wealth of different hadronic and also non-hadronic processes.
  - RADCOR [84]

    This generator is used in the analysis to simulate four-fermion processes for $\mathrm{e^+e^-} \rightarrow \gamma\gamma$ events.
  - VERMASEREN [85]

    This program performs calculations of $\mathrm{e^+e^-} \rightarrow \mathrm{e^+e^-} f\overline{f}$ events via $\gamma\gamma$ collisions. In this analysis it is used for the two-photon background.

- **Generators for further Systematic Checks:**
  - EXCALIBUR [86]

    The program EXCALIBUR evaluates cross sections for $\mathrm{e^+e^-}$ scattering into all possible four-fermion final states. EXCALIBUR has the restriction that the fermions are massless. The OPAL analysis employs an additional interface with JETSET to include the mass of the fermions. EXCALIBUR is used in the analysis to check Monte Carlo systematic uncertainties due to the differences between samples which include all possible four-fermion final states and those which include CC03 diagrams only.
  - GRC4F [87]

    This program is based on GRACE and allows the full set of four-fermions in the final state, including the interferences between them, to be used. Final state interaction effects also are implemented. In the present analysis, it is used together with EXCALIBUR to perform Monte Carlo systematic uncertainties checks.

5.5 The Cross Section for $\mathrm{W^+W^-} \rightarrow \ell\nu_\ell\ell'\nu_{\ell'}$ Events

The fully leptonic event selection has a very small background and is therefore well suited to measure the four-fermion cross sections for the six charged di-lepton final states. These states have contributions from WW, ZZ, $\mathrm{We}\nu_\mathrm{e}$, $\mathrm{Ze^+e^-}$ and $\mathrm{Z}\nu\overline{\nu}$ diagrams and their respective interferences.

The four-fermion cross sections are defined taking into account the following kinematic acceptance cuts [72]:

- At least one of the charged leptons is produced with $|\cos\theta| < 0.90$.
- Both charged leptons are produced with $|\cos\theta| < 0.99$.
- The invariant mass of the system must be greater than 10 GeV and the transverse momentum must have $\mathrm{p_T/E_{beam}} > 5\%$.

The corresponding values for the six individual cross section are shown in table 5.4. The results obtained are in good agreement with the Standard Model rates.

$e^+e^- \rightarrow$	Measured cross section (fb)	Expected value (fb)
$e^+e^-\nu\overline{\nu}$	$290\binom{+56}{-51} \pm 11$	262
$\mu^+\mu^-\nu\overline{\nu}$	$195\binom{+44}{-40} \pm 08$	221
$\tau^+\tau^-\nu\overline{\nu}$	$290\binom{+73}{-66} \pm 13$	207
$e^{\pm}\mu^{\pm}\nu\overline{\nu}$	$384\binom{+60}{-55} \pm 11$	387
$e^{\pm}\tau^{\pm}\nu\overline{\nu}$	$225\binom{+64}{-58} \pm 10$	388
$\mu^{\pm}\tau^{\pm}\nu\overline{\nu}$	$348\binom{+69}{-63} \pm 11$	376

Table 5.4: Four fermion $\ell^+\ell^-\nu\overline{\nu}$ individual cross sections at 189 GeV. The errors are the statistical and the systematic uncertainties respectively. The expected cross section values within the Standard Model are calculated using the KORALW four fermion Monte Carlo generator.

The selection efficiency is estimated to be $(84.6 \pm 0.3)\%$, where the error is the statistic uncertainty. This efficiency is obtained for a center-of-mass energy of 189 GeV and takes into account all leptonic W^+W^- decays. Efficiencies for each individual di-lepton pair are shown in table 5.5 [69]. Since the efficiencies shown in this table correspond to those obtained after the whole selection, the values differ from those shown in table 5.2 which shows efficiencies after acolinearity momentum cuts have been applied. Similar values are obtained at the other center-of-mass energies of 183, 192, 196, 200 and 202 GeV.

	$e^+\nu_e e^-\overline{\nu}_e$	$\mu^+\nu_\mu\mu^-\overline{\nu}_\mu$	$\tau^+\nu_\tau\tau^-\overline{\nu}_\tau$	$e^{\pm}\nu_e\mu^{\pm}\nu_\mu$	$e^{\pm}\nu_e\tau^{\pm}\nu_\tau$	$\mu^{\pm}\nu_\mu\tau^{\pm}\nu_\tau$
$e^+\nu_e e^-\overline{\nu}_e$	75.5	0.0	1.0	0.1	6.2	0.0
$\mu^+\nu_\mu\mu^-\overline{\nu}_\mu$	0.0	80.4	0.6	1.2	0.1	6.1
$\tau^+\nu_\tau\tau^-\overline{\nu}_\tau$	0.5	0.4	46.4	0.4	4.1	5.0
$e^{\pm}\nu_e\mu^{\pm}\nu_\mu$	2.5	0.4	1.2	77.8	6.2	7.2
$e^{\pm}\nu_e\tau^{\pm}\nu_\tau$	8.5	0.0	11.1	3.9	63.0	1.1
$\mu^{\pm}\nu_\mu\tau^{\pm}\nu_\tau$	0.1	6.6	8.3	3.9	0.8	60.6

Table 5.5: Individual efficiencies for the selection of each di-lepton event class measured at a center-of-mass energy of 189 GeV. These efficiencies are evaluated with KORALW CC03 Monte Carlo samples.

Chapter 6

Variables sensitive to $\mathrm{M_W}$ for Fully Leptonic Events

As explained in section 4.5, there are not enough constrains to reconstruct fully leptonic events with a kinematic fit, thus the determination of $\mathrm{M_W}$ from leptonic decays must employ alternative methods.

6.1 The Leptonic Energy

The end-points of the leptonic energy spectra in $\mathrm{W^+W^-} \to \ell\nu_\ell\ell'\nu_{\ell'}$ events depend on the W mass. Neglecting the mass of the charged leptons and the finite width of the W boson, the energy of the charged leptons, E_ℓ, can be written in terms of $\mathrm{M_W}$ as [88]:

$$E_\ell = \frac{\sqrt{\mathrm{s}}}{4} + \cos\theta_\ell^*\sqrt{\frac{\mathrm{s}}{16} - \frac{M_W^2}{4}} \tag{6.1}$$

where s is the square of the center-of-mass energy and θ_ℓ^* is the angle between the lepton direction measured in the W rest frame and the direction of the W in the laboratory frame. The latter is not known, so the measured energy is integrated over $\cos\theta_\ell^*$, resulting in a distribution which end points depending on the W mass.

In practice, however, the end-points of the distribution are considerably smeared by finite width effects, by Initial State Radiation and by the detector resolution. These effects weaken the sensitivity of this variable.

Figure 6.1 shows this dependence of E_ℓ on $\mathrm{M_W}$ without taking into account additional detector effects. When $\mathrm{M_W}$ increases, the E_ℓ distribution becomes narrower, whereas if $\mathrm{M_W}$ decreases, the lepton energy distribution becomes broader. The present analysis makes use of the information from the energy of both charged leptons in an event.

6.2 The Pseudomass

In order to include the information from the angle between the two leptons and the correlation between their energies a second kinematic variable, the so–called pseudomass, is used in the

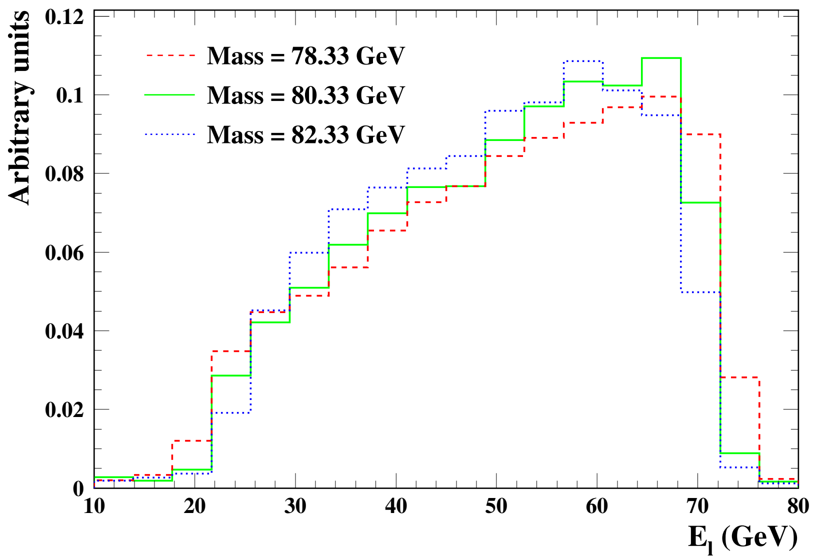

Figure 6.1: Leptonic energy in $W^+W^- \to \ell\nu_\ell\ell'\nu_{\ell'}$ events produced at 189 GeV for M_W = 80.33 GeV (solid line), M_W = 78.33 GeV (dashed line) and M_W = 82.33 GeV (dotted line). The spectra are generated with Monte Carlo without additional detector effects.

analysis. The calculation of this variable is based on an approximative reconstruction of the event. The total reconstruction of the event consists of the determination of the four–momenta for both charged leptons and the two neutrinos, 16 quantities in total. The four-momenta of the two charged leptons are measured. The total reconstruction therefore depends on the determination of the two momenta of the neutrinos [89]. Assuming massless neutrinos and using the standard constraints of a kinematic fit, the four–momentum conservation and assuming that both W bosons have equal mass, seven more quantities can be obtained. A general description of the method can be found in Appendix A. In order to get the missing constraint, an additional arbitrary constraint is defined. If one assumes that both neutrinos are in the same plane as the charged leptons (this corresponds to setting the coefficient c shown in Appendix A to zero), it is possible to reconstruct the event and to calculate the W mass as a function of the momenta of the charged leptons, their masses and the beam energy. Since this assumption is in general not true, this reconstructed mass is called the *pseudomass*. Due to a twofold ambiguity, two solutions are found for this variable:

$$\mathrm{M}^2_{\pm} = \frac{2}{(\overline{\ell}+\ell)^2}\left((\mathrm{P}\overline{\ell}-\mathrm{N}\ell)(\overline{\ell}+\ell) \pm \sqrt{(\ell\times\overline{\ell})^2[(\overline{\ell}+\ell)^2(\mathrm{E_{beam}}-\mathrm{E}_\ell)^2-(\mathrm{P}+\mathrm{N})^2]}\right) \quad (6.2)$$

where

$$\mathrm{P} = \mathrm{E_{beam}}\mathrm{E}_\ell - \mathrm{E}^2_\ell + \frac{1}{2}\mathrm{m}^2_\ell, \qquad \mathrm{N} = -\mathrm{E_{beam}}\mathrm{E}_{\overline{\ell}} - \overline{\ell}\cdot\ell + \frac{1}{2}\mathrm{m}^2_{\overline{\ell}}$$

$\mathrm{E_{beam}}$ is the beam energy, E_ℓ, $\mathrm{E}_{\overline{\ell}}$ are the energies of the two charged leptons, m_ℓ, $\mathrm{m}_{\overline{\ell}}$ are their masses and ℓ, $\overline{\ell}$ are their three–momenta. In the present analysis the charged leptons are considered to be massless particles because the values of these masses are very small in comparison with the beam energy.

The sensitivity of both solutions was studied with Monte Carlo, which showed that only the larger solution, M_+, is sensitive to M_W. The dependence of the pseudomass on M_W for this solution is illustrated in Figure 6.2. Since the condition to define the last constraint which solves the system is arbitrary, a small constant angle, between the plane of the neutrinos and the plane of the charged leptons could also be used. The sensitivity of the measurement is independent of the chosen angle.

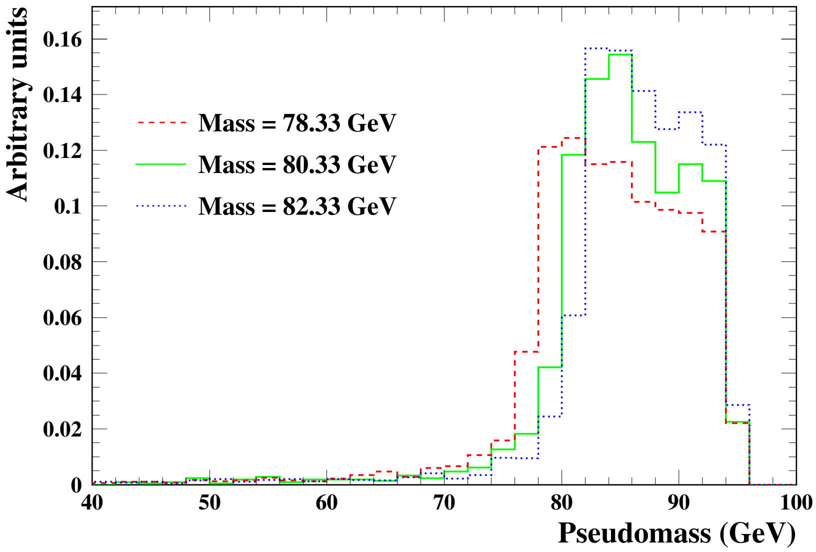

Figure 6.2: The pseudomass in $W^+W^- \to \ell\nu_\ell\ell'\nu_{\ell'}$ events produced at 189 GeV for M_W = 80.33 GeV (solid line), M_W = 78.33 GeV (dashed line) and M_W = 82.33 GeV (dotted line). No additional detector effects are taken into account.

6.3 Classification of Events

In the present analysis, identified taus are rejected since they dilute the sensitivity in the leptonic energy and the pseudomass.

The resolutions obtained for electrons and muons differ significantly at high energies. For 45 GeV electrons, the electromagnetic calorimeter energy has a resolution of approximately 3%, whereas for μ at the same energy, the charged track momentum measured using the central tracker delivers a resolution of approximately 8% [14]. To maximize the sensitivity of the measurement, electron and muon measurements are considered separately in the M_W analysis defining different classes of events for both the pseudomass and the leptonic energy analyses.

In the case of the leptonic energy the information of both charged leptons is used independently. For this variable two different classes are defined; the first class contains leptons identified as electrons and the second class contains leptons identified as muons. To increase the number of leptons used in the analysis also events identified as electron–tau and muon–tau are included. In these events, only the most energetic lepton (if it is identified as an electron or a muon) is used, because the less energetic one is most likely to have originated from the tau decays.

ECM (GeV)	Leptonic Energy	Pseudomass
183	67	32
189	250	140
192	44	21
196	125	65
200	120	59
202	77	33

Table 6.1: Number of observed events for the leptonic energy and the pseudomass, for center-of-mass energies from 183 to 202 GeV.

Figure 6.3 shows E_ℓ for Monte Carlo events generated at M_W = 80.33 GeV. This figure shows both classes for the leptonic energy at $\sqrt{s}$ = 189 GeV between 10 and 80 GeV, the region considered in the fit at this energy. The worse resolution of the muon momenta compared to the electron energy is visible. As shown in figure 6.1, the region sensitive to M_W is around the maximal and the minimal values for E_ℓ. These regions have sharper edges for electron energies (see figure 6.3(a)), than for muon momenta (see figure 6.3(b)).

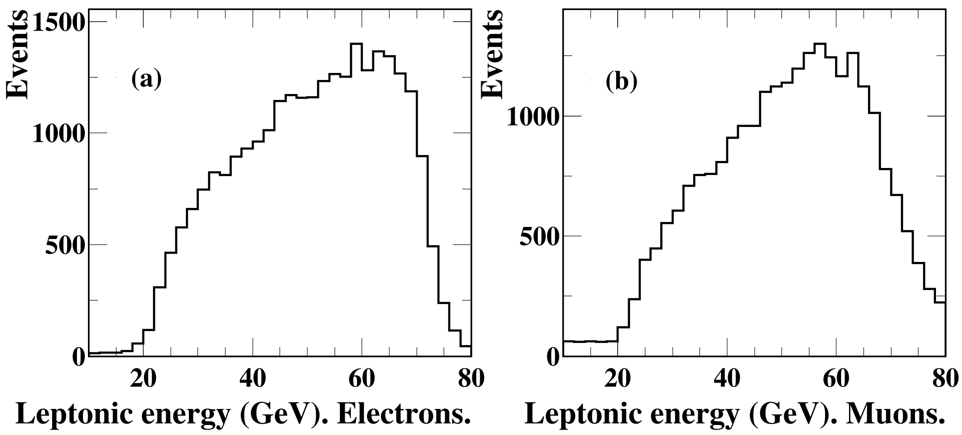

Figure 6.3: Monte Carlo leptonic energy distributions in the $W^+W^- \to \ell\nu_\ell\ell'\nu_{\ell'}$ channel including detector effects. The histograms do not include background events. (a) First class of events containing electrons using the electromagnetic calorimeter energy information. (b) Second class of events containing muons using the central track momentum information.

For the pseudomass three classes of events including different identified charged leptons are defined as follows:

1. Events including two leptons identified as e.
2. Events including two leptons identified as μ.
3. Events including two leptons identified as an e and a μ.

Figure 6.4 shows the pseudomass distribution for Monte Carlo events generated at $\mathrm{M_W}$ = 80.33 GeV at a center-of-mass energy of 189 GeV. The three classes of events are shown separately. The greater sensitivity to $\mathrm{M_W}$ of e relative to μ can be observed by comparing figures 6.4(a) (including e) and 6.4(b) (including μ) in the region sensitive to $\mathrm{M_W}$ around 80 GeV. The third figure 6.4(c) shows the third class, the mixed e-μ events. The observed number of events for the pseudomass and the leptonic energy after the selection in different classes are summarized in table 6.1. In this figure the variable is plotted between 70 and 90 GeV. This is the region chosen to fit the pseudomass in the analysis. The upper limit for the pseudomass is given by the beam energy and it changes therefore for each center–of–mass energy. Nevertheless, the sensitive region is around the generated W mass (the spectra show a sharp edge around $\mathrm{M_W}$) and the region to perform the fit can be taken between 70 and 90 GeV for every center–of–mass energy. The apparent dependence of the peak height in figure 6.2 on $\mathrm{M_W}$ is an artefact. The three spectra are normalized to the number of events and a change on the position of their sharp edges will induce a change on the height of the distributions.

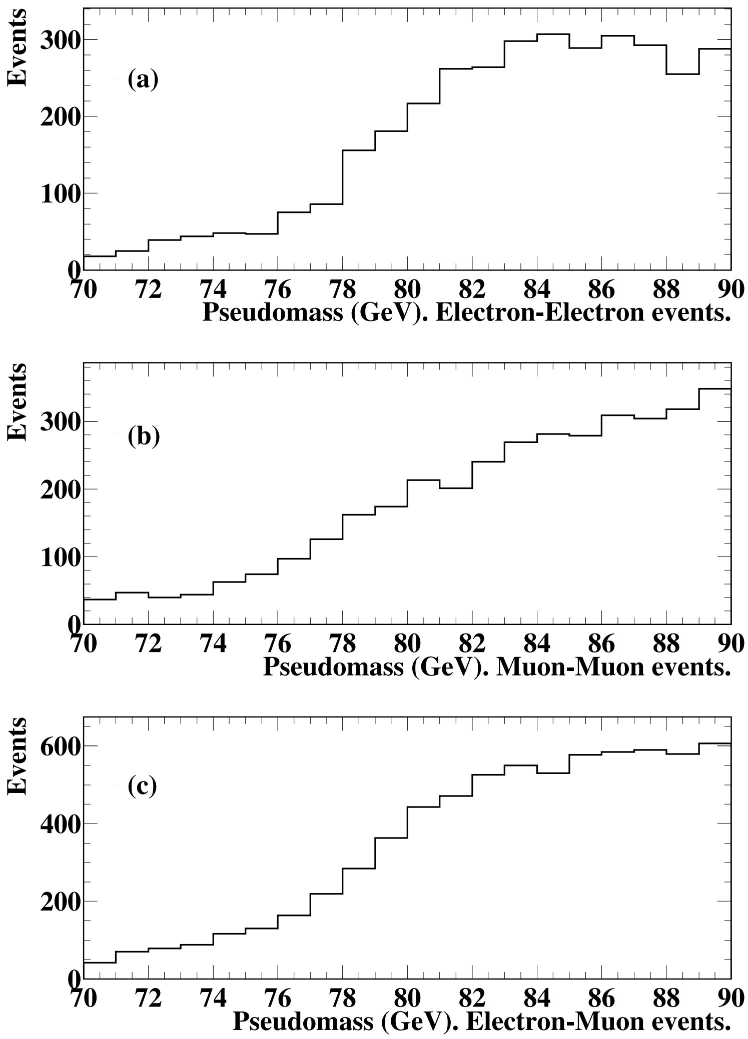

Figure 6.4: Monte Carlo pseudomass distributions in the $W^+W^- \to \ell\nu_\ell\ell'\nu_{\ell'}$ channel including detector effects. The histograms do not include background events. (a) First class of events containing electrons-electron events using the electromagnetic calorimeter energy information. (b) Second class of events containing muon-muon events using the central track momentum information. (c) Third class of events containing electron-muon events using the electromagnetic calorimeter energy and the central track momentum information.

Chapter 7

Determination of $\mathrm{M_W}$ using a Reweighting Method

This chapter presents a determination of the W boson mass, $\mathrm{M_W}$, by comparing the leptonic energy and the pseudomass distributions obtained from the data to the corresponding Monte Carlo distributions generated with a variety of $\mathrm{M_W}$. Using a reweighting technique, Monte Carlo spectra for arbitrary $\mathrm{M_W}$ can be obtained. A binned likelihood fit is then used to extract $\mathrm{M_W}$ and its error by determining which Monte Carlo spectrum best describes the data. The method does not need further correction for detector effects, Initial State Radiation or acceptance, as these effects are modeled by the simulation. In the following sections the method is explained in detail.

7.1 The Monte Carlo Reweighting Technique

The reweighting method is used to emulate a fully[1] simulated Monte Carlo spectrum which corresponds to some W mass value, $\mathrm{M_W^{new}}$, from a single Monte Carlo sample generated at a given value of the W mass, $\mathrm{M_W^{MC}}$. For each event a reweighting factor is calculated to weight the entries in the spectra of fully simulated observables, in the case of this analysis, the leptonic energy and the pseudomass. This factor, f, is defined as the probability that the generated event would be produced at $\mathrm{M_W^{new}}$ divided by the probability that this same event aroses from $\mathrm{M_W^{MC}}$. This probability is given by [90]

$$P(\mathrm{M_W}, \Gamma_\mathrm{W}, m_1, m_2) = \sigma_0(m_1, m_2, m) \times \mathcal{BW}(\mathrm{M_W}, \Gamma_\mathrm{W}, m_1) \times \mathcal{BW}(\mathrm{M_W}, \Gamma_\mathrm{W}, m_2,) \quad (7.1)$$

where σ_0 is the Born level cross section for the $\mathrm{W^+W^-}$ pair production which depends on $\mathrm{m_1}$ and $\mathrm{m_2}$, the two generated tree-level W masses and $\mathcal{BW}$ is the Breit-Wigner function,

$$\mathcal{BW}(\mathrm{M_W}, \Gamma_\mathrm{W}, m) = \frac{1}{\pi}\frac{\Gamma_\mathrm{W}}{\mathrm{M_W}}\frac{m^2}{(m^2 - \mathrm{M_W}^2)^2 + m^4\frac{\Gamma_\mathrm{W}{}^2}{\mathrm{M_W}{}^2}}, \quad (7.2)$$

[1]Full Monte Carlo simulation means the inclusion of all the detector effects in the spectrum.

The event–event reweighting factor can be written as:

$$f = \frac{\mathcal{BW}(M_W^{new},\ \Gamma_W^{new};\ m_1)\mathcal{BW}(M_W^{new},\ \Gamma_W^{new};\ m_2)}{\mathcal{BW}(M_W^{MC},\ \Gamma_W^{MC};\ m_1)\mathcal{BW}(M_W^{MC},\ \Gamma_W^{MC};\ m_2)} \tag{7.3}$$

In this analysis, only $\mathrm{M_W}$ is taken as the free parameter and Γ_W is constrained to its Standard Model value (see equation 4.5) which relates both quantities. Figure 7.1 illustrates the equation (7.3). It shows the reweighting factor f, as a function of the generated masses m_1 and m_2 in the case where a spectrum of $\mathrm{M_W^{new}}$ = 79 GeV is emulated from a Monte Carlo sample generated at $\mathrm{M_W^{MC}}$ = 80 GeV. For generated mass around 80 GeVthe reweighting factor f is below one. Events with generated masses around 79 GeV, have the maximal weights.

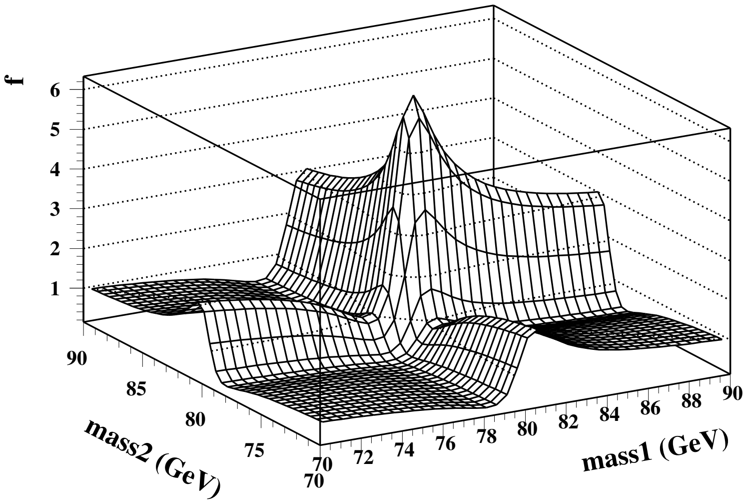

Figure 7.1: The reweighting factor distribution for $\mathrm{M_W^{new}}$ = 79 GeV, which is the mass to reweight to and $\mathrm{M_W^{MC}}$ = 80 GeVwhich is the generated Monte Carlo mass.

In order to obtain the fully simulated spectra of a certain observable after the simulation, the entries in the corresponding signal spectra are weighted according to equation (7.3). The background distributions for the spectra are generated and normalized to the expected number of background events. The reweighted signal spectra are then normalized such that the total number of signal plus background events corresponds to the observed number of events in the data. A likelihood fit is used to extract $\mathrm{M_W}$ by determining which Monte Carlo spectrum best describes the data. The likelihood function is constructed using Poisson probabilities,

$$\mathcal{L} = \prod_{i}^{N_{bins}} \frac{\lambda_i^{n_i} e^{-\lambda_i}}{n_i!} \tag{7.4}$$

The product extends over the total number of bins N_{bins}, n_i is the number of events per bin found in the data and λ_i is the expected number of events determined from Monte Carlo (containing both signal and background events). The W mass is obtained as the minimum of the $(-\log\mathcal{L})$ curve and its error from the region where $(-\log\mathcal{L})$ is smaller than 0.5.

7.1.1 Introduction of Further Monte Carlo Samples

Statistical fluctuations due to limited Monte Carlo statistics may produce reweighting factors much bigger than one for events with masses m_1 and m_2 near $\mathrm{M_W^{new}}$. It is possible to reduce such fluctuations using further Monte Carlo samples generated at different $\mathrm{M_W^{MC}}$. N Monte Carlo samples generated at masses $\mathrm{M_W^{(i)}}$, where $i = 1, ..., N$, are merged into one reweighted spectrum for $\mathrm{M_W^{new}}$ by taking the weighted average bin–by–bin. The content of bin j of the reweighted spectrum from sample i is given by [91]:

$$b_{ij} = \frac{1}{N_i}\sum_{k=1}^{n_{ij}} f_k^i \tag{7.5}$$

where $\mathrm{n_{ij}}$ is the number of events for each jth bin of the ith sample, N_i is a normalization factor, introduced to normalized each individual Monte Carlo sample before merging all in one sample and f_k^i is the corresponding reweighting factor for each event. N_i is defined such that:

$$\sum_{j}^{N_{bins}} b_{ij} = 1 \tag{7.6}$$

The total error associated to each bin is given by:

$$\Delta b_{ij} = \frac{1}{N_i}\sqrt{\sum_{k=1}^{n_{ij}}(f_k^i)^2 + \Delta\overline{b_i^2}} \tag{7.7}$$

The first term corresponds to the statistical error associated to the number of events inside each bin and the second term is an average error added in quadrature to limit fluctuations from low statistic-bins:

$$\Delta\overline{b_i^2} = \frac{1}{N_i}\frac{1}{N_{bins}}\sqrt{\sum_j\sum_{k=1}^{n_{ij}} f_k^{i2}} \tag{7.8}$$

The combined bin content in bin j is the weighted sum over all samples i:

$$b_j = \frac{\sum_{i=1}^{N}\frac{b_{ij}}{(\Delta b_{ij})^2}}{\sum_{i=1}^{N}\frac{1}{(\Delta b_{ij})^2}} \tag{7.9}$$

Monte Carlo samples with a generated W mass $\mathrm{M_W^{(i)}}$ closer to $\mathrm{M_W^{new}}$ will have a more significant impact than the other samples.

7.2 Monte Carlo Generators used in the Analysis

Samples of WW events are generated with the KORALW version 1.42 event generator with a reference W mass of 80.33 GeV. The analysis uses both samples which include CC03 events only and samples with all four–fermion processes. Additional samples generated for different W masses to build the fully simulated Monte Carlo reweighted spectrum are also used. The following Monte Carlo programs were used to generate background samples at all center of mass energies: PYTHIA was used to produce $e^+e^- \to ZZ$ and Zee events and KORALW for Weν events. Multi-photon final states were simulated with the RADCOR generator. Two-photon final states were generated with VERMASEREN. Finally, KORALZ and BHWIDE were used to generate dilepton final states. Table 7.1 summarizes all Monte Carlo samples used in the analysis.

Process	Generator	$\sqrt{s}$ (GeV)	$\mathcal{L}$(fb^{-1})	M_W (GeV)
$W^+W^- \to \ell\nu_\ell\ell'\nu_{\ell'}$	KORALW	183	36.0	80.33
$W^+W^- \to \ell\nu_\ell\ell'\nu_{\ell'}$	KORALW	189	34.1	80.33
$W^+W^- \to$ all	KORALW	189	10.9	80.33
$W^+W^- \to$ all	KORALW	192	10.8	80.33
$W^+W^- \to$ all	KORALW	196	10.8	80.33
$W^+W^- \to$ all	KORALW	200	10.8	80.33
$W^+W^- \to$ all	KORALW	202	10.8	80.33
$W^+W^- \to$ all	KORALW	183 to 202	2.7	79.33
$W^+W^- \to$ all	KORALW	183 to 202	2.7	79.83
$W^+W^- \to$ all	KORALW	183 to 202	2.7	80.83
$W^+W^- \to$ all	KORALW	183 to 202	2.7	81.33
$W^+W^- \to$ all	KORALW	192 to 202	5.3	80.08
$W^+W^- \to$ all	KORALW	192 to 202	5.3	80.58
$W^+W^- \to \ell\nu_\ell\ell'\nu_{\ell'}$	KORALW	189	5.8	78.33
$W^+W^- \to \ell\nu_\ell\ell'\nu_{\ell'}$	KORALW	189	5.6	82.33
e^+e^-	BHWIDE	all	3.0	-
$\mu^+\mu^-$	KORALZ	all	45.1	-
$\tau^+\tau^-$	KORALZ	all	49.9	-
ZZ	PYTHIA	183 and 189	34.5	-
Zee	PYTHIA	183 and 189	4.6	-
Weν	KORALW	all	162.2	-
$\nu\nu$	KORALZ	all	95.0	-
$\gamma\gamma$	RADCOR	all	7.0	-
Two-photon	VERMASEREN	all	24.1	-

Table 7.1: Monte Carlo samples used in the analysis.

7.3 Extraction of the W Mass: Monte Carlo Studies

The reweighting method was studied with Monte Carlo data generated at a center-of-mass energy of 189 GeV. The analysis was performed for the leptonic energy and for the pseudomass separately. For the leptonic energy a bin width of 2 GeV was used in an energy region between 10 and 80 GeV. For the pseudomass the fit was performed with a bin width of 1 GeV between 70 and 90 GeV. In both cases, these regions are most sensitive to $\mathrm{M_W}$. The total likelihood function for the pseudomass, $\mathcal{L}_\mathrm{P}$, and for the lepton energy, $\mathcal{L}_\mathrm{E}$, are defined as the product of the individual, $\mathcal{L}_\mathrm{i}$, likelihood functions defined for each class i of events; three functions are therefore defined for the pseudomass and two for the leptonic energy.

$$\mathcal{L}_{P/E} = \prod_i \mathcal{L}_i \tag{7.10}$$

The expected statistical error on $\mathrm{M_W}$ for each variable is estimated via an ensemble test with 1000 Monte Carlo subsamples. Each subsample contains signal and background events in the expected proportion for an integrated luminosity of 183 pb^{-1}. The signal events are obtained from a Monte Carlo sample generated at a W mass of 80.33 GeV (considered as the "data" sample) and the background events from the corresponding samples shown in Table 7.1. Signal and background events of each subsample are chosen randomly from the corresponding Monte Carlo samples. First a number of background events is selected, then the sample is filled with signal events until the total number of events in each subsample is equal to the observed number in the data. Due to the finite Monte Carlo statistics each event can appear in more than one subsample for an ensemble of 1000 subsamples. It was shown in [92] that the multiple inclusion of events in the subsamples should not introduce a bias in the expected statistical error if the number of subsamples is less than $(\mathcal{N}/\mathrm{n})^2$, where n is the number of events per subsample and $\mathcal{N}$ is the total pool of events included in the large Monte Carlo sample taken as the "data".

The reweighting fit is repeated for each subsample and the corresponding W mass and the error are obtained by the the minimization package `MINUIT` [93]. The fit statistical errors are taken to be the Mean value of the corresponding distributions shown in Figure 7.2. Most of the samples have fit errors close to the mean value of the distribution but a considerable number of subsamples have fit errors much larger than the mean value. Further tests showed that the likelihood functions of these subsamples have a non–parabolic shape and poorly defined minima leading to the large fit errors. This effect is due to the low statistics avaible per sample to perform the fit. The number of events found in the region sensitive to $\mathrm{M_W}$ is very small and this low number of events can produce statistical fluctuations. Additional Monte Carlo tests were performed varying the number of events per subsample. The fraction of subsamples with poorly defined minima strongly decreases when increasing the number of events per subsample.

To minimize the statistical fluctuations in the fit, the leptonic energy and the pseudomass were combined in one simultaneous fit including $\mathrm{W^+W^-} \to \ell\nu_\ell\ell'\nu_{\ell'}$ events recorded at center-of-mass energies of $\mathrm{E_{CM}}$ = 183, 189, 192, 196, 200 and 202 GeV. In this simultaneous fit the total likelihood function is defined as:

$$\mathcal{L}_T = \prod_{k=1}^{6}(\prod_{i=1}^{3}\mathcal{L}_P^k \times \prod_{i=1}^{2}\mathcal{L}_E^k) \tag{7.11}$$

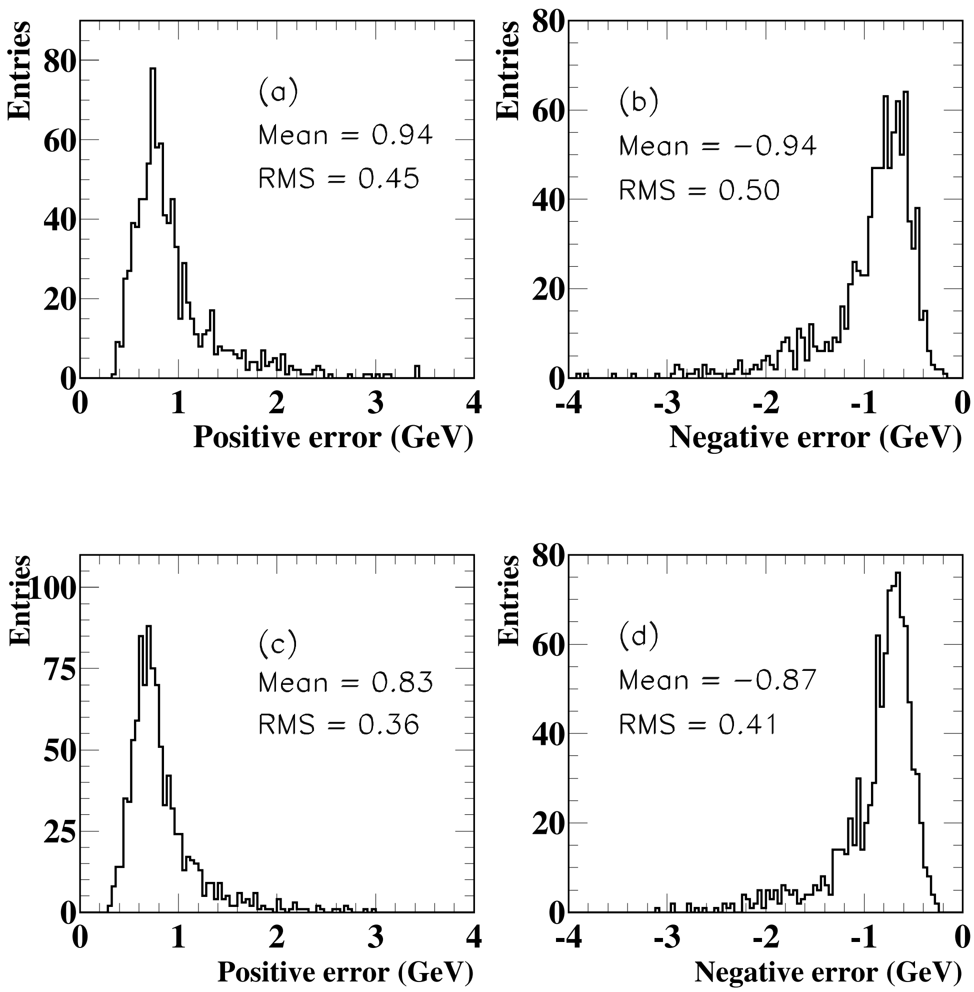

Figure 7.2: Fit asymmetric error distributions at 189 GeV for the sensitive variables. (a) Positive error distribution for the pseudomass. (b) Negative error distribution for the pseudomass. (c) Positive error distribution for the leptonic energy. (d) Negative error distribution for the leptonic energy.

where k denotes each center-of-mass energy and $\mathcal{L}_P^k$ the likelihood function for the pseudomass and $\mathcal{L}_E^k$ for the leptonic energy.

For the additional energies, the fit is again performed between 70 and 90 GeV for the pseudomass with a bin width of 1 GeV. For the leptonic energy the energy region is adjusted for each center-of-mass energy, in order not to lose sensitivity at the upper end of the spectrum. The different energy regions for each center-of-mass energy are summarized in table 7.2.

Figure 7.3 shows the fit error distributions after the simultaneous fit for the pseudomass and

$\sqrt{s}$ (GeV)	183	189	192	196	200	202
Low (GeV)	10	10	10	10	10	10
Up (GeV)	80	80	84	90	90	92

Table 7.2: Energy regions considered in the fit for the leptonic energy variable depending on the center-of-mass energy.

the leptonic energy including all center-of-mass energies. The effect of the statistical fluctuations is notably reduced.

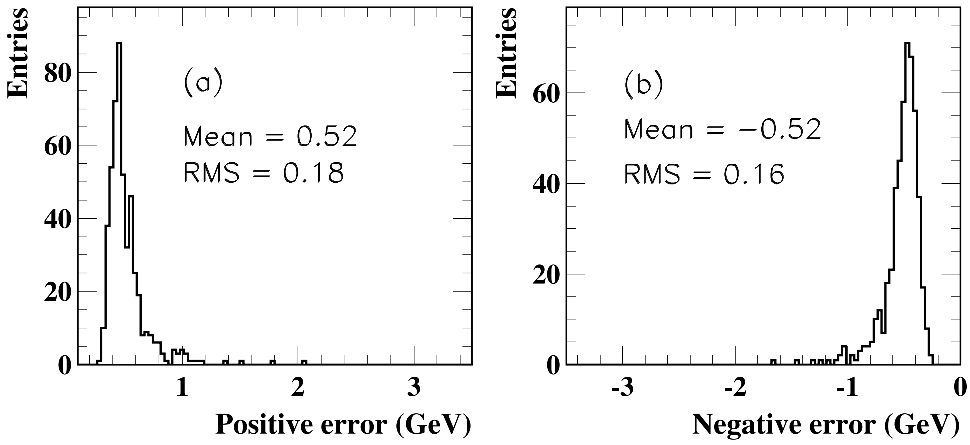

Figure 7.3: Fit error distributions for the simultaneous fit to all center-of-mass energies to the pseudomass together with the leptonic energy distribution. (a) Positive error distribution. (b) Negative error distribution. Both distributions are rescaled by a factor 1.13 to take into account the correlation between the pseudomass and the leptonic energy.

However, one problem remains; positive and negative errors can differ substantially, as shown in figure 7.4. This makes it difficult to combine the results with other measurements of $\mathrm{M_W}$.

In order to demonstrate that the method is bias free and the extracted errors are correct, the fitted mass and the pull distributions are analysed. The pull is defined as:

$$Pull = \frac{M_W^{meas} - M_W^{true}}{\sigma_M^{meas}} \tag{7.12}$$

where $\mathrm{M_W^{meas}}$ is the fitted $\mathrm{M_W}$ for each subsample, $\mathrm{M_W^{true}}$ is the generated mass of the large sample taken as the "data" and $\sigma_{\mathrm{M}}^{\mathrm{meas}}$ is the fitted error for the corresponding subsample [91].

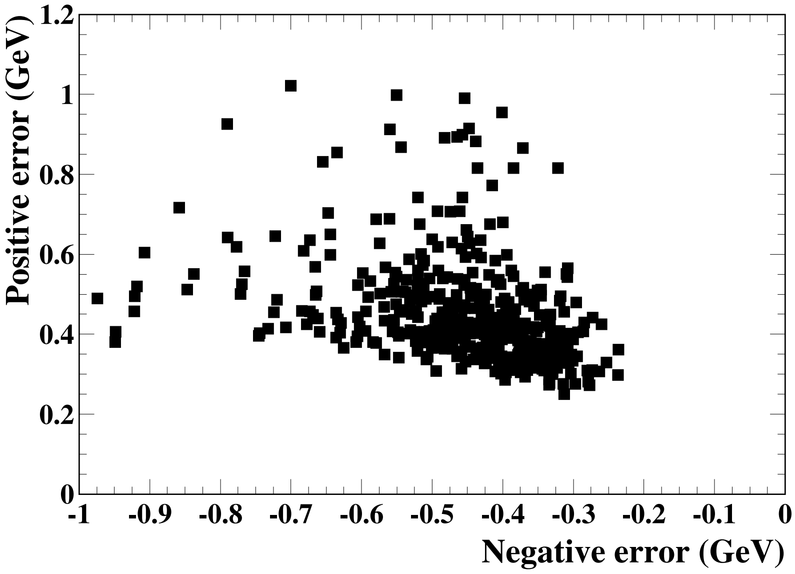

Figure 7.4: Comparison between the fit positive and negative errors for the simultaneous fit considering at all center-of-mass energies.

The determination of the fitted mass and its error is unbiased, if the pull distribution is consistent with a Gaussian with a mean of zero and a with of one. To take into account the asymmetric errors, the pulls are defined for this analysis as follows:

$$Pull = \begin{cases} \frac{M_W^{meas} - M_W^{true}}{\sigma_M^{meas+}} & \text{if } M^{meas} < M^{true} \\ \frac{M_W^{meas} - M_W^{true}}{\sigma_M^{meas-}} & \text{if } M^{meas} > M^{true} \end{cases}$$

where $\sigma^{\mathrm{meas}+(-)}$ are the positive (negative) error.

Figure 7.5(a) shows the fitted mass distribution and 7.5(b) the corresponding pull. A Gaussian fit was performed. In the case of the mass distribution, the width of this Gaussian is taken as the expected error for the analysis. This value is in good agreement with the mean value of the fit error distributions (Figure 7.3). The simultaneous fit however does not consider the possible correlation between the leptonic energy and the pseudomass which leads to an underestimation of the fit error. This correlation is computed using independent[2] Monte Carlo subsamples at center-of-mass energies from 183 to 202 GeV and repeating the reweighting procedure for the pseudomass and for the leptonic energy separately. The obtained correlation factor is 13%, which can be accounted for rescaling the fit error by a factor 1.13. After that the pull width is

[2]The random sampling to collect events for each subsample is not used for this study. Each signal event is used in only one sample once to avoid additional correlations between the subsamples.

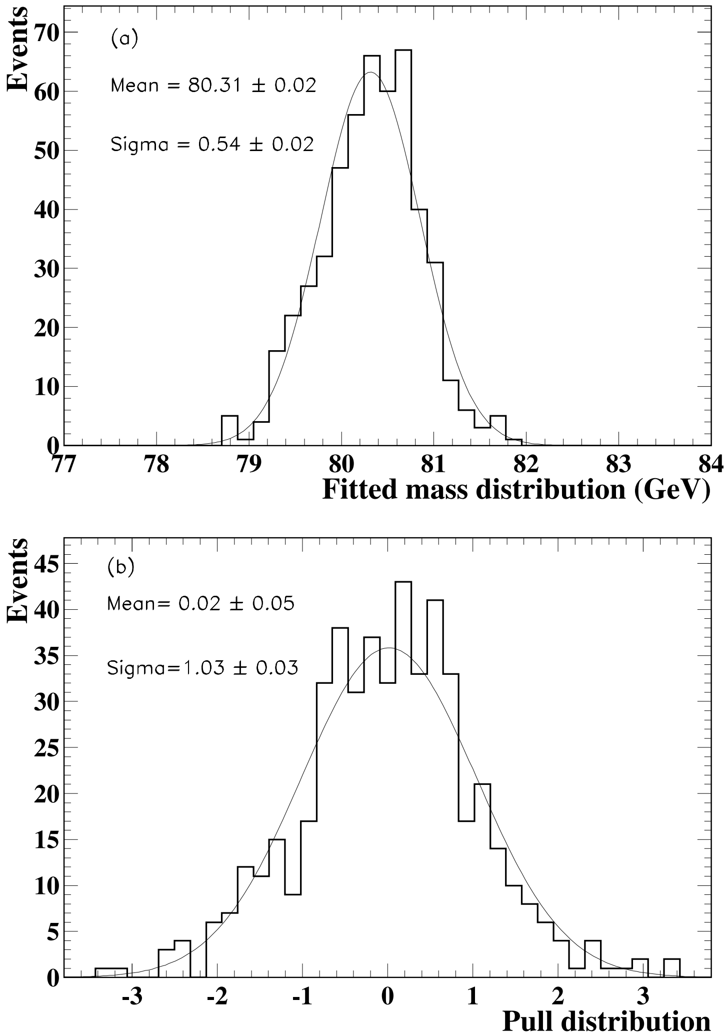

Figure 7.5: (a) Fitted mass distributions from Monte Carlo at all center-of-mass energies for the simultaneous fit of the pseudomass and the leptonic energy. The test samples are generated at M_W = 80.33 GeV. (b) Pull distribution. The corresponding errors are rescaled by a factor 1.13 to take into account the correlation between the pseudomass and the leptonic energy.

consistent with unity. Appendix B gives a brief description how the correlation factor is determined. This factor is already included in the fit error distributions shown in figure 7.3 and in the pull distribution definition. The relation between the M_W values derived from these variables can be seen in figure 7.6. The small correlation between the leptonic energy and the pseudomass arises from two factors:

- For the leptonic energy, events $e - \tau$ and $\mu - \tau$ are used. This leads to an additional information for the leptonic energy.
- The fact that the common information for the leptonic energy and the pseudomass is used in different ways (in the case of the leptonic energy both charged leptons are used independently, in the case of the pseudomass the correlation between the lepton energies and their angles are taken into account) decreases the correlation factor.

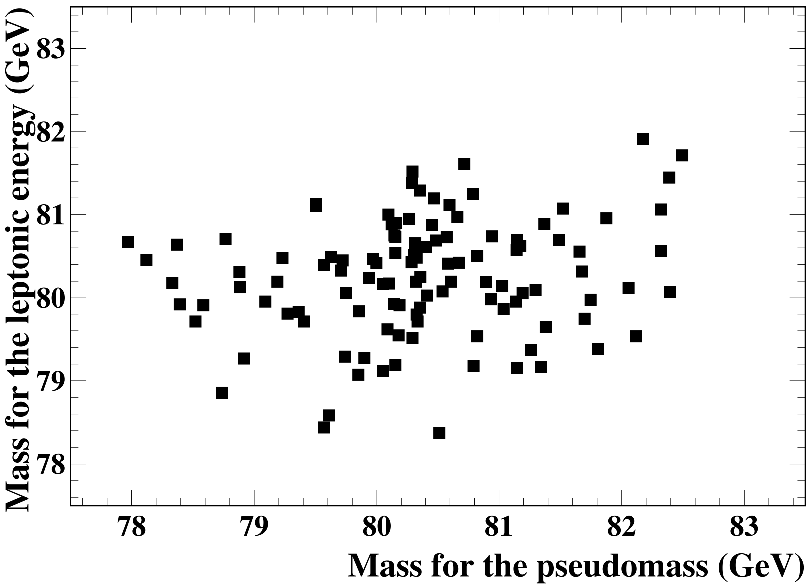

Figure 7.6: Fitted mass distribution at all center-of-mass energies for the pseudomass in comparison with the one for the leptonic energy. 112 independent Monte Carlo subsamples were used in the analysis.

7.4 Results of the Reweighting Method

The center-of-mass energy values between the data and Monte Carlo differ at 183 and 189 GeV. The corresponding center–of–mass energies in the data are 182.68 and 188.64 GeV respectively. Therefore it is necessary to introduce a correction in the fit to the data. The momenta of the charged leptons in Monte Carlo are rescaled by factors $\mathrm{f_{res}}$, $\mathrm{f_{res}} = \sqrt{\mathrm{s}}_{\mathrm{MonteCarlo}}/\sqrt{\mathrm{s}}_{\mathrm{data}}$. These factors are used to rescale the generated W mass and the fitted W mass in the reweighting factor. Such a correction is not used for energies between 192 and 202 GeV because they agree with the values in the data.

The simultaneous fit for the pseudomass and the leptonic energy combining all center-of-mass energies gives the following result:

$$\boxed{\mathrm{M_W} = 80.30^{+0.48}_{-1.55}\ \mathrm{GeV}}$$

The quoted errors are the statistical errors derived from the fit to the data.

The error is rather asymmetric which is caused by the double peak structure of the likelihood curve shown in Figure 7.7. The curve on the low side of the minimum only increases by 0.3 before reaching a local minimum which causes a large asymmetric error. Such an effect is not unusual as Monte Carlo studies show [62].

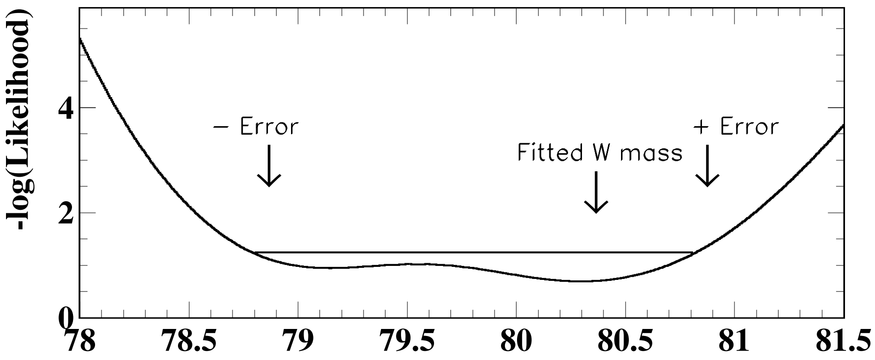

Figure 7.7: $-\log\mathcal{L}$ curve obtained from the fit to the real data. The fitted W mass and the asymmetric errors are shown with arrows.

Figure 7.8 shows the two classes defined for the leptonic energy depending on the lepton flavor for the data in comparison with the Monte Carlo distribution for the best fit to the data, including as well the events for the background. Figure 7.9 shows the same distributions for the three classes defined for the pseudomass. The good agreement between data and Monte Carlo can be seen in all these plots. Similar results are obtained at all center-of-mass energies.

7.5 Systematic Checks and Uncertainties

The determination of the systematic uncertainties of $\mathrm{M_W}$ measurement is performed by repeating the simultaneous fit to the pseudomass and the leptonic energy spectra with shifted or smeared parameters. The deviation in the new fit result is taken as systematic error. The study of these uncertainties are summarized in table 7.3. Initial state radiation and four-fermion effects were studied at a center-of-mass energy of 189 GeV. The other sources have been studied simultaneously for all center-of-mass energies.

Systematic errors	Error (MeV)
Beam energy	12
Spread in the beam energy	10
ISR	< 10
Four-fermion	42
ECAL scale	101
ECAL resolution	83
CT scale	14
CT resolution	18
Background	12
Total	140

Table 7.3: Summary of systematic uncertainties on $\mathrm{M_W}$ measurement using a reweighting method.

7.5.1 Beam Energy

The error of the LEP beam energy is ± 21 MeV [94]. This corresponds to a relative uncertainty of 0.02%. The effect of this uncertainty on the measured $\mathrm{M_W}$ is determined by refitting the Monte Carlo test samples with the three-momenta for both the electromagnetic calorimeter and the central track detector scaled by 1.0002. Such a change corresponds to a sample generated with both $\sqrt{\mathrm{s}}$ replaced by $1.0002 \times \sqrt{\mathrm{s}}$ and $\mathrm{M_W}$ replaced by $1.0002 \times \mathrm{M_W}$. Since here one is only interested in the $\sqrt{\mathrm{s}}$ change, the systematic error is estimated by comparing the fitted $\mathrm{M_W}$ with the W mass from the original fit scaled by 1.0002. The mean shift in the fitted mass is 12 MeV and is taken as the associated systematic uncertainty. The systematic error due to the spread in the LEP beam energy was measured by smearing the energy of the charged leptons with a Gaussian distribution, with a width of 240 MeV, the spread in the LEP beam energy [94]. The corresponding systematic error is 10 MeV.

7.5.2 Initial State Radiation

The systematic error associated with uncertainties in the modelling of Initial State Radiation is estimated by comparing KORALW Monte Carlo $\mathrm{W^+W^-}$ events reweighted using a $O(\alpha)$ and $O(\alpha^2)$ treatment of initial state radiation to the standard $\mathrm{W^+W^-}$ sample which includes $O(\alpha^3)$ treatment. In the case of the $O(\alpha)$ correction a mean difference of 6 MeV is obtained and 4 MeV in the case of $O(\alpha^2)$. The larger is taken as systematic error.

7.5.3 Four-Fermion Effects

The generated reference samples at 183 and 189 GeV do not include a complete set of four-fermion diagrams and neglect interference effects between $\mathrm{W^+W^-}$ diagrams and other four-fermion processes. In order to check the systematic error due to these effects, the fit results of a sample generated including the full set of interfering four-fermion diagrams (GRACE generator [87]) are compared to the same events, but reweighted to the CC03 $\mathrm{W^+W^-}$ diagrams alone, which results in a difference of 42 MeV. This difference is taken as the systematic uncertainty.

7.5.4 Detector and Resolution Effects

The effects of the detector calibrations and the uncertainties in the Monte Carlo simulation of the detector response are investigated by varying the observed lepton energy scales in the electromagnetic calorimeter (for the electrons) and in the central detector (for the muons) by $\pm 0.3\%$ [51]. The systematic error due to this source is 101 MeV for the electromagnetic calorimeter and 14 MeV for the central track detector. The study was performed independently for both.

For the resolution effect, the difference between the measured, $\mathrm{E_{meas}}$ and the generated energy, $\mathrm{E_{gen}}$, was changed as follows:

$$\mathrm{E_{new}} = \mathrm{E_{gen}} + \mathrm{f_r}(\mathrm{E_{meas}} - \mathrm{E_{gen}})$$

where $\mathrm{E_{new}}$ is the new energy and $\mathrm{f_r}$ is the resolution factor, $\mathrm{f_r} = 1.03$ for the electromagnetic calorimeter and $\mathrm{f_r} = 1.08$ for the central track detector. The systematic error due to this source is 83 MeV and 18 MeV respectively. The study was also performed independently.

The quoted systematic error due to energy scale and resolution effect are for the combined result of the electrons and muons. Electrons have a rauch larger weight in the combination therefore the effect of the electromagnetic calorimeter energy scale variation is much larger.

7.5.5 Background Treatment

The background normalization is varied by $\pm 25\%$, which contains both the corresponding error in the cross section measurement for the leptonic channel (5%) and the uncertainty of the actual number of background events in the data due to statistical fluctuations. The resulting change in the fitted $\mathrm{M_W}$ is 12 MeV.

7.6 Test of the Reweighting Method

7.6.1 Bin Width

One of the principal intrinsic parameters of the reweighting method is the width of the bins. A small bin size will improve the resolution of the sensitive variables as long as the Monte Carlo statistics are large enough to allow smooth reweighted spectra for the pseudomass and the leptonic energy. On the other hand, a bin size too small will increase the fluctuations in the final result. The bin width is varied simultaneously for the leptonic energy and the pseudomass in a range of 1.0-1.75 GeV for the former and 2.0-2.75 GeV for the latter. The maximal change in the fitted mass is 24 MeV, which is well within the expected statistical scatter. The position of the bin centers is also varied by up to 0.5 GeV. The maximal shift of 14 MeV is again not significant. No systematic error was assigned because of these effects.

7.6.2 Linearity of the Reweighting Procedure

An important check of any fit method is to test for a possible bias and the linearity of the procedure. In principle, the reweighting method should be linear and bias-free by construction. In order to test it, Monte Carlo samples generated at center-of-mass energies of 79.33, 79.83, 80.33

80.83 and 81.33 GeVare used. These are the available samples for all center-of-mass energies from 183 to 202 GeV. The relation between the generated and the fitted mass is found to be linear for the combination in a region of ±0.5 GeV, with a slope of 0.98±0.16 (see figure 7.10). There is no evidence of non-linear behavior in the range of several 500 MeV around the central value and our measured value lies safely within this region. On the other hand the figure shows no bias effects in this range. Therefore no additional error is assigned for this effect.

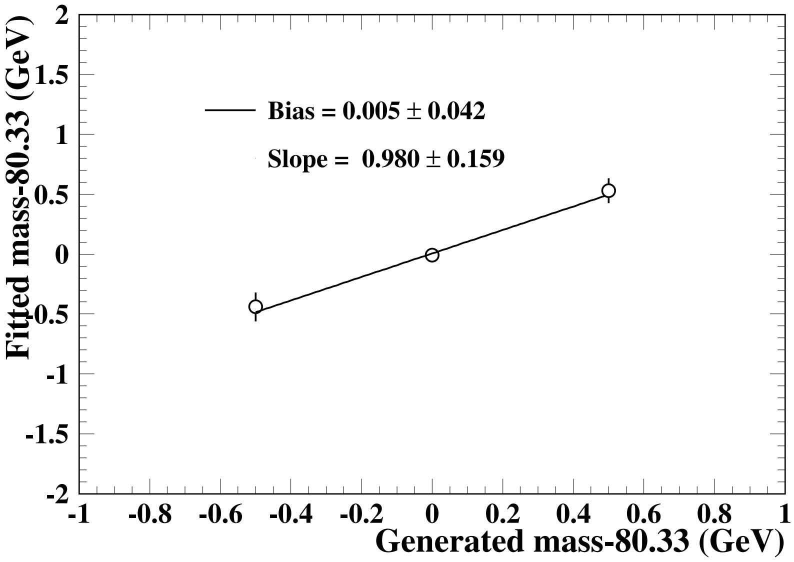

Figure 7.10: Linearity of the reweighting method procedure. The central value of 80.33 GeV is subtracted from all the masses.

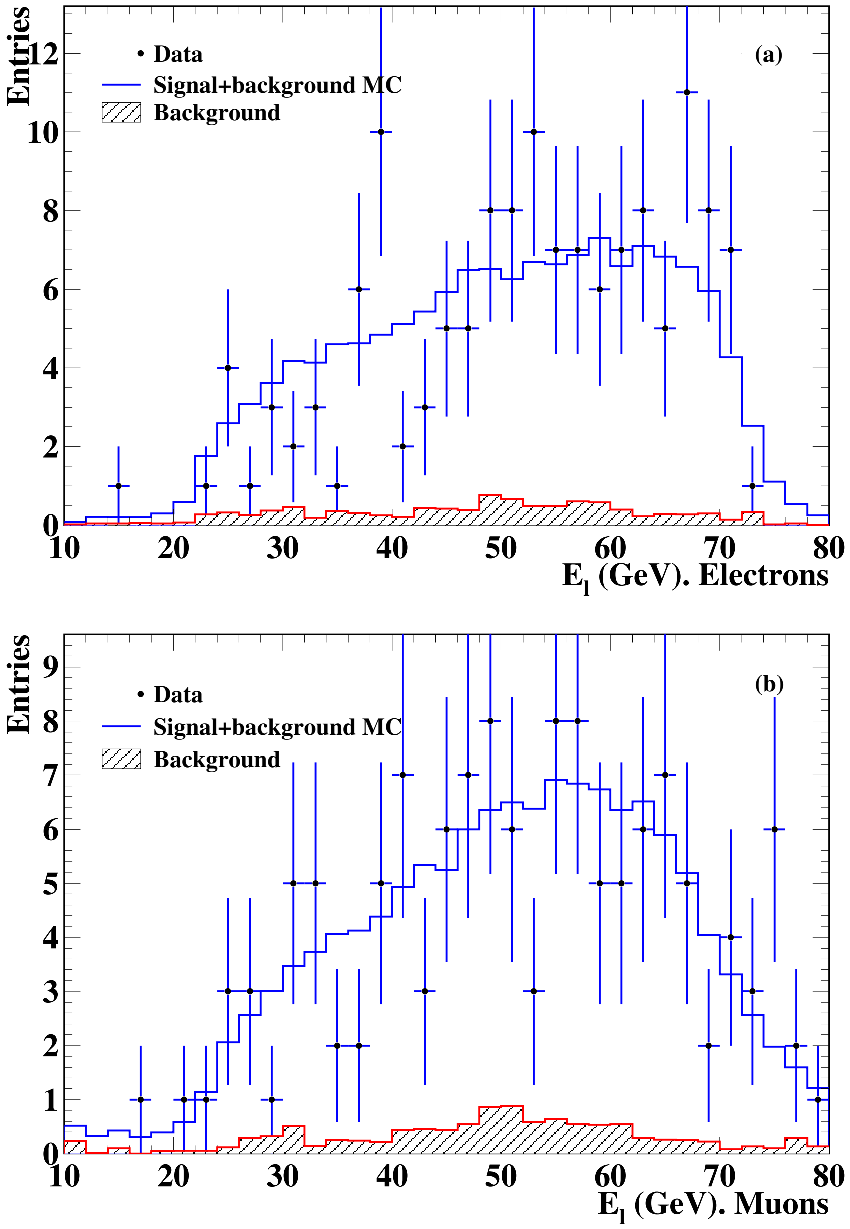

Figure 7.8: Leptonic energy distributions in the $\mathrm{W^+W^-} \to \ell\nu_\ell\ell'\nu_{\ell'}$ channel at a center-of-mass energy of 189 GeV for data (points with error bars), background Monte Carlo (shaded area) and signal+background Monte Carlo for the best fit to the data (solid histogram). Detector effects are included. (a) First class containing electrons using electromagnetic calorimeter energy information. (b) Second class containing muons events using central track momentum information.

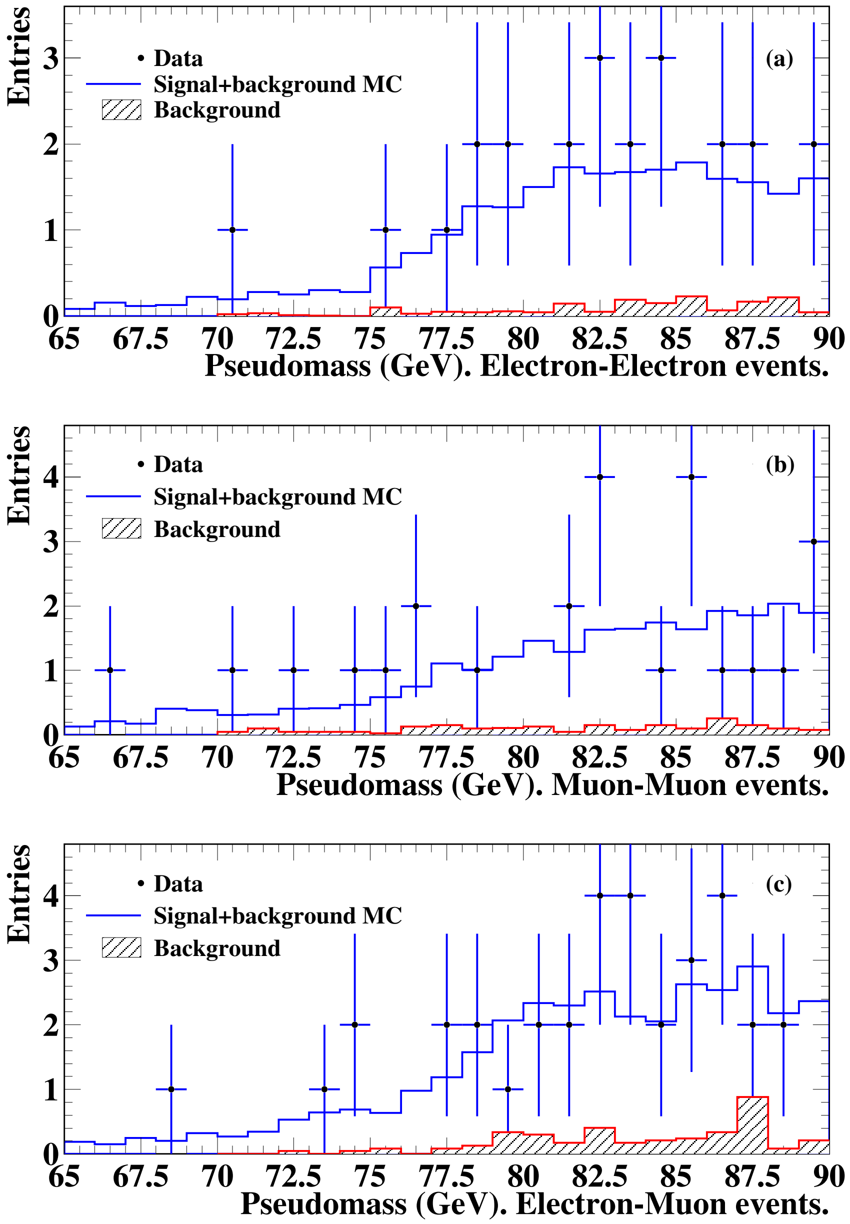

Figure 7.9: Pseudomass distributions in the $\mathrm{W}^+\mathrm{W}^- \to \ell\nu_\ell\ell'\nu_{\ell'}$ channel at a center-of-mass energy of 189 GeV for data (points with error bars), background Monte Carlo (shaded area) and signal+background Monte Carlo for the best fit to the data (solid histogram). Detector effects are included. (a) First class of events containing electron-electron events using electromagnetic calorimeter energy information. (b) Second class of events containing muon-muon events using central track momentum information. (c) Third class of events containing electron-muon events using the electromagnetic calorimeter and the central track detector informations.

Chapter 8

Determination of $\mathrm{M_W}$ using an Unbinned Maximum Likelihood Fit

This chapter describes an alternative method to determine $\mathrm{M_W}$ from $\mathrm{W^+W^-} \to \ell\nu_\ell\ell'\nu_{\ell'}$ events based on an unbinned likelihood fit. The reweighting method, discussed in the previous chapter, suffers from statistical fluctuations due to the limited size of the available Monte Carlo samples which are used to derive the reference spectra. This gives rise to:

- Asymmetric errors.
- Occasional subsamples with very large errors (figure 7.3).

In particular, the asymmetry of the statistical error makes it difficult to combine the result with other OPAL and LEP $\mathrm{M_W}$ measurements from $\mathrm{W^+W^-} \to \mathrm{q_1\overline{q}_2q_3\overline{q}_4}$ and $\mathrm{W^+W^-} \to \mathrm{q_1\overline{q}_2}\ell\nu_\ell$ events. In order to overcome these problems an alternative method to determine $\mathrm{M_W}$ in the leptonic channel was developed. The basic idea is the parameterization of the simulated pseudomass and the leptonic energy spectra (including the background) by analytical functions. A linear dependence of the parameters which are included in the analytical functions on the W mass is assumed. The W mass and its error is then obtained in an unbinned likelihood fit which determines for which W mass the analytic function describes better the spectra of the sensitive variables.

8.1 General Description of the Method

The pseudomass and the leptonic energy distributions obtained from the Monte Carlo simulation (including all background sources) are parametrized by appropriate analytical functions, f:

$$f = f(P_1, \cdots, P_N, x) \tag{8.1}$$

which depend on N parameters, P_i, and x, the values of the leptonic energy or the pseudomass. For each parameter a linear dependence on $\mathrm{M_W}$ is assumed:

$$P_i = b_i^0 + b_i^1 \times \mathrm{M_W} \tag{8.2}$$

The coefficients b_i^0 and b_i^1 are obtained by fitting the pseudomass and leptonic energy spectra generated for different W masses with the analytical function. The linear dependence of each parameter on $\mathrm{M_W}$ is studied separately. Only in the case b_i^1 is signicantly different from zero a dependence on $\mathrm{M_W}$ is assumed; otherwise the parameter is fixed by the constant term b_i^0. This parameterization is performed independently for each class of events (see chapter 6) defined for the sensitive variables. Details of the method are discussed in the following sections.

In the end, the W mass is determined from the data by an unbinned maximum likelihood based on these functions:

$$\mathcal{L} = \prod_j f(P_i(\mathrm{M_W}), x_j) \tag{8.3}$$

where j denotes the events for the pseudomass and the leptonic energy. The different center-of-mass energies between 183 and 202 GeV are taken into account in a simultaneous fit to both sensitive variables. The general likelihood function is identical to the one defined in equation (7.11).

8.1.1 Parameterization of the Leptonic Energy

The leptonic energy spectrum is fitted with a function f_T, which is the product of *two Fermi functions* and a *linear function*.

$$f_T = f_1 \times f_2 \times f_3 \tag{8.4}$$

with

$$f_1 = \frac{1}{e^{\frac{-(x-P_1)}{P_2}} + 1}, \quad f_2 = P_5 + P_6 \times x, \quad f_3 = \frac{1}{e^{\frac{x-P_3}{P_4}} + 1} \tag{8.5}$$

$\mathrm{P_1}$ and $\mathrm{P_3}$ correspond to the middle points of the two Fermi functions, $\mathrm{P_2}$ and $\mathrm{P_4}$ to their widths, $\mathrm{P_5}$ is the constant term of the linear function and $\mathrm{P_6}$ is its slope.

The fit depends therefore on six parameters. The overall normalization of the spectra can be used to determine $\mathrm{P_5}$. Figure 6.1 illustrates that the edges of the leptonic energy spectrum are the regions sensitive to $\mathrm{M_W}$. In terms of the parameterization these edges correspond to $\mathrm{P_1}$ and $\mathrm{P_3}$. These are the only parameters which are expected to change for different W masses while the other parameters, $\mathrm{P_2}$, $\mathrm{P_4}$ and $\mathrm{P_6}$ are more sensitive to the W width and detector resolution effects. Figure 8.1 shows an example of a function f_T fitting a leptonic energy distribution. The spectrum is generated with from a Monte Carlo sample with a W mass of 80.33 GeV at a center–of–mass energy of 189 GeV. The fit is performed with five free parameters.

A simultaneous fit of the parameters $\mathrm{P_1}$, $\mathrm{P_2}$, $\mathrm{P_3}$, $\mathrm{P_4}$ and $\mathrm{P_6}$ with all Monte Carlo samples was performed. $\mathrm{P_2}$, $\mathrm{P_4}$ and $\mathrm{P_6}$ are assumed to be independent of $\mathrm{M_W}$; therefore one global value was determined for each. $\mathrm{P_1}$ and $\mathrm{P_3}$ describe the $\mathrm{M_W}$ dependence and an independent value was determined for each Monte Carlo $\mathrm{M_W}$. Figure 8.2 shows the fitted $\mathrm{P_1}$ and $\mathrm{P_3}$ parameters and the linear dependence on $\mathrm{M_W}$ in the case of electrons. These fits are performed independently for each class of events and each center–of–mass energy.

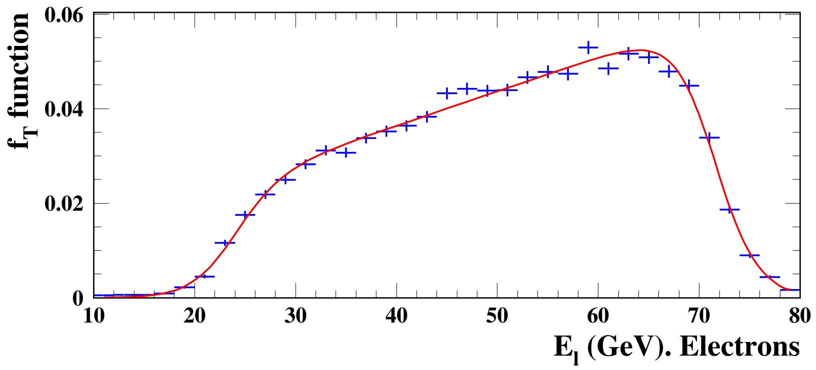

Figure 8.1: Fit to the leptonic energy distribution generated with a W mass of 80.33 GeV at $\sqrt{s}$ = 189 GeV. The Monte Carlo data belongs to the first class defined for the leptonic energy, i.e, it contains electrons only. The crosses correspond to the Monte Carlo data. The indicated error are the ones used in the averaging algorithm (see section 7.3). The fit is performed with two Fermi functions and a linear function with five free parameters as defined in equation (8.5).

The likelihood fit which determines $\mathrm{M_W}$ is performed therefore with two free parameters, $\mathrm{P_1}$ and $\mathrm{P_3}$, leaving $\mathrm{P_2}$, $\mathrm{P_4}$ and $\mathrm{P_6}$ fixed. The constant values chosen for these parameters to perform the likelihood fit are those shown by the coefficients b^0 of their corresponding linear fits. The determination of the parameters was repeated independently for each class defined for the leptonic energy and for each center-of-mass energy from 183 to 202 GeV. In all cases the results confirmed $\mathrm{P_1}$ and $\mathrm{P_3}$ as the most sensitive parameters. The numerical values of all parameters for center-of-mass energies from 183 to 202 GeVand for each class is summarized in tables C.1 and C.2 in Appendix C.

The sensitivity of the function f_T with five free parameters to $\mathrm{M_W}$ is illustrated in figure 8.3.

8.1.2 Parameterization of the Pseudomass

The analytical function chosen to fit the pseudomass spectra is the sum of a *Fermi function* and a constant function, with four free parameters:

$$f = \frac{P_1}{e^{\frac{-(x-P_2)}{P_3}} + 1} + P_4 \tag{8.6}$$

where $\mathrm{P_1}$ is the height of the curve, $\mathrm{P_2}$ corresponds to the middle point of the slope, $\mathrm{P_3}$ is the width and $\mathrm{P_4}$ is chosen as a constant term. As for the leptonic energy, one parameter is fixed by the overall normalization of the spectra. This procedure is used to eliminate the parameter $\mathrm{P_1}$. Figure 6.2 shows a sharp edge on the value of the pseudomass corresponding to the generated

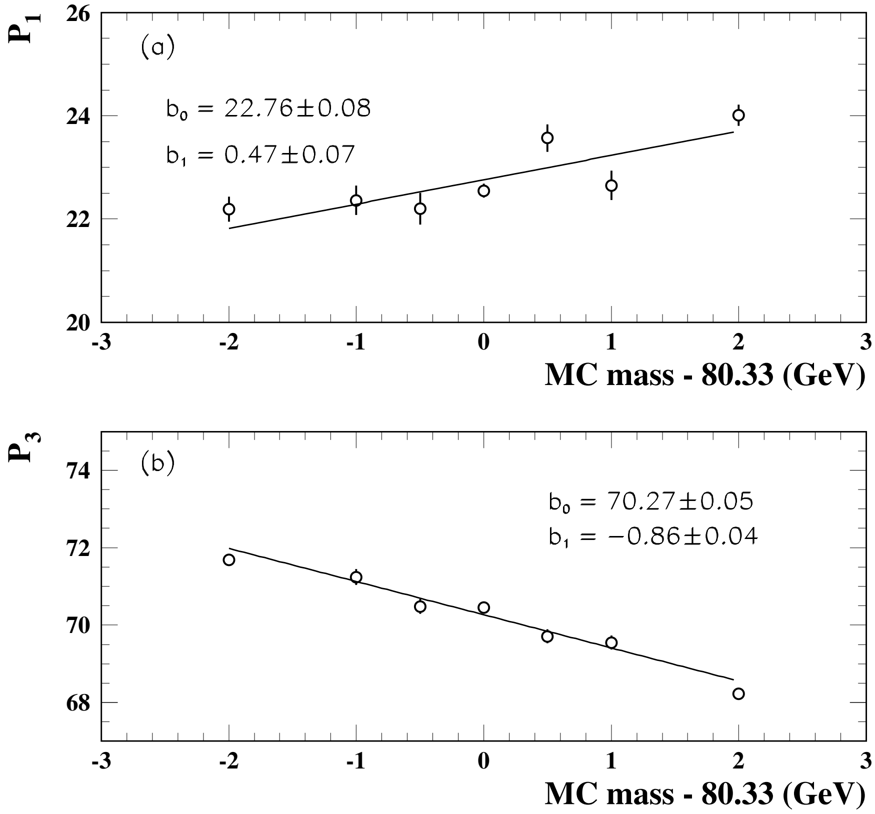

Figure 8.2: Linear fit of the coefficients P_1 (a) and P_3 (b) (middle points of the Fermi functions) to $\mathrm{M_W}$ at a center-of-mass energy of 189 GeV. The central value of 80.33 GeV is subtracted from all generated W masses. The events chosen to perform this fit belong to the first class defined for the leptonic energy, which contains electrons only. Similar studies were performed for the second class at all center-of-mass energies.

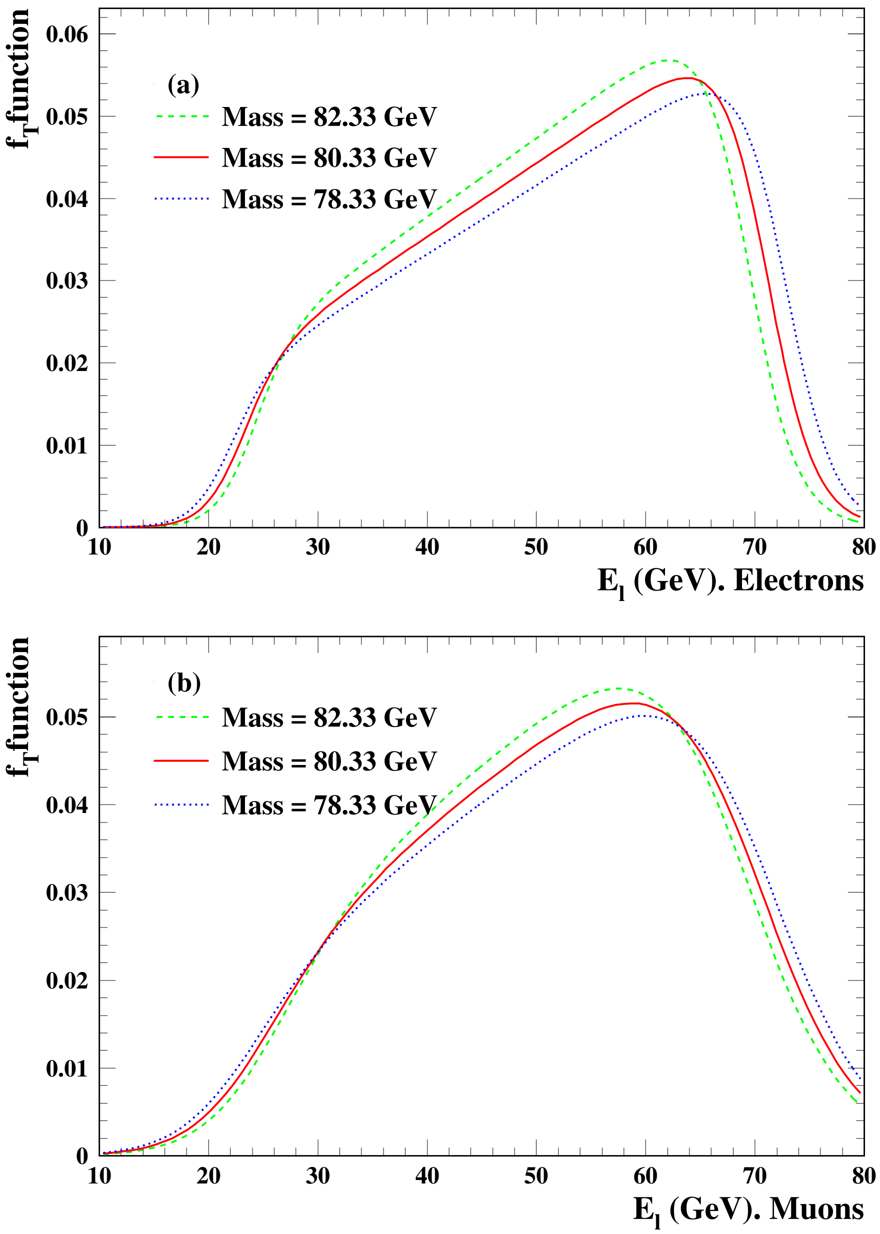

Figure 8.3: Comparison of f_T functions for three different generated masses: 78.33 GeV (dotted line), 80.33 GeV (solid line) and 82.33 GeV (dashed line) at a center-of-mass energy of 189 GeV. (a) First class defined for the leptonic energy which contains electrons. (b) Second class defined for the leptonic energy which contains μ.

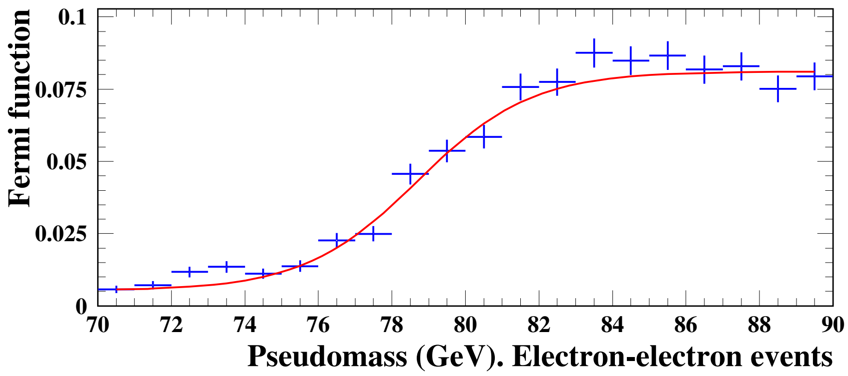

Figure 8.4: Fit to the pseudomass distribution generated at 80.33 GeV at $\sqrt{s}$ = 189 GeV. The crosses correspond to the Monte Carlo data. The indicated error are the ones used in the averaging algorithm, (see section 7.3). The fit is performed with a Fermi function with three free parameters.

W mass. In terms of the above parameterization, this edge corresponds to P_2. This is the only parameter which is expected to show a clear dependence on M_W. Figure 8.4 shows an example of the function fitting a pseudomass distribution. Similar fits were performed for each class of events at all center-of-mass energies considered in the analysis.

The individual linear dependence of each parameter on M_W is studied as for the leptonic energy. A simultaneous fit of the parameters P_2, P_3 and P_4 with all Monte Carlo samples was performed. P_3 and P_4 are assumed to be independent of M_W; therefore one global value was determined for each. P_2 describes the M_W dependence and an independent value was determined for each Monte Carlo M_W. Figure 8.5 shows the fitted P_2 parameter and the linear dependence on M_W in the case of e-e events. These fits are performed independently for each class of events and each center–of–mass energy. The numerical values of the parameters are summarized in tables C.3, C.4 and C.5 in Appendix C.

The sensitivity of the Fermi functions which fit the pseudomass spectra is illustrated in a similar way to the leptonic energy. Figure 8.6 shows the dependence on M_W for the three classes of events defined for the pseudomass at a center-of-mass energy of 189 GeV.

8.2 Extraction of the W Mass: Monte Carlo Studies

The extraction of the W mass is performed, as for the reweighting method, by a simultaneous maximum likelihood fit to the pseudomass and the leptonic energy including the information of center-of-mass energies from 183 to 202 GeV. In this simultaneous fit the likelihood is defined

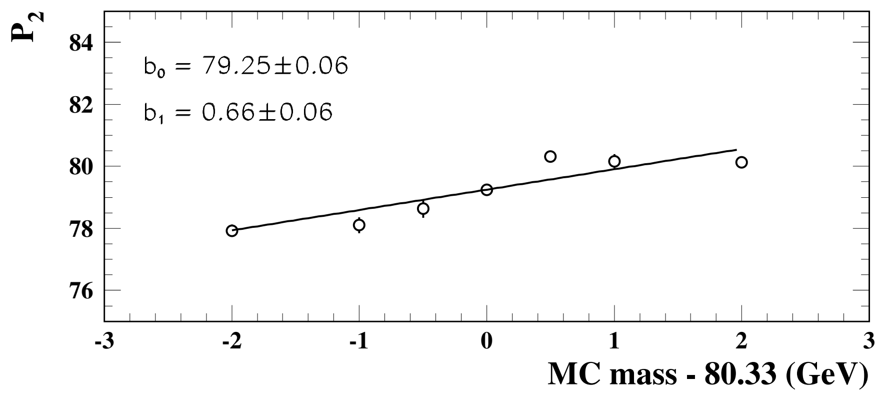

Figure 8.5: Linear fit of the coefficient P_1 (middle point of the Fermi function) to M_W at a center–of–mass energy of 189 GeV. The central value of 80.33 GeV is subtracted from all generated W masses. Similar studies were performed for the second and the third class at all center-of-mass energies.

as in equation 7.11.

The same Monte Carlo data samples used in the reweighting method generated at M_W = 80.33 GeV for each center-of-mass energy are now considered to estimate the expected statistical error on M_W. The correlation between the pseudomass and the leptonic energy was calculated to rescale the fit errors and it was found to be 13%; in agreement with the result for the reweighting method (Appendix B). The relation between the fitted masses for the pseudomass and the leptonic energy is shown in figure 8.7. The method is checked with 500 subsamples whose events are chosen in the randomly as explained in chapter 7. Figure 8.9 shows the distribution of the fit errors after the simultaneous fit. The distributions are nicely symmetric and the statistical fluctuations which were observed in the reweighting method are eliminated. The fit errors shown in figure 8.9 are rescaled by a factor 1.13 account for this correlation.

The second problem found in the reweighting procedure, the asymmetric fit uncertainties, is also much reduced. Figure 8.10 shows the high correlation between both errors. Figure 8.8(a) shows the mass distribution fitted with a Gaussian function. The mean value shows no bias and the width is in perfect agreement with the fit error distributions as shown by the pull distributions in figure 8.8(b).

8.3 Results of the Unbinned Method

The simultaneous fit for the pseudomass and the leptonic energy, combining center-of-mass energies from 183 to 202 GeV, gives the following result:

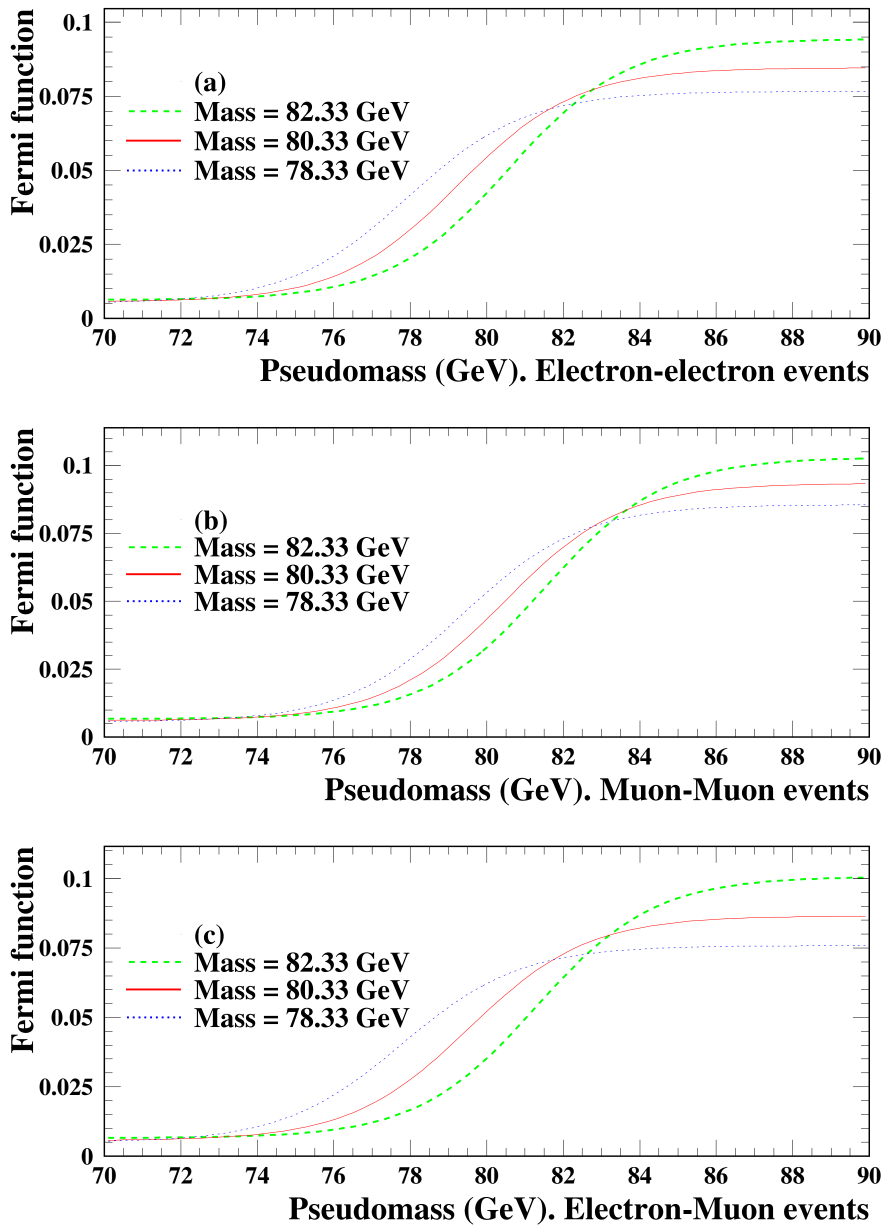

Figure 8.6: Comparison of Fermi functions for three different generated masses: 78.33 GeV (dotted line), 80.33 GeV (solid line) and 82.33 GeV (dashed line) at a center-of-mass energy of 189 GeV. (a) First class of which contains e-e events. (b) Second class which contains μ-μ events. (c) Third class which contains e-μ events.

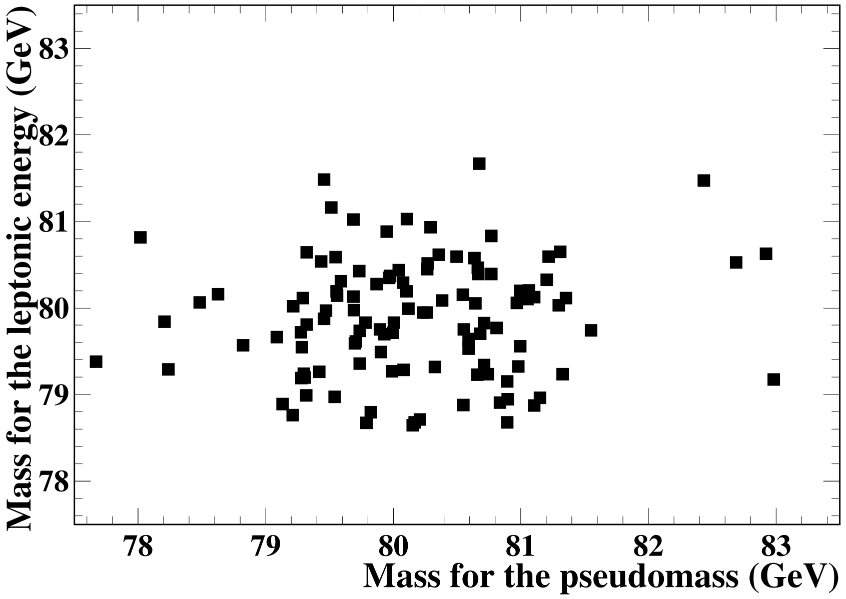

Figure 8.7: Fitted mass distribution at all center-of-mass energies for the pseudomass in comparison with the one for the leptonic energy using the unbinned methode. 112 independent Monte Carlo subsamples are used in the analysis.

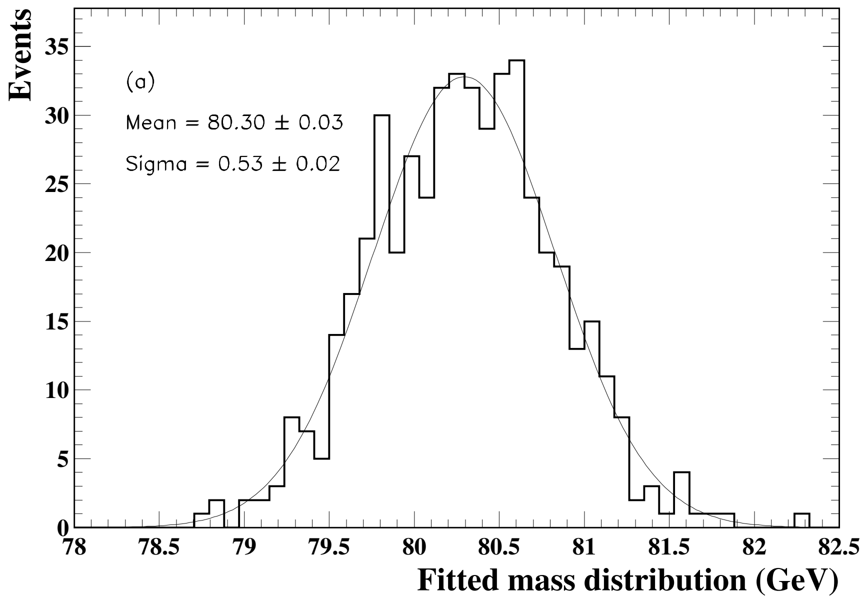

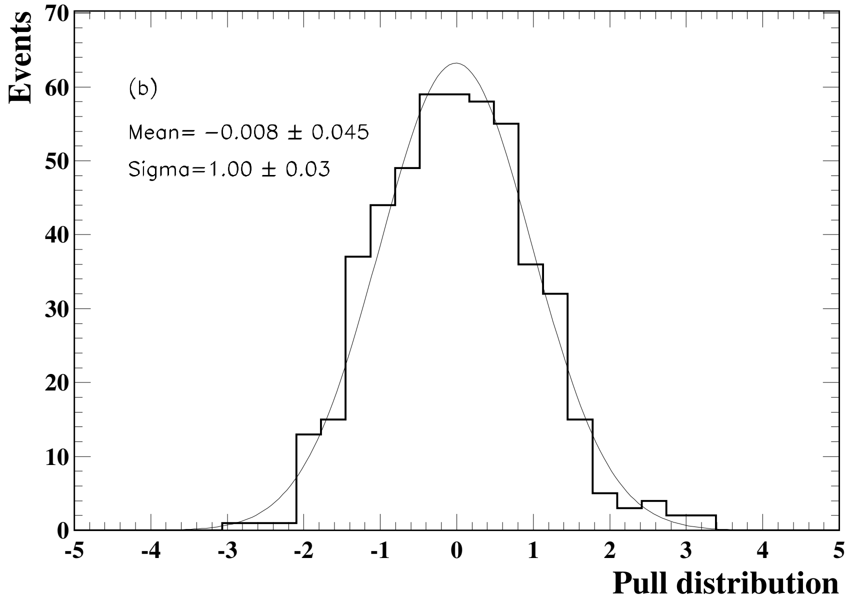

Figure 8.8: (a) Fitted mass distributions from Monte Carlo for the simultaneous fit of the pseudomass and the leptonic energy at all center-of-mass energies. The test samples are generated at $\mathrm{M_W}$ = 80.33 GeV. (b) Pull distribution. The corresponding errors are rescaled to take into account the correlation between the pseudomass and the leptonic energy.

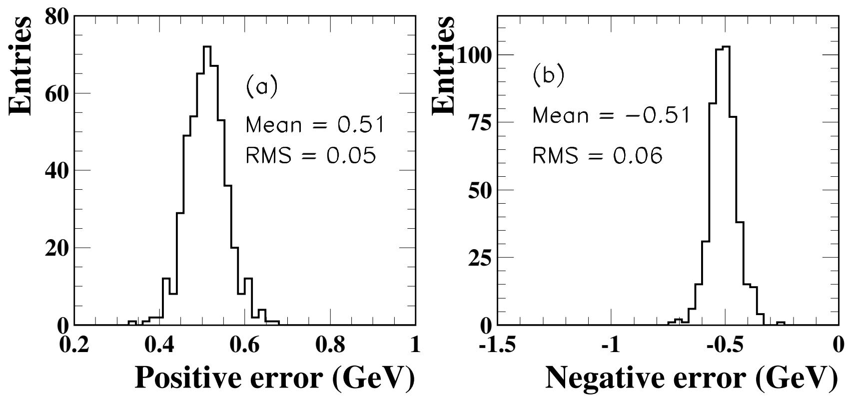

Figure 8.9: Fit error distributions for the simultaneous fit at all center-of-mass energies to the pseudomass together with the leptonic energy distribution. (a) Positive error distribution. (b) Negative error distribution. Both distributions are rescaled by a factor 1.13 to take into account the correlation between the pseudomass and the leptonic energy.

$$\boxed{\mathrm{M_W} = 80.43\ ^{+0.51}_{-0.52}\ \mathrm{GeV}.}$$

The quoted errors are derived from the fit to the data sample. The errors are rescaled by a factor 1.13 to take into account the correlation between the pseudomass and the leptonic energy. The figure 8.11 shows the $-\log(\mathrm{Likelihood})$ curve for this unbinned fit. Figure 8.12 and table 8.1 summarize the results for the W mass from $\mathrm{W^+W^-} \rightarrow \ell\nu_\ell\ell'\nu_{\ell'}$ decays for each year using an unbinned maximum likelihood method.

Figure 8.13 shows the comparison between the fit function and the data for the three classes of events defined for the pseudomass at a center-of-mass energy of 189 GeV. Figure 8.14 shows analogous results for the two classes defined for the leptonic energy at 189 GeV.

8.4 Systematic Checks and Uncertainties

The systematic uncertainties discussed for the reweighting fit (see section 7.5) also affect the unbinned method and they are evaluated in the same manner, yielding similar errors. The study of all the uncertainties are summarized in table 8.2. A new systematic source, which does not exist in the reweighting fit, is now present due to the parameterization of the pseudomass and the leptonic energy spectra. This source is explained in the next section.

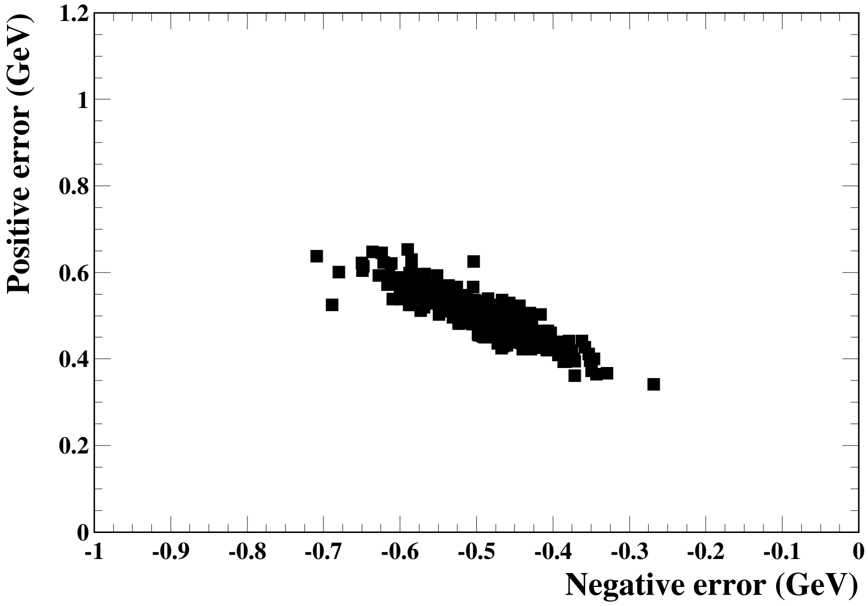

Figure 8.10: Comparison between the positive and the negative error distributions for the unbinned method. The limits are taken as in the reweighting method to compare both distributions.

Year	CM energy (GeV)	W mass (GeV)	Error (GeV)
1997	183	81.73	$\binom{+1.12}{-1.14}$
1998	189	80.16	$\binom{+0.88}{-0.91}$
1999	192–202	80.13	$\binom{+0.70}{-0.69}$
Combination	183–202	80.43	$\binom{+0.51}{-0.52}$

Table 8.1: Summary of the $\mathrm{M_W}$ results from 1997 until 1999 and combined for the leptonic channel using an unbinned maximum likelihood method. The corresponding errors are statistical.

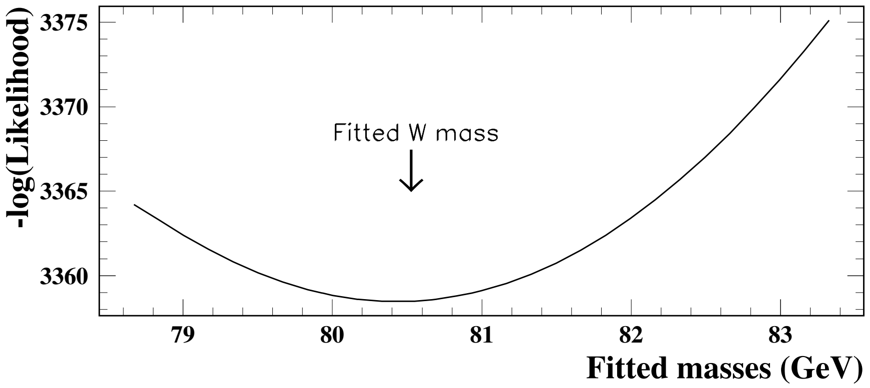

Figure 8.11: $-\log(\mathcal{L})$ curve obtained from the fit to the real data. The fitted W mass is shown with arrors.

8.4.1 Parameterization of the Sensitive Variables

A total of 114 parameters are obtained for the pseudomass and the leptonic energy considering center-of-mass energies from 183 to 202 GeV for all the defined classes and both sensitive variables. From these, 42 parameters depend on the mass of the W boson. To check the systematic error associated to the parameterization of the pseudomass and the leptonic energy distributions each parameter is varied by 1σ independent from the rest. This is repeated for all center-of-mass energies and all classes of events. The systematic error due to this source in the parameters which depend on $\mathrm{M_W}$ is 28 MeV; for the parameters independent of $\mathrm{M_W}$, the corresponding error is 20 MeV. Adding the resulting changes in quadrature yields a total systematic uncertainty due to the parameterization of 34 MeV.

8.4.2 Linearity of the Unbinned Method

The possible bias and the linearity of the unbinned procedure is checked in this section. The same samples as for the reweighting procedure are used in this case (see section 7.6.2). The relation between the generated and the fitted mass is found to be linear for the combination in a region of ± 1 GeV, with a slope of 0.984$\pm$0.065. There is no evidence of non–linear behavior in the range of 1 GeV around the central value and our measured value lies safely within this region. Therefore no additional error is assigned for this effect. The value of the bias is -0.005$\pm$0.036, compatible with zero and which statistical error is in good agreement with the systematic error associated to the parameterization source (see section 8.4.1). Figure 8.15 shows this linear behavior and the bias for the parameterization procedure.

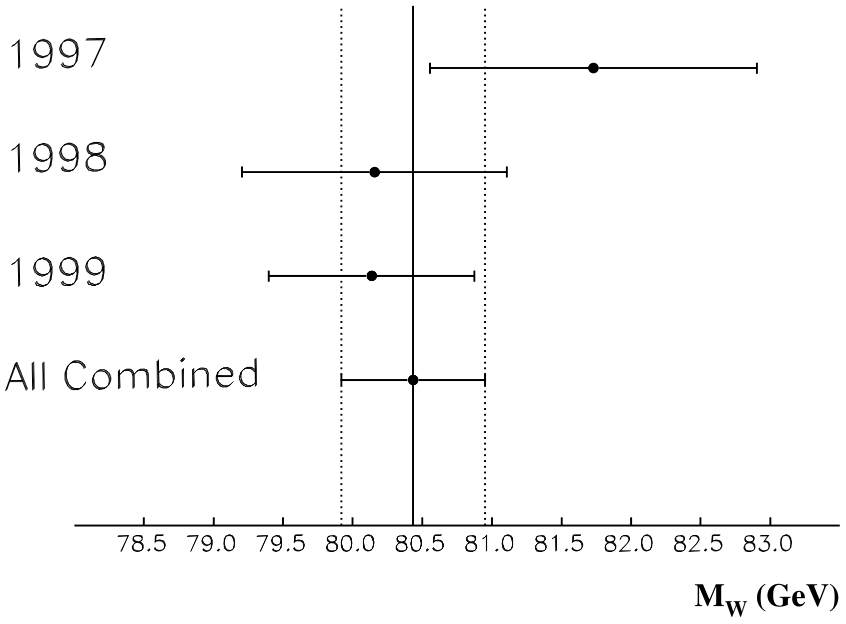

Figure 8.12: Comparison of the $\mathrm{M_W}$ results from leptonic decays using an unbinned maximum likelihood method for each year.

Systematic errors	Error (MeV)
Beam energy	< 10
Spread in the beam energy	14
ISR	< 10
Four-fermion	24
ECAL scale	129
ECAL resolution	87
CT scale	< 10
CT resolution	< 10
Background	16
Parameterization	34
Total	162

Table 8.2: Summary of systematic uncertainties on $\mathrm{M_W}$ measurement using the unbinned method.

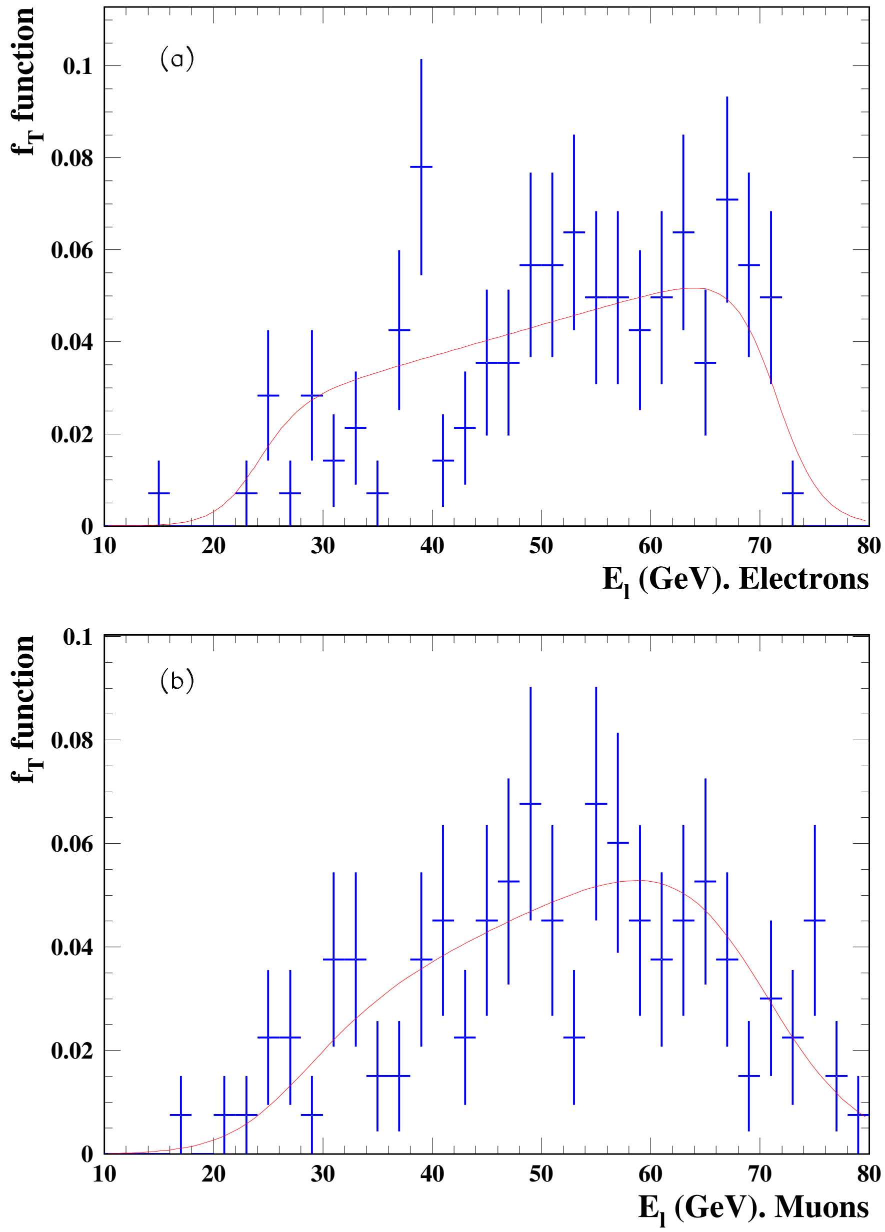

Figure 8.13: Comparison between the data and the f_T function for the leptonic energy at a center–of–mass energy of 189 GeV. (a) electron events. (b) muon events.

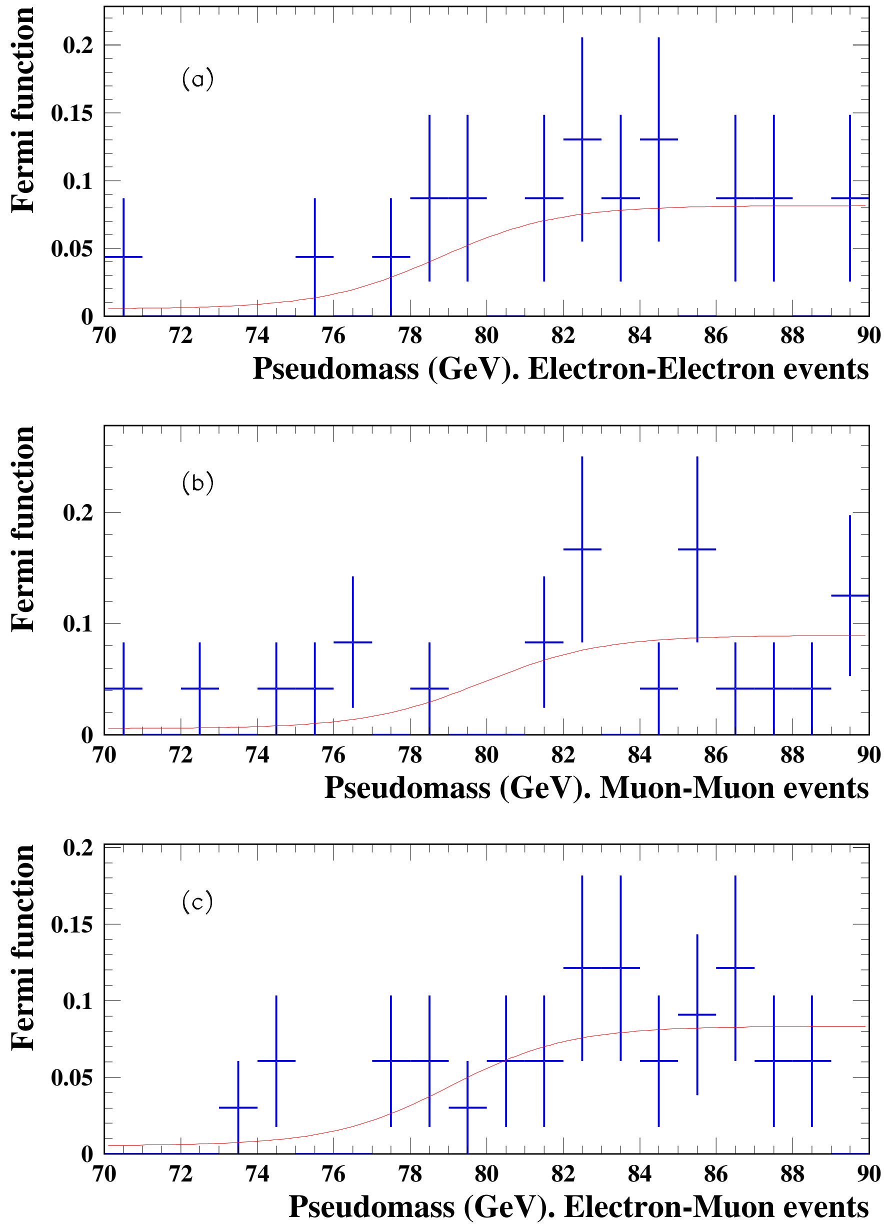

Figure 8.14: Comparison between the data and the fit function for the pseudomass at a center–of–mass energy of 189 GeV. (a) electron–electron events. (b) muon–muon events. (c) electron–muon events.

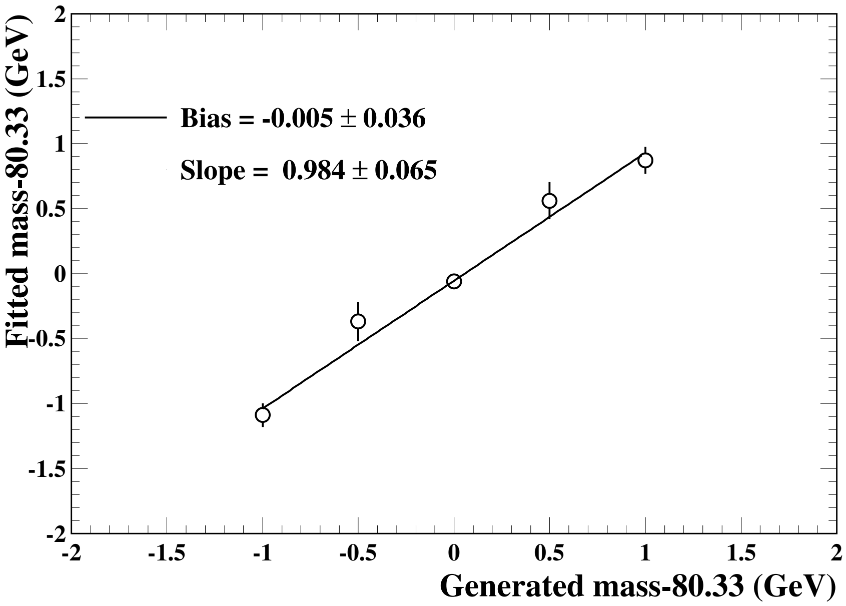

Figure 8.15: Linearity of the unbinned method procedure. The central value of 80.33 GeV is subtracted from all the masses.

Chapter 9

Comparison of the Methods and Combination with the $\mathrm{W^+W^-} \to \mathrm{q_1\overline{q}_2q_3\overline{q}_4}$ and $\mathrm{W^+W^-} \to \mathrm{q_1\overline{q}_2}\ell\nu_\ell$ Channels

The *reweighting technique* is one of the standard methods by all four LEP collaborations to determine $\mathrm{M_W}$. In the present thesis it is therefore used to study the mass of the W boson from $\mathrm{W^+W^-} \to \ell\nu_\ell\ell'\nu_{\ell'}$ decays. It was well known that one of the biggest problems of this channel is the small branching ratio and therefore the small number of events in the data sample. Due to this feature, the first studies were performed at center-of-mass energy of 189 GeV. At this energy, the number of events were enough to obtain a first estimate of $\mathrm{M_W}$. As chapter 7 shows, the results obtained with this method present big fluctuations due to the small statistics in data. The limited Monte Carlo statistics for the production of the reweighted histogram contribute as well to these fluctuations. The solution is clear for this method, it is necessary to add more statistics. Additional data from center-of-mass energies of 183, 192, 196, 200 and 202 GeV were therefore included in the method but although the fluctuations decrease by including more data, they are not eliminated completely (section 7.3). As a consequence the method to determine $\mathrm{M_W}$ can be subjected to the influence of these fluctuations. If this is the case (and it is!), the results for the data are very assymetric and the combination with other $\mathrm{M_W}$ measurements from $\mathrm{W^+W^-} \to \mathrm{q_1\overline{q}_2q_3\overline{q}_4}$ and $\mathrm{W^+W^-} \to \mathrm{q_1\overline{q}_2}\ell\nu_\ell$ decays becomes difficult.

This is the motivation which leads to the *unbinned method* to determine $\mathrm{M_W}$. The fluctuations due to the small statistics now decrease, the expected error distribution is symmetric and the positive and the negative error values are in good agreement. Now it is easier to combine the result obtained with other measurements.

In spite of the fluctuations present in the reweighting technique, both methods show a good agreement between their results; the ideal expected errors have the same values and the obtained correlations for the leptonic energy and the pseudomass are compatible. The systematic errors are similar as well. The systematic uncertainty for the unbinned method is around 50 MeV larger than for the reweighting fit, due to the systematic source associated to the parameterization of the leptonic energy and the pseudomass spectra.

9.1 Combination with Hadronic and Semileptonic Channels Results

Results from center-of-mass energies 192 to 202 GeV which have been obtained using a fit to the distribution of the reconstructed W masses in decays of the type $\mathrm{W^+W^-} \rightarrow \mathrm{q_1\overline{q}_2q_3\overline{q}_4}$ and $\mathrm{W^+W^-} \rightarrow \mathrm{q_1\overline{q}_2}\ell\nu_\ell$, have been combined with previous OPAL measurements at center-of-mass energies from 161 until 189 GeV. The results are summarized as follows:

- $\sqrt{\mathrm{s}}$ = 161 to 189 GeV with $\mathrm{W^+W^-} \rightarrow \mathrm{q_1\overline{q}_2q_3\overline{q}_4}$ and $\mathrm{W^+W^-} \rightarrow \mathrm{q_1\overline{q}_2}\ell\nu_\ell$ events [51]:

$$\mathrm{M_W} = 80.432 \pm\ 0.066 \pm 0.045\ \mathrm{GeV}$$

- $\sqrt{\mathrm{s}}$ = 192 to 202 GeV with $\mathrm{W^+W^-} \rightarrow \mathrm{q_1\overline{q}_2q_3\overline{q}_4}$ and $\mathrm{W^+W^-} \rightarrow \mathrm{q_1\overline{q}_2}\ell\nu_\ell$ events [95]:

$$\mathrm{M_W} = 80.523 \pm\ 0.073 \pm 0.042\ \mathrm{GeV}.$$

The present measurements have been combined with each other and with the result presented in this thesis obtained for $\mathrm{M_W}$ from the reweighting method [45, 95]:

$$\mathrm{M_W} = 80.485 \pm\ 0.052 \pm 0.039\ \mathrm{GeV}.$$

The impact of the $\mathrm{W^+W^-} \rightarrow \ell\nu_\ell\ell'\nu_{\ell'}$ channel to the general result is around 1%. Analogous results are obtained by combining with $\mathrm{M_W}$ obtained from $\mathrm{W^+W^-} \rightarrow \ell\nu_\ell\ell'\nu_{\ell'}$ decays using the unbinned method.

9.2 $\mathbf{M_W}$ from $\mathbf{W^+W^-} \rightarrow \boldsymbol{\ell\nu_\ell\ell'\nu_{\ell'}}$ Decays by the LEP Experiments

In parallel to OPAL, the other 3 experiments of LEP (ALEPH, DELPHI and L3) performed studies of $\mathrm{M_W}$ in this channel. The methods and results are summarized as follows:

- ALEPH and L3 employ the kinematic properties of the leptons to estimate the W mass. The variables used to measure $\mathrm{M_W}$ are the energy of the most energetic lepton, $\mathrm{E}_\ell^{\mathrm{max}}$, and the energy of the second most energetic lepton, $\mathrm{E}_\ell^{\mathrm{min}}$. The missing energy, $\mathrm{E^{miss}}$, of the events, defined as $\sqrt{\mathrm{s}}$-$\mathrm{E^{vis}}$ where $\mathrm{E^{vis}}$ is the reconstructed visible energy of the events, is used in the ALEPH analysis as well. The technique used to obtain $\mathrm{M_W}$ and its error is a reweighting method. Individual likelihoods functions for each variable are defined considering the lepton flavors together in each likelihood. The OPAL analysis presented does the opposite; the total likelihood considers individual contributions from the variables and different lepton flavours classes. The better resolution in the measurements of muons by ALEPH and L3 allows the lepton flavors to be considered together. Figure 9.1 shows the sensitive variables to $\mathrm{M_W}$ used in the analysis by ALEPH. The analysis has been performed at a center-of-mass energy of 189 GeV by L3 and 183 combined with 189 GeV by ALEPH. The results obtained are [88]:

$$\text{ALEPH } (183 - 189 \text{ GeV}): \ \mathrm{M_W} = 81.81 \pm 0.67 \pm 0.20 \text{ GeV}$$

where the first error is statistical and the second one is systematic.

At present L3 only quotes the expected statistical error of their measurements at 189 GeV [96]:

$$\text{L3 } (189 \text{ GeV}): \ \Delta\mathrm{M_W} = 0.95 \text{ GeV}$$

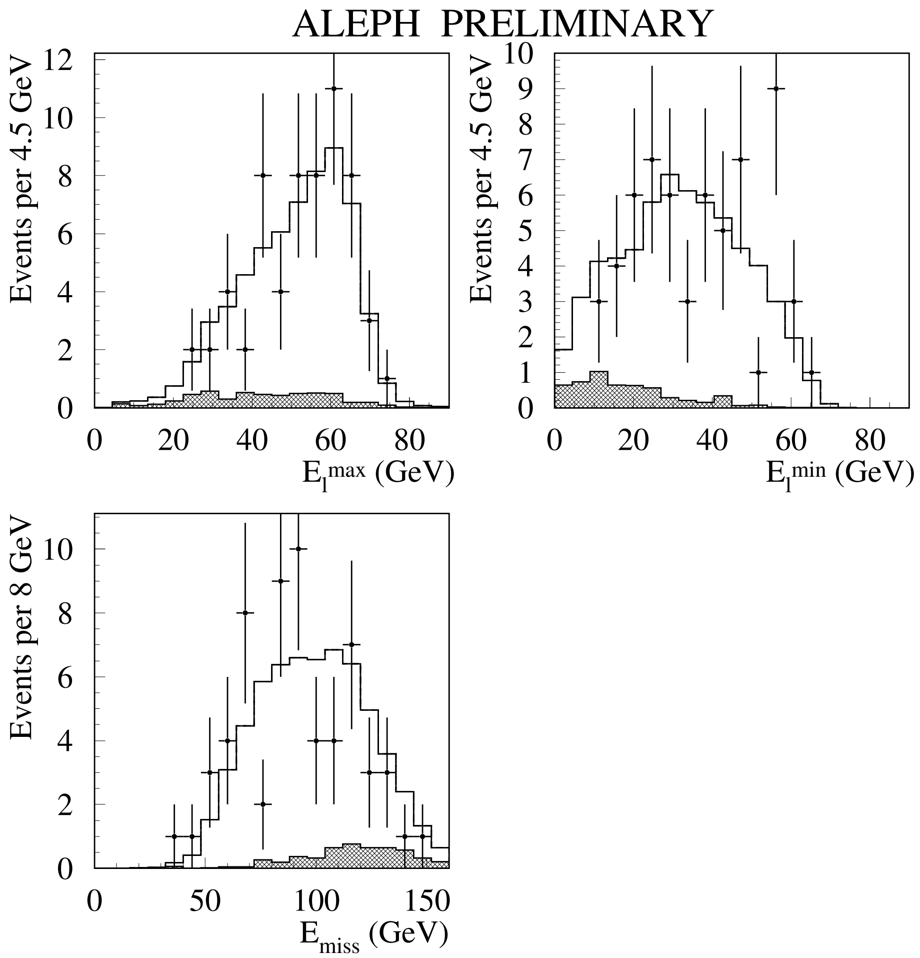

Figure 9.1: Distributions of the higher and lower lepton momenta and of the missing energy in each $\mathrm{W^+W^-} \to \ell\nu_\ell\ell'\nu_{\ell'}$ events at 189 GeV, comparing with the reweighted Monte Carlo prediction giving the best combined fit.

- DELPHI has worked on a method which can use the full information of the event. The basic idea is that given the two charged three-momenta of each event and assuming that they come from different and independent bodies, only certain boost values and certain directions are possible for the W bosons. Using the standard constrains of a kinematic fit, it is possible to define a probability density function (*p.d.f*) which depends on the boost, β and the directions $\theta,\ \phi$. An unbinned likelihood which contains the detector effects can be therefore defined to obtain $\mathrm{M_W}$:

$$\mathcal{L}(\mathrm{M_W}) = \int p.d.f(\beta,\theta,\phi) \times F(\beta,\theta,\phi/\mathrm{M_W})$$

where F is a function of the purity and the signal and background expectations. An individual likelihood function is defined for each leptonic channel and the general fit is performed with a *p.d.f* obtained as the weighted sum of each leptonic channel to take into account the cross contamination between the channels; for example a selected $\mathrm{e}\nu\mathrm{e}\nu$ event has a certain probability to be a $\mathrm{e}\nu\tau\nu$ or a $\tau\nu\mathrm{e}\nu$ or even a $\tau\nu\tau\nu$ event. The weights with which the *p.d.f* are summed, are extracted from Monte Carlo studies and depend upon the momentum of the considered lepton[1]. The events containing τ leptons are treated separately from the other channels. The result obtained by DELPHI at a center-of-mass energy of 189 GeV, combining all leptonic channels is [97]:

$$\text{DELPHI}\ (189\ \mathrm{GeV}):\ \Delta\mathrm{M_W}\ = 0.73\ \mathrm{GeV}.$$

No value for $\mathrm{M_W}$ is currently published. A good agreement between the four experiments is found for an expected error of 0.75 GeV at a center-of-mass energy of 189 GeV. Table 9.1 shows the comparison between the results for the four experiments.

Experiment	$\sqrt{\mathrm{s}}$ (GeV)	$\Delta\mathrm{M_W}$ (GeV)
ALEPH	183-189	0.67
DELPHI	189	0.73
L3	189	0.95
OPAL	183-189	0.69
OPAL	183-202	0.51

Table 9.1: Comparison between the results in $\mathrm{W^+W^-} \to \ell\nu_\ell\ell'\nu_{\ell'}$ channel for the four experiment. The errors given are statistical.

[1] An electron of 20 GeV has a certain probability to come from tau decays, while an electron of 70 GeV is almost certainly coming from the W decay. This is the reason of the weight factors definition.

Chapter 10

Summary

This thesis has presented the first determination of the mass of the W boson in the fully leptonic channel using the data of the OPAL detector at LEP. Two different methods, using the same sensitive variables were employed to extract the W mass from the data sample recordered between 1997 and 1999 at center-of-mass energies of 183, 189, 192, 196, 200 and 202 GeV. All these data amount to an integrated luminosity of 457.1 pb^{-1}.

The precise measurement of the W mass has been one of the major goals of the LEP2 program. This mass combined with other electroweak measurements, provides stringent tests of the current theory which explains the matter and its interactions, the Standard Model, and it can be used to constrain the mass of the Higgs boson. Previous analysis performed by OPAL were based on the fully hadronic and semi-leptonic $\mathrm{W}^+\mathrm{W}^-$ decay modes.

The $\mathrm{W}^+\mathrm{W}^- \rightarrow \ell\nu_\ell\ell'\nu_{\ell'}$ events comprise the 10% of the total $\mathrm{W}^+\mathrm{W}^-$ cross section. They are characterized by two acoplanar charged leptons and a large missing energy due to at least two non-observed neutrinos in the final state. The standard method to determine $\mathrm{M_W}$ from $\mathrm{W}^+\mathrm{W}^- \rightarrow \mathrm{q}_1\overline{\mathrm{q}}_2\mathrm{q}_3\overline{\mathrm{q}}_4$ and $\mathrm{W}^+\mathrm{W}^- \rightarrow \mathrm{q}_1\overline{\mathrm{q}}_2\ell\nu_\ell$ events which is based on a full kinematic reconstruction of the event, is here therefore not possible because the system is not enough constrained to define a kinematic fit which leads to the reconstruction of the leptonic event. Additional measurement methods have to be used to obtain $\mathrm{M_W}$ in this channel. These methods are based on the sensitivity that some variables present to $\mathrm{M_W}$. The present analysis employs as sensitive variables the directly measured energy of the charged leptons together with another kinematic variable called pseudomass. This latter variable is obtained from an approximative reconstruction of the event which is achieved defining the standard constraints of a kinematic fit plus an additional arbitrary constraint which is the assumption that both neutrinos are in the same plane as the charged leptons. Under this circumstance, the leptonic event can be reconstructed and a sensitive variable to $\mathrm{M_W}$, called the pseudomass, is obtained. This assumption can be generalized assuming fixed angles between the plane of the neutrinos and the plane of the charged leptons. An increase of the sensitivity is however not found.

Due to the different momentum resolutions obtained in OPAL for electrons and for muons, separate classes have been defined for the leptonic energy and for the pseudomass depending upon the different lepton flavors. This separation of the leptons which are measured with the electromagnetic calorimeter energy in the case of identified electrons and the charged momentum in the case of identified muons, maximizes the sensitivity of the measurement.

The first measurement which has been presented determines $\mathrm{M_W}$ from a *reweighting method*. In this method, the W mass is measured by directly comparing the pseudomass and the leptonic energy spectra in the data to fully simulated Monte Carlo spectra generated at different W masses. These Monte Carlo spectra are obtained by reweighting each event of Monte Carlo samples with a factor which depends on the generated W masses and the desired $\mathrm{M_W}$. A simultaneous likelihood fit for the pseudomass and the leptonic energy combining center-of-mass energies from 183 to 202 GeV leads to $\mathrm{M_W}$ together with its error. The result obtained with the reweighting technique is:

$$\boxed{\mathrm{M_W} = 80.30\ ^{+0.48}_{-1.55} \pm 0.14\ \mathrm{GeV},}$$

where the first error is statistical and the second one systematic.

The asymmetry obtained in the error comes from statistical fluctuations due to the small number of events contained in the data and the limited Monte Carlo statistic to build the reweighted sample which fit the data. Previous Monte Carlo studies of the reweighting method confirmed the existence of these asymmetries in the statitical error. This fact makes a combination of this results with $\mathrm{M_W}$ measurements from $\mathrm{W^+W^-} \to \mathrm{q_1\overline{q}_2q_3\overline{q}_4}$ and $\mathrm{W^+W^-} \to \mathrm{q_1\overline{q}_2}\ell\nu_\ell$ events difficult.

The possible asymmetry of the errors obtained with the reweighting method motivates the study of a second $\mathrm{M_W}$ measurement technique based on an *unbinned likelihood method*. The basic idea of this method is the parameterization of the pseudomass and the leptonic energy spectra by known analytical functions. Assuming a linear dependence of the coefficients which define the parameterization with the W mass, an unbinned likelihood function which depends now on $\mathrm{M_W}$ and the values of the sensitive variables is defined to obtain the W mass. A simultaneous fit for the pseudomass and the leptonic energy leads to this result using the same data sample as for the reweighting technique. The result obtained applying the unbinned method to the data is:

$$\boxed{\mathrm{M_W} = 80.43\ ^{+0.51}_{-0.52} \pm 0.16\ \mathrm{GeV}.}$$

The correlation between the pseudomass and the leptonic energy have been studied separately for both methods. In both cases the obtained value for the correlation factor is 13%. The slightly different event samples used in the cases of the leptonic energy and the pseudomass and the fact that the pseudomass employs the angular distribution information between both charged leptons, which is not included in the leptonic energy, leads to this small correlation. In spite of the fluctuations obtained with the reweighting technique, both methods present good agreement in the Monte Carlo studies performed to obtain the fitted mass distribution and the expected error whose value is:

$$\Delta\mathrm{M_W} = 0.51\ \mathrm{GeV}.$$

The previous $\mathrm{M_W}$ measurements obtained by OPAL in the hadronic, $\mathrm{W^+W^-} \to \mathrm{q_1\overline{q}_2q_3\overline{q}_4}$ and the semi-leptonic channel, $\mathrm{W^+W^-} \to \mathrm{q_1\overline{q}_2}\ell\nu_\ell$ channels can be now easily combined with the corresponding one of the $\mathrm{W^+W^-} \to \ell\nu_\ell\ell'\nu_{\ell'}$ channel obtained from the unbinned method.

The combination of the three channels using data recorded between 161 and 202 GeV (in the case of the semileptonic and hadronic events) leads to a W mass of:

$$M_W = 80.485 \pm\ 0.051\ \pm 0.038\ \mathrm{GeV}.$$

For the fully leptonic decays, the methods used by the four LEP experiments show a similar statistical sensitivity to M_W. The expected error obtained at center–of–mass energies of 183 and 189 GeV is around 0.75 MeV.

The results obtained in the fully leptonic channel cannot compete in accuracy with those obtained from $W^+W^- \rightarrow q_1\overline{q}_2q_3\overline{q}_4$ and $W^+W^- \rightarrow q_1\overline{q}_2\ell\nu_\ell$ events but this was not the goal of this thesis. Nevertheless, the statistical gain obtained including the fully leptonic channel in the result of M_W taking into account hadronic and semileptonic events should not be neglected. In terms of statistic, an improvement of 1% in the general result means a gain of 2% in the luminosity and the effort made to gain an additional 2% is huge in comparison with the present analysis. However, this is not the most important motivation and two different aspects should be taken into account. First, the method here developed and presented is completly complementary to those used in the other two channels. The effort made by the collaborations to perform cross-checks for the M_W result is tremendous in comparison to the present analysis. Second, any improvements on M_W in the near future will come from hadron colliders (Tevatron at Fermilab and LHC at CERN) and they are only sensitive to leptonic W decays. A comparison of M_W measurements from different decay channels can only be performed at e^+e^- colliders and therefore for LEP, it is mandatory to include this comparison in their analysis.

The year 2000 closes the LEP2 era. All the data recorded by the four experiments between 1996 and 2000 at center-of-mass energies from 161 to 210 GeV will confirm the LEP M_W measurement as what it is already: the most precise result of the W boson mass.

Appendix A

Kinematic Reconstruction of Fully Leptonic Events

The kinematics of the $W^+W^- \to \ell\nu_\ell\ell'\nu_{\ell'}$ process is determined by six angles, two for the scattering, and two for each W decays. The two three-momenta of the charged leptons are known and this should be enough to fix the whole system. A twofold ambiguity occurs, however, because the solution involves a quadratic equation. Both solutions of the equation are perfectly compatible with the system but not distingable experimetally. A solution for the two nonobserved neutrino momenta p_ν and $p_{\nu'}$ are now presented as a function of the observed lepton momenta ℓ and ℓ'. The analysis is performed in the e^+e^- center of mass frame and assuming the neutrinos to be massless. The system will be solved for $p_{\nu'}$, because p_ν is given by momentum conservation.

1. Assuming that the W^- energy is equal to the beam energy E_b:

$$p^0_{\nu'} = E_b - \ell_0 \tag{A.1}$$

   or:

$$p^2_{\nu'} = (E_b - \ell_0)^2 \tag{A.2}$$

   where $p^0_{\nu'} = |p_\nu|$ is the energy of the neutrino and ℓ_0 is the charged lepton energy.

   A similar equation comes from the other W^+ boson:

$$p^2_{\nu} = (E_b - \ell'_0)^2 \tag{A.3}$$

2. Using the momentum conservation for the momenta of the charged leptons , the equation (A.2) can be rewritten in terms of $p_{\nu'}$:

$$(\ell + \ell') \cdot p_{\nu'} = E_b(\ell_0 + \ell'_0) - \ell_0^2 - \ell \cdot \ell' + \frac{1}{2}(m_\ell^2 + m_{\ell'}^2) \tag{A.4}$$

   where m_ℓ^2 and $m_{\ell'}^2$ are the masses of the charged leptons.

3. The third constraint comes from the condition that the lepton–antineutrino system should have the mass of the W boson:

$$(\ell + p^0_{\nu'})^2 = m_W^2 \tag{A.5}$$

which gives from (A.2):

$$\ell \cdot p_{\nu'} = E_b \ell_0 - \ell_0^2 - \frac{1}{2} m_W^2 + \frac{1}{2} m_\ell^2 \tag{A.6}$$

Using the relation obtained in (A.4) and (A.5):

$$\ell' \cdot p_{\nu'} = -E_b \ell'_0 - \ell \cdot \ell' + \frac{1}{2} m_W^2 + \frac{1}{2} m_{\ell'}^2 \tag{A.7}$$

The conditions of equations (A.4), (A.6) and (A.7) provide a solution for $p_{\nu'}$. The right–hand sides of these equations can be rewritten:

$$p^2_{\nu'} = L \tag{A.8}$$

$$\ell \cdot p^2_{\nu'} = M \tag{A.9}$$

$$\ell' \cdot p^2_{\nu'} = N \tag{A.10}$$

It is assumed the most general case in which the two three-momenta ℓ and ℓ' are not parallel. Expanding $\mathrm{p}^2_{\nu'}$ in terms of ℓ and ℓ':

$$p_{\nu'} = a\,\ell + b\,\ell' + c\,\ell \times \ell' \tag{A.11}$$

Using this last relation in (A.9) and (A.10), they give:

$$a\,\ell^2 + b\,\ell \cdot \ell' = M, \tag{A.12}$$

$$a\,\ell \cdot \ell' + b\,\ell'^2 = N,$$

which can be explicitly solved:

$$\begin{pmatrix} a \\ b \end{pmatrix} = \frac{1}{\ell^2 \ell'^2 - (\ell \cdot \ell')^2} \begin{pmatrix} \ell'^2 & -\ell \cdot \ell' \\ -\ell \cdot \ell' & \ell^2 \end{pmatrix} \begin{pmatrix} M \\ N \end{pmatrix}$$

The last variable c is determined using (A.8):

$$c^2 = \frac{1}{|\ell \times \ell'|^2} (L - a^2 \ell^2 - b^2 \ell'^2 - 2a\,b\,\ell \cdot \ell') \tag{A.13}$$

Experimentally the sign of c cannot be determined. This shows the twofold discrete ambiguity mentioned at the biginning of present appendix. Geometrically the ambiguity in the neutrino momenta corresponds to two specular vectors, one over, the other under the plane formed by the two charged leptons.

Appendix B

Correlation between Measurements of a Single Physical Quantity

The correlation between N different estimates of a physical quantity is obtained from the error matrix defined as [98]:

$$\mathbf{E} = \begin{pmatrix} \sigma_1^2 & cov_{12} & \dots & cov_{1N} \\ cov_{21} & \sigma_2^2 & & \vdots \\ \vdots & \vdots & \ddots & \vdots \\ cov_{N1} & \dots & \dots & \sigma_N^2 \end{pmatrix} \tag{B.1}$$

where σ_N^2 [1] are the variance for each invididual measurement and cov_{nm} is the covariance between measurements n and m and it is defined as:

$$cov_{nm} = \sigma_n \sigma_m r_{nm} \tag{B.2}$$

where r_{nm} is the correlation factor between n and m estimates. Thus, if the measurements are uncorrelated the error matrix is diagonal whereas elements outside of the principal diagonal give an idea of the lineal relation (this is the correlation) between the measurements.

The full error matrix is estimated by Monte Carlo simulation. A total number of N independent subsamples are taken and they are subjected to the same selection criteria as were used in the real data. In this way N sets of estimations τ_{ik} are obtained, where k denotes the Monte Carlo subsample number and i refers to the method uses to determine τ, i.e. the variable.

The elements of the error matrix are defined as:

$$E_{ij} = \frac{1}{N} \sum_{i=1}^{N} (\tau_{ik} - \overline{\tau_i})(\tau_{jk} - \overline{\tau_j}) \tag{B.3}$$

[1]The *variance* σ^2 is defined as $E(x^2) - \mu^2$, where E is the expected value, x is the performed measurement of a physical quantity and μ is its mean value. The variance is a measure of how widely the measurement x is spread about its mean value μ. The square root of the variance σ is called the *standard deviation* of x [99].

where $\overline{\tau_i}$ is the Monte Carlo average for the i variable:

$$\overline{\tau_i} = \frac{1}{N}\sum_{k=1}^{N}\tau_{ik} \tag{B.4}$$

The correlation factor r_{nm} between the variables n and m is determined therefore from the corresponding error matrix element cov_{nm}, using the equation (B.2).

Appendix C

Coefficients for the Unbinned Maximum Likelihood Fit

The differents coefficients obtained from the linear dependence studies to $\mathrm{M_W}$ for the leptonic energy and the pseudomass for all their classes are summarized in the following tables:

First class for the leptonic energy							
	$\mathrm{P_1}$		$\mathrm{P_2}$	$\mathrm{P_3}$		$\mathrm{P_4}$	$\mathrm{P_6}$
$\sqrt{s}$ (GeV)	$\mathrm{b_0}$	$\mathrm{b_1}$	$\mathrm{b_0}$	$\mathrm{b_0}$	$\mathrm{b_1}$	$\mathrm{b_0}$	$\mathrm{b_0}$
183	23.58±0.10	0.88±0.19	2.44±0.07	65.81±0.06	-0.90±0.12	2.15±0.04	0.07±0.01
189	22.76±0.08	0.47±0.07	2.14±0.07	70.27±0.05	-0.86±0.04	2.08±0.05	0.08±0.01
192	23.26±0.11	0.31±0.22	2.35±0.10	71.73±0.06	-1.01±0.12	2.15±0.04	0.07±0.01
196	23.60±0.11	0.35±0.14	2.70±0.08	74.68±0.07	-0.61±0.18	2.25±0.05	0.05±0.01
200	23.03±0.12	0.30±0.21	2.41±0.09	76.82±0.07	-0.67±0.13	2.28±0.05	0.11±0.02
202	23.53±0.12	0.52±0.23	2.62±0.09	78.72±0.07	-0.87±0.13	2.21±0.04	0.07±0.01

Table C.1: Numerical values of the coefficients for the first class of defined for the leptonic energy at all center–of–mass energies.

Second class for the leptonic energy							
	$\mathrm{P_1}$		$\mathrm{P_2}$	$\mathrm{P_3}$		$\mathrm{P_4}$	$\mathrm{P_6}$
$\sqrt{s}$ (GeV)	$\mathrm{b_0}$	$\mathrm{b_1}$	$\mathrm{b_0}$	$\mathrm{b_0}$	$\mathrm{b_1}$	$\mathrm{b_0}$	$\mathrm{b_0}$
183	23.91±0.17	1.18±0.30	3.84±0.12	64.67±0.09	-0.73±0.18	4.03±0.05	1.41±0.01
189	23.04±0.13	0.61±0.11	3.73±0.11	68.71±0.08	-0.65±0.07	4.46±0.07	1.36±0.01
192	23.02±0.14	0.58±0.27	3.59±0.15	70.03±0.10	-0.69±0.19	4.48±0.08	1.96±0.15
196	22.36±0.15	0.49±0.27	3.27±0.16	72.73±0.11	-0.30±0.20	5.12±0.07	1.45±0.09
200	24.09±0.17	0.42±0.28	5.11±0.21	74.71±0.12	-1.35±0.22	5.61±0.09	0.45±0.11
202	23.44±0.19	0.50±0.26	4.45±0.18	76.00±0.12	-0.97±0.24	5.67±0.09	1.16±0.15

Table C.2: Numerical values of the coefficients for the second class of defined for the leptonic energy at all center of mass energies.

First class for the pseudomass				
	P_2		P_3	P_4
$\sqrt{s}$ (GeV)	b_0	b_1	b_0	b_0
183	78.99±0.07	0.45±0.16	1.61±0.07	0.058±0.006
189	79.25±0.06	0.66±0.06	1.49±0.05	0.080±0.005
192	79.59±0.07	1.74±0.15	1.55±0.06	0.069±0.005
196	79.86±0.07	0.62±0.12	1.27±0.05	0.115±0.006
200	80.54±0.09	0.74±0.17	1.73±0.05	0.096±0.003
202	81.44±0.09	0.50±0.23	1.84±0.10	0.058±0.006

Table C.3: Numerical values of the coefficients for the first class of events defined for the pseudomass at all center of mass energies.

Second class for the pseudomass				
	P_2		P_3	P_4
$\sqrt{s}$ (GeV)	b_0	b_1	b_0	b_0
183	80.29±0.09	1.27±0.20	2.91±0.10	0.053±0.008
189	80.45±0.08	0.53±0.07	3.18±0.09	0.041±0.006
192	80.10±0.06	0.56±0.14	1.90±0.06	0.135±0.006
196	80.81±0.09	0.74±0.15	2.24±0.08	0.151±0.007
200	81.85±0.10	0.41±0.17	2.55±0.09	0.156±0.008
202	83.47±0.12	1.20±0.34	3.42±0.11	0.081±0.006

Table C.4: Numerical values of the coefficients for the second class of events defined for the pseudomass at all center of mass energies.

Third class for the pseudomass				
	P_2		P_3	P_4
$\sqrt{s}$ (GeV)	b_0	b_1	b_0	b_0
183	79.53±0.05	1.14±0.13	1.85±0.05	0.097±0.005
189	79.53±0.05	0.87±0.05	2.13±0.05	0.082±0.004
192	79.90±0.05	0.53±0.11	1.71±0.05	0.114±0.005
196	80.64±0.07	0.85±0.15	1.14±0.02	0.042±0.006
200	80.80±0.06	0.62±0.12	2.22±0.06	0.104±0.005
202	81.67±0.07	1.14±0.16	2.56±0.07	0.094±0.005

Table C.5: Numerical values of the coefficients for the third class of events defined for the pseudomass at all center of mass energies.

Bibliography

[1] S. Weinberg, Phys. Rev. Lett **19** (1967) 1264.

[2] A. Salam, In Elementary Particle Theory, (Stockholm: Almquist and Wiskell, 1968).

[3] S. L. Glashow, Nucl. Phys **22** (1961) 579.

[4] G. 't Hooft, Rev. Mod. Phys. **72** (2000) 333–339.

[5] M. J. G. Veltman, Rev. Mod. Phys. 72 (2000) 341–149.

[6] H. Fritzsch and M. Gell-Mann, XVth Intern. Conf. on High Energy Physics, 1973, Chicago-Batavia.

[7] The UA1 Collaboration, Zeit. Phys. **44** (1989) 15.

[8] G. Altarelli and Ronald Kleiss and Claudio Verzegnassi, Z Physics at LEP 1, CERN 89-08, CERN, 1989, Volume 1.

[9] G. Altarelli, T. Söjstrand and F. Zwirner, Physics at LEP 2, CERN 96-01, CERN, 1996, Volume 1.

[10] The LEP Collaborations, the LEP Electroweak Working Group and the SLD Heavy Flavour Working Group, (2000), CERN-EP/2000-016.

[11] CERN. Geneva, LEP Desing Report, CERN-LEP-TH-83, 1983, Volume 2.

[12] The L3 Collaboration, Nucl. Instr. Meth. **289** (1990) 35.

[13] The ALEPH Collaboration, Nucl. Instr. Meth. **294** (1990) 121.

[14] OPAL Collaboration, Nucl. Instr. Meth. **305** (1991) 275.

[15] The DELPHI Collaboration, Nucl. Instr. Meth. **303** (1991) 233.

[16] W. Hollik and G. Duckeck, Electroweak Precision Tests at LEP, (Springer Verlag, 2000).

[17] C. Caso et al., Eur. Phys. J. **15** (2000) 157.

[18] The LEP Collaborations, the LEP Electroweak Working Group and the SLD Heavy Flavour Working Group, (2001).

[19] The ATLAS Collaboration, ATLAS Technical Proposal, CERN/LHCC 94-43, CERN, 1994, needs to be updated.

[20] The CMS Collaboration, CMS Technical Proposal, CERN/LHCC 94-38, CERN, 1994, needs to be updated.

[21] B.E. Anderson et al., IEEE Transactions on Nuclear Science **41** (1994) 845.

[22] S. Anderson et al., Nucl. Instr. Meth. **403** (1998) 326.

[23] S. L. Lloyd, The OPAL Primer, 1998, Version 98a.

[24] W. Leo, Techniques for Nuclear and Particle Physics, (Springer, second edition, 1994).

[25] J. Allison et al., Nucl. Instr. Meth. **317** (1992) 47.

[26] R. Brun, GEANT 3 Users Guide, CERN/DD/EE 84-1, CERN, 1984.

[27] C. Hawkes and D. Lellouch and M. Redmond and O. Schaile and M. Schröder, ROPE 410, OPAL-Offline Note 16/OFFL-0487, CERN, 1996.

[28] F. Mandl and G. Shaw, Quantum Field Theory, (John Wiley and Sons, 1988).

[29] D. Gross, F. Wilczek, Phys. Rev. **8** (1973).

[30] S. Weinberg, Phys. Rev. Lett **31** (1973).

[31] H. Fritzsch, M. Gell-Mann and H. Leutwyler, Phys. Rev. Lett **47** (1973) 365.

[32] D. Perkins, Hochenergiephysik, (Wesley, 1991).

[33] O. Nachtmann, Elementarteilchenphysik. Phänomene und Konzepte, (Veiweg, 1986-1992).

[34] P. Schmüser, Feynman Graphen und Eichtheorien für Experimentalphysiker, (Springer, 1995).

[35] The LEP Higgs Working Group, CERN Research Board (2000).

[36] The L3 Collaboration, Phys. Lett. B (2000).

[37] The OPAL Collaboration, Eur. Phys. J. (2000), CERN-EP/2000-114.

[38] The LEP Collaborations, LEP W-Pair, Z-Pair and Single W Cross Section Results for the Summer 2000 Conferences, LEPEWWG/XSEC/ 2000-01, CERN, 2000.

[39] The OPAL Collaboration, Measurement of the W Pair Production Cross Section and Triple Gauge Boson Couplings at LEP, OPAL Physics Note PN354, CERN, 1998.

[40] A. Denner, S. Dittmaier, M. Roth and D. Wackeroth, Nucl. Phys **475** (2000) 127.

[41] S. Jadach, W. Placzek, M. Skrzypek, B.F.L Ward and Z. Was, Phys. Lett. **61** (2000) 113010.

[42] D. Bardini, GENTLE4fan v. 2.0: A Program for the Semi-Analytical Calculation of Predictions for the Processes $e^+e^- \rightarrow 4f$, DESY 96-233, HEP-PH/9612409, DESY, 1996.

[43] Y.S. Kim, Recontres de Moriond, 1997.

[44] The LEP Collaborations and the LEP W Working Group, Combined Preliminary Results on the Mass and Width of the W Boson Measured by the LEP Experiments, LEP-EWWG/MASS/ 2000-01, CERN, 2000.

[45] XXXth International Conference on High Energy Physics, Osaka 2000.

[46] The LEP Collaborations, Combined Preliminary Results on the Mass and the Width of the W Boson Measured by the LEP Experiments, LEPEWWG/MASS/ 2000-01, CERN, 2000.

[47] The ALEPH Collaboration, Phys. Lett. **401** (1997) 347.

[48] The DELPHI Collaboration, Phys. Lett. **397** (1997) 158.

[49] The L3 Collaboration, Phys. Lett. **398** (1997) 223.

[50] The OPAL Collaboration, Phys. Lett. **389** (1996) 416.

[51] The OPAL Collaboration, Measurement of the Mass and the Width of the W Boson in e^+e^- annihilations at 189 GeV, Paper submitted to physics letters, CERN, 2000, CERN-EP-2000-099.

[52] J. Dubbert, W Mass Determination in the Semileptonic Channel using a Convolution Method, OPAL Technical Note TN641, CERN, 2000.

[53] J. Dubbert, Measurement of the W Mass in the $W^+W^- \rightarrow q_1\overline{q}_2\ell\nu_\ell$ channel using a convolution method, OPAL Technical Note TN642, CERN, 2000.

[54] C.G. Littlewood, C.P. Ward, D.R Ward, Measurement of the Mass of the W boson at 189 GeV using an analitic Breit-Wigner fit, OPAL Technical Note TN658, CERN, 2000.

[55] The ALEPH Collaboration, Phys. Lett. **453** (1999) 121.

[56] The ALEPH Collaboration, Measurement of the W Mass and Width in e^+e^- Collisions at $\sqrt{s}$ = 192-202 GeV, ALEPH 018, CERN, 2000.

[57] The DELPHI Collaboration, Eur. Phys. J **2** (1998) 581.

[58] The DELPHI Collaboration, DELPHI (2000), Contributed paper for ICHEP 2000.

[59] The L3 Collaboration, Phys. Lett **407** (1997) 419.

[60] The L3 Collaboration, Preliminary Results on the Measurement of the Mass and the Width of the W Boson at LEP, L3 Note 2575, CERN, 2000.

[61] OPAL Collaboration, Eur. Phys **1** (1998) 395.

[62] The OPAL Collaboration, Determination of the W Mass in the Fully Leptonic Channel, OPAL Physics Note PN447, CERN, 2000.

[63] Tim Christiansen, Influence of 5-Jet Events on the Measurement of the Mass of the W Boson in e^+e^- Collisions, Diplomarbeit, Ludwig-Maximilians-Universität München, 2000.

[64] O. Sahr, Colour Reconnection in hadronischen W-Paar Zerfllen, Ph.D. thesis, Ludwig-Maximilians-Universität München, 2001.

[65] The OPAL Collaboration, Colour Reconnection Studies in $e^+e^- \to W^+W^-$ at $\sqrt{s}$ = 189 GeV using Inter-jet Multiplicity, OPAL Physics Note PN448, CERN, 2000.

[66] J. Dubbert, Measurement of the W Boson Mass in the $W^+W^- \to q\bar{q}\ell\bar{\nu}$ Channel with the OPAL Detector at LEP, Ph.D. thesis, Ludwig-Maximilians-Universität München, 2001.

[67] C.P. Ward and D.R. Ward and N.K. Watson et al., Program `WW113`, [Web page] http://opal.web.cern.ch/opal/manuals/ww/dev/ww.html, Last access: November 2000.

[68] Graham W. Wilson, An Improved Selection of Acoplanar Dilepton Events with High visible Energy at $\sqrt{s}$ = 172 GeV, OPAL Technical Note TN446, CERN, 1996.

[69] G. Wilson, Further Improvements to an Event Selection for Events with Two Charged Leptons and Missing Energy, OPAL Technical Note TNxxx, CERN, 2000, Draft 0.11, March 2000.

[70] The OPAL Collaboration, QCD Studies using a Cone–based Jet Finding Algorithm for e^+e^- Collsions at LEP, Paper submitted to zeitschrift für physik, CERN, 1994, CERN-PPE/94–51.

[71] Graham W. Wilson, Towards an Events Selection of Acoplanar Di-Lepton Events Optomised for the $W^+W^- \to \ell\nu_\ell\ell'\nu_{\ell'}$ channel at $\sqrt{s} \approx 2M_W$, OPAL Technical Note TN382, CERN, 1996.

[72] The OPAL Collaboration, W^+W^- Production Cross Section and W Branching Fractions in e^+e^- Collisions at 189 GeV, CERN-EP 101, CERN, 2000.

[73] The OPAL Collaboration, Search for Acoplanar Lepton Pair Events in e^+e^- Collisions at $\sqrt{s}$ = 183 and 189 GeV, CERN-EP 99-122, CERN, 1999.

[74] K. Roscoe, Improvements to the classification of leptonically decaying W pair events at $\sqrt{s}$ = 189 GeV, OPAL Technical Note TN617, CERN, 1999.

[75] M.A. Thomson and M.F. Watson, $W^+W^- \to q_1\overline{q}_2\ell\nu_\ell$ event selection at $\sqrt{s}$ = 161 GeV, OPAL Technical Note TN386, CERN, 1996.

[76] OPAL conversion finder IDGCON, implemented in the ID package.

[77] G. Altarelli, T. Söjstrand and F. Zwirner, Physics at LEP 2, CERN 96-02, CERN, 1996, Volume 2.

[78] G. Altarelli and Ronald Kleiss and Claudio Verzegnassi, Z Physics at LEP 1, CERN 89-08, CERN, 1989, Volume 3.

[79] S. Jadach and W. Placzek and M. Skrzypek and B.F.L. Ward and Z. Wa, Monte Carlo program KORALW 1.42 for All Four-Fermion Final States in e^+e^- Collision, CERN-TH 98-242, CERN, October 1998.

[80] T. Sjöstrand, Comp. Phys. Comm. **82** (1994) 74.

[81] Minami-Tayeta Collaboration, GRACE Manual version 1.0, Report 92-19, KEK, 1993.

[82] S. Jadach, W. Placzek and B.F.L. Ward, Phys. Lett **390** (1997) 298.

[83] S. Jadach, B.F.L. Ward and Z. Was, Comp. Phys. Comm. **79** (1994) 503.

[84] F.A. Berends and R. Kleiss, Nucl. Phys. **186** (1981) 22.

[85] J.A.M Vermaseren, Nucl.Phys. **229** (1983) 347.

[86] F.A. Berends and R. Pittau and R. Kleiss, Comp. Phys. Comm. **85** (1995) 437–452.

[87] J. Fujimoto, T. Ishikawa, T. Kaneko, K. Kato, S. Kawabata, Y. Kurihara, T. Munehisa, D. Perret-Gallix, Y. Shimizu and H. Tanaka, Comp. Phys. Comm. **100** (1997) 74.

[88] M. J. Duncan and G. L. Kane, W. W. Repko, Nucl. Phys. **272** (1986) 517.

[89] K. Hagiwara, R.D. Peccei, D. Zeppenfeld, Nucl. Phys **282** (1987) 253.

[90] A. Denner, Fortschr. Phys. **1** (1993) 307.

[91] C. Burgard and C. Hartmann, Measurement of the Mass and the Width of the W Boson using a Reweighting Method, OPAL Technical Note TN468, CERN, 1997.

[92] R. Barlow, Recycling Data using the MC Bootrap, MAN/HEP/99/4, 1999.

[93] F. James, MINUIT Reference Manual, CERN Program Library Long Writeup D506, CERN, 1994.

[94] LEP Energy Working Group, Eur. Phys. J. **11** (1999) 573.

[95] OPAL M_W working group, Measurement of the Mass of the W Boson in e^+e^- annihilations at 192-202 GeV, OPAL Physics Note PN422, CERN, 2000.

[96] WW00 workshop, 2000.

[97] Roberto Chierici, 2000, private communication.

[98] L. Lyons and D. Gibaut, Nucl. Inst. and Meth. in Phys. A **270** (1988) 110–117.

[99] G. Cowan, Statistical Data Analysis, (Claredon Press-Oxford, 1998).

Acknowledgments

I would like to acknowledge the support and the trust of Prof. Dr. D. Schaile. She gave me the freedom to work and to lern to my own rhythm and provided me her help, good advices and breath when I needed it.

This thesis would have never been possible without the help and advices of Dr. Günter Duckeck. He offered me his experience, his help and his time. Although many times I couldn't see any light or I was lost, I always knew that I could count on him. Thank you!

Go inside Dr. Raimund Ströhmer office with a problem, go out without it. A tireless help during all the work. Thank you for your ideas and your time.

For sure all this time in Garching would have been very different without some good colleagues. Thanks to Jörg Dubbert for his good advices for the analysis and the thesis, thanks to Oliver Sahr for his phantastish humour and for all his good ideas and correctures and thanks to Oliver Kortner for his support and trust on me.

I spent always a great time at CERN thanks to Dr. Madjid Boutemeur. He always welcame me in Geneva and if I know some small secrets of TOF is thanks to him.

I want to acknowledge the whole group of Munich University the good atmosphere that we hat to work and to enjoy in special to Frau Franz for all her help.

To the OPAL W group at CERN in special to Vato Kartvelishvili, David Ward, Nigel Watson and Eric Torrence for their help and advices for the present analysis.

I would like to mention to Roberto Chierici from CERN. We worked together in the preparation of presentations and he always found time for all my questions. Thanks for your advices and your help to present the DELPHI analysis in this thesis.

I would like to acknowledge to DAAD to trust on me and to give me a scolarship to perform this work.

A special acknowledge to Eusebio Sánchez. Thanks for paying so much attention to this analysis, for having always a great advice for all my doubts and for giving me breath and strength at any time.

Esta tesis está dedicada a mis padres. Gracias por vuestro apoyo, por vuestro sacrificio y por vuestra infinita paciencia. Gracias por confiar y por creer en mí.

To all of you thank you!

Curriculum Vitae

23. March 1972	**Born in Salamanca (Spain)**
1978–1984	Primary School. First Stage (“Amor de Dios” School in Salamanca)
1984–1987	Primary School. Second Stage (“Amor de Dios” School in Salamanca)
1987–1989	Secondary School (“Amor de Dios” School in Salamanca)
August 1989	Trinity College English Exam in Dublin
1989–1990	Preparation Course for the University (COU) (“Maestro Avila” School in Salamanca)
June 1999	Selectividad
October 1990–Juni 1996	Licenciatura in Physics at Salamanca University
Juli–August 1996	German Course. Goethe Institut in München
October 1996–October 1997	Diploma Thesis at Munich University (LMU) Title: *Untersuchung Multihadronischer Ereignisse mit Photonabstrahlung im Anfangszustand.* Supervisor: Prof. Dr. D. Schaile
October 1997–August 2000	DAAD Scholarship to perform the Doctoral Thesis at Munich University (LMU) for the OPAL Experiment. Supervisor: Prof. Dr. D. Schaile
September 1998	Autum School for High Energy Physics in Maria Laach (Germany)
Since August 2000	Scientific Employee at Munich University (LMU)
August 2000	PSI Zuoz Summer School “Phenomenology of Gauge Interactions”
March 2001	A Lecture and Workshop Series at Vanderbilt University “Astrophysics, Nuclear, Particle Physics and the Connections”